

**HETEROGENEOUS SMALL MOLECULE INTERACTIONS ON SURFACES
PROBED WITH AMBIENT PRESSURE X-RAY PHOTOELECTRON
SPECTROSCOPY**

by

Christopher M. Arble

A dissertation submitted to the Faculty of the University of Delaware in partial fulfillment of the requirements for the degree of Doctor of Philosophy in Chemistry and Biochemistry

Summer 2018

© 2018 Christopher M. Arble
All Rights Reserved

**HETEROGENEOUS SMALL MOLECULE INTERACTIONS ON SURFACES
PROBED WITH AMBIENT PRESSURE X-RAY PHOTOELECTRON
SPECTROSCOPY**

by

Christopher M. Arble

Approved: _____
Brian J. Bahnson, Ph.D.
Chair of the Department of Chemistry and Biochemistry

Approved: _____
George H. Watson, Ph.D.
Dean of the College of Arts and Sciences

Approved: _____
Ann L. Ardis, Ph.D.
Senior Vice Provost for Graduate and Professional Education

I certify that I have read this dissertation and that in my opinion it meets the academic and professional standard required by the University as a dissertation for the degree of Doctor of Philosophy.

Signed:

John T. Newberg, Ph.D.
Professor in charge of dissertation

I certify that I have read this dissertation and that in my opinion it meets the academic and professional standard required by the University as a dissertation for the degree of Doctor of Philosophy.

Signed:

Andrew V. Teplyakov, Ph.D.
Member of dissertation committee

I certify that I have read this dissertation and that in my opinion it meets the academic and professional standard required by the University as a dissertation for the degree of Doctor of Philosophy.

Signed:

Karl S. Booksh, Ph.D.
Member of dissertation committee

I certify that I have read this dissertation and that in my opinion it meets the academic and professional standard required by the University as a dissertation for the degree of Doctor of Philosophy.

Signed:

Robert L. Opila, Ph.D.
Member of dissertation committee

ACKNOWLEDGMENTS

I received tremendous support from many people during my doctoral career and it was a privilege to share connections and ideas with each of you. First and foremost, I would like to give my sincere thanks and acknowledge my advisor, Dr. John Newberg, for his guidance and mentorship. The research achieved in this dissertation would not be possible if not for his support, advice, and suggestions. I am very grateful he afforded me the opportunity to conduct research at the University of Delaware. The knowledge, expertise, collaboration, and formulation of new ideas gained here will be carried forward into my professional career. Second, I would like to thank my dissertation committee members, Dr. Andrew V. Teplyakov, Dr. Karl S. Booksh, and Dr. Robert L. Opila, for all of their help and advice with my research. In addition, I would like to thank Dr. Thomas Beebe for sharing his knowledge and fruitful conversations. I would also like to thank Dr. Xiao Tong and Dr. J. Anibal Boscoboinik of Brookhaven National Lab for hosting and supporting my research performed there. Finally, I would like to thank the collaborators, Dr. Livia Giordano, and Dr. Anna M. Ferrari, I was fortunate enough to work with.

I would like to especially thank the members of Newberg group both current and former who provided me tremendous support and friendship, particularly Alicia Johnston and Yehia Khalifa. I give my thanks to the University of Delaware Surface Analysis Facility, specifically Dr. Thomas Beebe, Dr. Zachary Voras, and Chris Goodwin for providing XPS instrumentation and aid. The facilities and staff at the University of Delaware have been enormously helpful every day and provided

resource necessary for my research. From the support staff I thank Mr. Derrick Allen and Mr. Mark Schrader for their fabrication expertise and Mr. John Famiglietti, Mr. Moiscell Robinson, and Mr. Jim Draper for their technical and electronic expertise. I have to acknowledge Dr. Joe Smith and Dr. Mackenzie Lauro for their inspiration in science and in life. Dr. Scott Schuler and Dr. Baxter Abraham and all other members of the chemistry department for fostering comradery, sharing ideas, and help. I give my greatest thanks to Taozhu Sun for her motivation and unwavering encouragement. Lastly, I need to thank my family for their love and support throughout my life.

TABLE OF CONTENTS

LIST OF TABLES	x
LIST OF FIGURES	xi
ABSTRACT	xvii

Chapter

1	INTRODUCTION	1
1.1	Introduction to Surface and Heterogeneous Chemistry.....	1
1.2	X-ray Photoelectron Spectroscopy	2
1.3	Ambient Pressure X-ray Photoelectron Spectroscopy	8
1.4	Overview of Dissertation.....	11
2	LAB-BASED AMBIENT PRESSURE SYSTEM AND PERFORMANCE CHARACTERIZATION.....	14
2.1	Abstract.....	14
2.2	Introduction	14
2.3	Experimental Details	17
2.3.1	Sample Preparation and Methods	17
2.3.2	Lab-Based Ambient Pressure X-ray Photoelectron Spectroscopy (AP-XPS)	17
2.3.3	Hydrogen Plasma Process and Monitoring	22
2.4	Results and Discussion	22
2.4.1	System Performance in Vacuum and Under the Presence of Nitrogen Gas; Pressure Response and Signal Acquisition	22
2.4.2	Chamber Pressure Response to Hydrogen Plasma	31
2.4.3	Factors Influencing Signal Acquisition in Ambient Pressure X- ray Photoelectron Spectroscopy (AP-XPS).....	34
2.4.3.1	X-ray Windows and Spot Size	34
2.4.3.2	Gas Pressure and Aperture Size	37
2.4.3.3	Sample Contamination and Charging.....	39
2.4.3.4	Electrostatic Lens and System Pumping	41

2.4.3.5	Other Considerations	42
2.5	Conclusions	44
3	SURFACE SPECTROSCOPY OF ZINC BROMIDE INTERFACIAL CHEMISTRY DURING DELIQUESCENT	46
3.1	Abstract.....	46
3.2	Introduction	47
3.3	Experimental Details	53
3.3.1	Sample Preparation.....	53
3.3.2	Ambient Pressure X-ray Photoelectron Spectroscopy (AP- XPS)	53
3.3.3	Scanning Electron Microscopy (SEM).....	55
3.4	Results and Discussion	55
3.4.1	Effect of Water Adsorption on Zinc Bromide Surface Charge Compensation Through Dissolution and Ionic Mobility.....	55
3.4.2	Quantitative Analysis of Water Uptake with the Clausius- Claperyon Relation	61
3.4.3	Ion Segregation at the Liquid/Gas Interface: Evidence of Anion Surface Enhancement from Coordination with Water	71
3.5	Conclusions	74
4	HYDROXYLATION OF METAL OXIDE ULTRA-THIN FILMS SUPPORTED ON SILVER SINGLE CRYSTAL	76
4.1	Abstract.....	76
4.2	Introduction	77
4.3	Experimental Details	80
4.3.1	Sample Preparation.....	81
4.3.2	X-ray Photoelectron Spectroscopy (XPS).....	82
4.3.3	Scanning Tunneling Microscopy (STM).....	82
4.3.4	Low Energy Electron Diffraction (LEED)	83
4.3.5	<i>In-Situ</i> Water Exposures.....	83
4.4	Results and Discussion	84
4.4.1	Manganese Oxide Ultra-Thin Films on Ag(100)	84
4.4.1.1	Thin Film Deposition Characterization	84

4.4.1.2	Spectral Analysis of <i>In-Situ</i> Water Exposures	91
4.4.2	Nickel Oxide Ultra-Thin Films on Ag(100).....	94
4.4.2.1	Thin Film Deposition Characterization	94
4.4.2.2	Spectral Analysis of <i>In-Situ</i> Water Exposures	100
4.5	Conclusions	105
5	INVESTIGATION OF PHOTOCATALYTIC PROCESSES OF MANGANESE OXIDES	107
5.1	Abstract.....	107
5.2	Introduction	108
5.3	Experimental Details	110
5.3.1	Sample Preparation and Analysis	110
5.3.1.1	Native Manganese Oxide	110
5.3.1.2	Electrodeposited Manganese Oxide Film.....	111
5.3.2	Ambient Pressure X-ray Photoelectron Spectroscopy (AP- XPS)	111
5.3.3	X-ray Photoelectron Spectroscopy (XPS).....	112
5.3.4	Scanning Electron Microscopy (SEM) and Optical Microscopy	112
5.3.5	Xenon Light Exposure.....	113
5.4	Results and Discussion	114
5.4.1	Native Manganese Oxide Surface and Photocatalytic Behavior	114
5.4.1.1	Spectral Characterization of Initial Film	114
5.4.1.2	Manganese Oxide Chemistry in the Presence of Oxygen, Water, and Simulated Solar Light.....	116
5.4.2	Electrodeposited Manganese Oxide Film on Indium Tin Oxide (ITO) Synthesis and Photocatalytic Behavior	124
5.5	Conclusions	133
6	SUMMARY AND FUTURE WORKS.....	135
	REFERENCES	139

Appendix

A	COPYRIGHT PERMISSIONS	166
---	-----------------------------	-----

LIST OF TABLES

Table 3.1:	AP-XPS studies of solid salts exposed to humidity with experimental parameters of substrate, humidity exposure in relation being above, below, or going through the DRH during the experiment, use of variable X-ray energy to probe interfacial ion distribution, and location of the experiment.....	51
------------	--	----

LIST OF FIGURES

- Figure 1.1: Representation of the excitation of a core shell electron by X-ray irradiation and energy levels related to its ejection as a photoelectron..... 4
- Figure 1.2: Inelastic mean free path (λ_m) in angstroms as a function of the kinetic energy of the photoelectrons for various solid elements. Reproduced with permission from [6]..... 5
- Figure 1.3: Total electron scattering by hydrogen gas (1 mbar). The scattering cross-section and IMFP of the electrons are displayed as a function of their kinetic energy. Reproduced with permission from [7]. 7
- Figure 1.4: A schematic of a differentially pumped electrostatic lens system typical of modern AP-XPS systems. The electrostatic lenses focus the electrons onto the apertures between each differential pumping stage. The differential pumping stages reduce the pressure of gas the electrons increasing the mean free path and allowing more electrons to arrive at the detector. Reproduced with permission from [4]..... 9
- Figure 2.1: Diagram of electrostatic lens and pumping stages on the VG Scienta HiPP-2 R4000 and exchangeable analysis chamber with transparent X-ray window. Pressures presented are representative of pressures during a high-pressure experiment. 19
- Figure 2.2: Sample analysis geometry indicating the X-ray illumination spot (red) and XPS analysis collection area (green). The z-axis is the energy axis of the analyzer and N is the sample normal with the X-rays at 55° and analyzer at 20° . Sample to aperture distance denoted by the dashed arrow pointing from the X-ray spot to the aperture cone terminated with e^- 24

Figure 2.3:	Determination of AP-XPS analysis collection area (spot size of the analyzer field of view) on a silver foil. (a) Ag 3d (5/2) spectra at relative z-axis positions moving away from the center of the foil (i) 0, (ii) 0.75, (iii) 1.35, and (iv) 1.65 mm. (b) Normalized Ag 3d (5/2) spectra area as a function of z-axis position for acceleration (blue), transmission, (green) and angular (red) modes. Black lines represent 12 % and 88 % cutoffs for area and z-axis position. Reproduced with permission from [70].	27
Figure 2.4:	Ag 3d (5/2) signal intensity attenuation using nitrogen gas. (a) Relative Ag 3d (5/2) intensity as a function of analysis chamber pressure for acceleration (blue), transmission (green), and angular (red) modes. Inset displays exponential plot according to Equation 2.1. (b) Ag 3d (5/2) spectra collected in acceleration mode at (i) 10^{-4} , (ii) 1, (iii) 5, (iv) 10, (v) 15 and (vi) 20 Torr. Inset spectra (iv) to (vi) were normalized to give similar intensities. Reproduced with permission from [70].	29
Figure 2.5:	Stage 3 pressure (black) and Stage 1 turbo pump power (blue) versus analysis chamber pressure as N ₂ gas was introduced. Reproduced with permission from [70].	32
Figure 2.6:	Mass spectrometer response of the analysis chamber at 110 °C (blue), after 40 minutes of H ₂ plasma (0.001 Torr) at 110 °C, after vacuum evacuation at 21 °C (green).	32
Figure 2.7:	Metrics impacting lab-based AP-XPS signal and experimental quality. (a) X-ray transparent window, (b) X-ray spot size and flux onto sample, (c) gas phase pressure, (d) aperture diameter, (e) sample charging and contamination, (f) electrostatic lens system and pumping capacity. Reproduced with permission from [58].	35
Figure 3.1:	Representations of substrate configurations used in water adsorption experiments with AP-XPS (a) Concentrated salt solution deposited on substrate, evaporated under vacuum, and then exposed to humidity above deliquescence. (b) Salt single crystal exposed to humidity above deliquescence in vacuum to form continuous solution film. (c) Salt powder pressed pellet deliquesced in vacuum to form continuous solution film. (d) Thin film of salt exposed to humidity above deliquescence creating discontinuous droplets of salt solution.	48

Figure 3.2:	Optical images taken of the sample during the $-3.5\text{ }^{\circ}\text{C}$ isotherm where A and B correspond to the pressures of 4.0×10^{-8} and 0.61 Torr, respectively. Image C was SEM image taken using secondary electron imaging detector and with a 3.00 kV electron beam and 40x magnification.....	57
Figure 3.3:	Survey spectrum of ZnBr_2 film on Au foil under vacuum.....	58
Figure 3.4:	(a) Zn 2p(3/2) spectra displayed with increasing RH from the $-3.5\text{ }^{\circ}\text{C}$ isotherm. Spectra of i-v correspond to a RH of $1 \times 10^{-6}\%$, 1.4 %, 2.9 %, and 6.6 % respectively. (b) plots the binding energy shift Zn 2p(3/2) of the isotherms as a function of RH. (c) FWHM values of Zn 2p(3/2) as a function of RH.....	59
Figure 3.5:	O 1s spectra displayed are from the $8.0\text{ }^{\circ}\text{C}$ isotherm at the pressure of 3.3×10^{-8} , 7.6×10^{-2} , and 1.2 Torr corresponding to 4.1×10^{-7} , 8.8×10^{-1} , and 15%RH, respectively, shown from top to bottom.	63
Figure 3.6:	Hi resolution spectra of C1s of $-3.5\text{ }^{\circ}\text{C}$ isotherm. C 1s components were constrained to a full width at half maximum equivalent among each component at a value of $\sim 1.1\text{ eV}$. The aliphatic carbon has a binding energy of 285 eV, while alcohol and carbonyl functional groups are shifted by +0.94 and +1.16 eV respectively. Other components were not observed in the C 1s spectra.....	64
Figure 3.7:	The molar ratio of adsorbed water to zinc atoms of each isotherm plotted as a function of relative humidity.....	65
Figure 3.8:	(a) Plots of the $\ln P$ vs. $1/T$ (K) of mole fractions of adsorbed water and the linear least squares regression through the three temperatures. (b) The enthalpy of water adsorption plotted as a function of water mole fraction in the ZnBr_2 system.....	69
Figure 3.9:	Internal relative binding energy shifts (a) Br 3d(5/2) and Zn 2p(3/2) spectra at pressures of 1.8×10^{-8} and 2.5 Torr, corresponding to 7.0×10^{-7} and 14 % RH, respectively. (b) BE difference of the Zn 2p(3/2) and Br 3d(5/2) as a function of RH.	71
Figure 3.10:	The anion to cation ratio is plotted as a function of RH. The molar ratio of the Zn 3p to Br 3d of the UHV spectra was the baseline percentage increase.....	72

Figure 4.1: STM of cleaned silver, sputtered and annealed at 700K. 50x50 nm images collected at 0.96 V and 0.53 nA. Reproduced with permission from [221].	84
Figure 4.2: LEED images of (a) clean Ag(100) and (b) MnO film annealed to 700 K in vacuum. Images taken at 86 eV. Reproduced with permission from [221].	85
Figure 4.3: STM results of a freshly prepared MnO film annealed in vacuum to 800 K. (a) 200 x 200 nm image collected at -2.0 V and 0.40 nA. (b) Apparent height profiles of line traces within STM image. Reproduced with permission from [221].	87
Figure 4.4: XPS spectra of MnO/Ag(100) film at different experimental conditions (a) Mn 2p(3/2) and (b) O 1s XPS spectra taken of (i) silver substrate, (ii) as deposited film of MnO, (iii) after 5-minute exposure to 9.0×10^{-3} Torr H ₂ O and (iv) after exposure to 2.5 Torr H ₂ O. Reproduced with permission from [221].	88
Figure 4.5: XPS C1s spectra of (a) silver substrate, (b) as deposited MnO film, (c) after exposure to 9.0×10^{-3} Torr H ₂ O for 5min and (d) after exposure to 2.5 Torr water vapor for 5 min. Reproduced with permission from [221].	90
Figure 4.6: Ratio of XPS OH to Ox peak intensities for the initial MnO film, after exposure to 9.0×10^{-3} Torr H ₂ O, and after exposure to 2.5 Torr H ₂ O. Water exposures were 5 min. Reproduced with permission from [221].	92
Figure 4.7: (a) STM image of NiO film collected at +2.5V and 0.5 nA. The principal crystallographic directions are indicated. (b) Topological plot of white line in (a). Reproduced with permission from [222].	96
Figure 4.8: LEED image of an annealed NiO(100) film collected at 88 eV. Reproduced with permission from [222].	97
Figure 4.9: Ni 2p(3/2) spectra of NiO (a) initial film. (b) An overlay of three spectra, the initial film (black) and after 0.009 Torr (red) and 2.5 Torr (blue) water vapor exposures. Reproduced with permission from [222].	98
Figure 4.10: O 1s spectra of NiO (a) initial film, (b) after exposure to 0.009 Torr and (c) 2.5 Torr water vapor. Each exposure was for 15 min. Reproduced with permission from [222].	99

Figure 4.11: Ratio of the oxide (Ox), hydroxyl (OH) and molecularly bound water (H ₂ O) peak to the total O 1s peak area as a function of sample condition. Water vapor exposures were 15 min. Reproduced with permission from [222].	101
Figure 4.12: C 1s spectra of initial NiO film (black) and after water vapor exposures to 0.009 Torr (red) and 2.5 Torr (blue). Reproduced with permission from [222].	103
Figure 5.1: Oxygen 1s spectra taken of the (a) initial sample of the native oxide film on Mn, (b) illuminated for 2 hours, (c) under 0.09 Torr O ₂ illuminated for 1 hour, and (d) 2 hours. Components fit to the oxide (Ox), hydroxyl (O-H), oxygenated carbon species (O-C), and adsorbed water (H ₂ O).	115
Figure 5.2: C 1s spectra taken of the (a) initial sample of the native oxide film on Mn, (b) illuminated for 2 hours, (c) under 0.09 Torr O ₂ illuminated for 1 hour, and (d) 2 hours. Components fit to the advantageous carbon (CH), alcohol(C-OH), ketone (C=O), and carboxyl(COOH) species of the C1s.	116
Figure 5.3: Mn 2p spectra offset of the (a) initial sample of the native oxide film on Mn, (b) illuminated for 2 hours, (c) under 0.09 Torr O ₂ illuminated for 1 hour, and (d) 2 hours. (e) the difference between (a) and (d).	117
Figure 5.4: Mn 3s splitting of the initial sample of the native oxide film.	119
Figure 5.5: Relative abundance of oxygen and carbon species from (a) O 1s and (b) C 1s spectra taken of the initial sample of the native oxide film on Mn, 2-hour illumination, and under 0.09 Torr O ₂ illuminated for 1 and 2 hours.	122
Figure 5.6: Cyclic voltammograms of an ITO glass electrode in a solution of 0.10 M MnCl ₂ with a scan rate of 10 mV/s.	125
Figure 5.7: SEM images of electrodeposited MnO ₂ on ITO taken at (A) 30,000x and (B) 100,000x magnification.	126
Figure 5.8: Optical image of electrodeposited MnO ₂ film on ITO.	127
Figure 5.9: XPS survey spectra of electrodeposited MnO ₂ film on ITO. Principle peaks are labeled.	127
Figure 5.10: XPS spectra taken at the (a) In 3d and (b) Sn 3d regions.	128

Figure 5.11: Mn 2p(3/2) XPS spectra of the electrodeposited MnO ₂ film on ITO. Components fit to the contributions of Mn ³⁺ (red) and Mn ⁴⁺ (blue) oxidation states.	129
Figure 5.12: O 1s XPS spectra of the electrodeposited MnO ₂ film on ITO. Components fit to the oxide (Ox), hydroxyl (O-H), and adsorbed water (H ₂ O).	130
Figure 5.13: Transient photocurrents of MnO ₂ /ITO in 0.1 M KCl under Xenon light illumination at a 0 V bias potential.	132
Figure 5.14: UV-Vis spectra taken of the degradation of 200 uM methylene blue in solution with MnO ₂ particles during exposure to Xenon light. Inset shows absorbance degradation at the wavelength 660 nm.	132

ABSTRACT

In recent years there has been a significant drive in the surface science to investigate heterogeneous processes under realistic conditions. In this dissertation the quantification and analysis of heterogeneous systems were explored by a variety of techniques to elucidate complex electronic and chemical properties of surfaces in the presence of fundamental gases. In particular, photoelectron spectroscopy operated under ambient pressures was employed to assess chemical reactions and phase transitions of model and applied surfaces. Specifically, this dissertation will focus on the impact of adsorption of water and oxygen on interfacial compositions of salt and metal oxide surfaces. First the extremely hydroscopic system of zinc bromide was investigated as a function of relative humidity with high pressure photoelectron spectroscopy. Advanced analysis of isothermal water uptake yielded results which quantified the energetics of adsorption. Innovative assessment of surface composition with lab-based photoelectron spectroscopy produced findings previously limited to synchrotron-based techniques. Second, the effects of water adsorption upon epitaxial metal oxide films structural relaxation through hydroxylation were investigated. Evidence based on experimental and theoretical observations suggest that various mechanisms of water dissociation may exist between manganese and nickel oxide films but also that the adsorption of water dimers at higher pressures significantly alters the reaction mechanism, promoting further hydroxylation events. Lastly, the photocatalytic properties of manganese oxides were explored under reaction

conditions with exposure to light, water, and oxygen gases. Insights were made into the mechanisms of photo reactions with carbonaceous species with implications in photocatalysis. Overall this dissertation strives to highlight the analysis of complex heterogeneous systems with surface sensitive techniques focusing on *in-operando* conditions that are of broad interest to the surface science community and to provide enhanced understanding of important gas adsorption processes.

Chapter 1

INTRODUCTION

1.1 Introduction to Surface and Heterogeneous Chemistry

The field of surface science has made tremendous advancements over the past century. Many characteristics of material surfaces have been elucidated, such as the atomic and electronic structure, reactivity, and chemical dynamics thereof. Pioneering work of surface scientists has been globally recognized resulting in several Nobel prizes from the likes of I. Langmuir in 1932 to G. Ertl in 2007, highlighting the critical importance that surface chemistry plays in the scientific community. The use of ultra-high vacuum (UHV) environments in the experimental investigation of surfaces have constrained the implementation of many surface science imaging and spectroscopy techniques to preclude the study of interfaces under higher pressures. Scientists have studied adsorption of gas phase molecules on substrates with cryogenic temperature experiments to reach quantifiable coverage of weakly bound adsorbates. However, under real world conditions most heterogeneous surfaces are in contact with gases and liquids at or above ambient pressures and temperatures. When considering these realistic conditions of surfaces of interest are expected to be covered with condensed layers of adsorbates in equilibrium with the gas phase while also being at ambient temperatures or higher, which can drastically impact kinetic processes that cryogenic temperature studies are unable to access [1]. The structure of surfaces can be very different under ambient conditions from samples under high vacuum when observed with traditional surface characterization techniques. Thus, there has been concerted

effort made to push the boundaries of surface science to study heterogeneous phenomena under relevant temperatures and pressures with major strides being made to the instrumentation of numerous techniques to accommodate the measurement of samples under elevated conditions.

This dissertation focuses primarily on heterogeneous systems containing gaseous water adsorption events. Water is a ubiquitous adsorbate on most surfaces with major relevance in many environmental, atmospheric, and industrial systems. The interactions of water on surfaces have been the focus of numerous surface science researchers over the years, the results of their investigations summarized have been in prominent reviews by Thiel and Madey [2] and Henderson [3] with efforts ongoing to its continued study. Water adsorption over most surfaces starts with the adsorption of monomers, progresses to the formation of monolayers, and subsequent condensation of bulk water and has the potential to react with the surface changing the chemical properties of the material [4]. Quantification and assessment of the behavior of water at the interface of surfaces is critical to the understanding processes occurring within the environment, heterogeneous catalysis, electronic devices, and biological systems. This dissertation will examine heterogeneous water adsorption upon insulator and semiconductor surfaces of salts and metal oxides which serve as important substrates in many of these important processes.

1.2 X-ray Photoelectron Spectroscopy

Photoelectron spectroscopy is among the most suitable approaches used to investigate the electronic and chemical composition of solid surfaces. The concept of photoelectron spectroscopy is based on the photoelectric effect postulated by Einstein, wherein the photons of light can interact with an electron in an atom and if they

possess sufficient energy can emit the electron from a material. A Swedish scientist named Kai Siegbahn demonstrated the use of an instrument which could detect photoelectrons as an analytical tool to probe surface chemistry in the 1960's [5]. Kai Siegbahn was awarded the Nobel Prize in Physics in 1981 for his efforts in the development of high-resolution electron spectroscopy. The instrument caused the excitation of core shell electrons from solid samples using characteristic X-rays causing their emission and their subsequent detection with energy dispersive electron analyzers revealed chemical information that was dependent on the photoelectron's kinetic energies. The interpretation of these results led to the technique being initially termed electron spectroscopy for chemical analysis (ESCA), now more often referred to as X-ray photoelectron spectroscopy (XPS).

Today, XPS is one of the most common surface sensitive experimental techniques due its powerful utility of combining atomic and chemical specificity with submonolayer quantitative sensitivity. XPS utilizes high energy X-ray photons to irradiate the surface of a sample leading to the ejection of photoelectrons from atomic core shell orbitals that are detected based on their kinetic energy (**Figure 1.1**). The theoretical model of the photoemission mechanism was developed by Berglund and Spicer wherein the process is described as a three-step model. This approach proceeds as follows, first the optical excitation between ground and final Bloch states, then transit of the electron to the surface interface, and finally the escape of the electron through the surface into the vacuum.

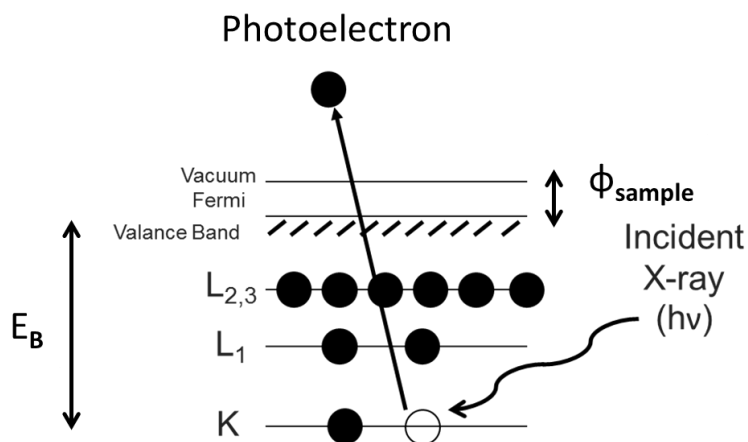


Figure 1.1: Representation of the excitation of a core shell electron by X-ray irradiation and energy levels related to its ejection as a photoelectron.

The probability of an electron adsorbing light energy to transition from a ground to free state is dependent on the photoionization cross-section which is related to the photon energy, atom, and electron orbital. The surface sensitivity XPS results from the strong interaction of electrons with matter which occurs during the second step of the model as the electron travels to the surface. Photoelectrons which experience an inelastic collision with matter lose kinetic energy may still be detected by XPS and arise as artifacts of the spectra, i.e. Bremsstrahlung radiation, or the photoelectrons may experience enough collisions to never escape the sample surface. The main advantage of XPS is its sensitivity to the material surface because the photoelectrons which are detected are emitted from only the top few nanometers of the sample interface. The low inelastic mean free path (IMFP) of electrons traveling through a solid (**Figure 1.2**) only permit photoelectrons escaping from the outermost sample surface (1-10 nm) to reach the detector unimpeded by collisions with surrounding atoms .

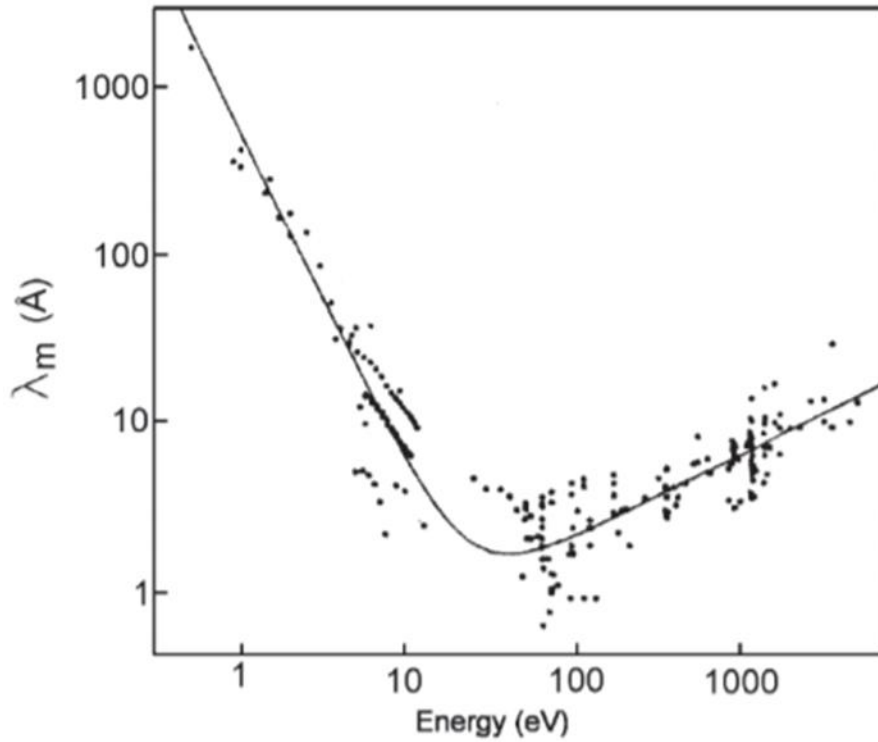


Figure 1.2: Inelastic mean free path (λ_m) in angstroms as a function of the kinetic energy of the photoelectrons for various solid elements. Reproduced with permission from [6].

In the final step of the model to cross the surface the electrons must overcome a potential barrier known as the work function. The work function is defined as the amount of energy required to get the electron from the Fermi level into the vacuum, where it is free from any influence of its parent atom. Taking the work function into

account the energy of the emitted photoelectron can be determined from the law of conservation of energy is given by equation (1.1)

$$E_{K^*} = h\nu + E_B + \phi_{sample} \quad (1.1)$$

where E_K is the kinetic energy (KE) of the ejected electron, $h\nu$ is the energy of the incident photon, E_B is the binding energy (BE) of the core electron and ϕ_{sample} is the work function of the sample. The BE is defined as the amount of energy needed to free an electron from its orbital and is dependent on the element as well as the chemical environment surrounding the atom. The effect of the chemical environment around the atom results in a small change in the BE of the emitted photoelectron known as a chemical shift in the XPS spectra. The chemical shifts in XPS are generally distinct from the principle peak with well-defined energy differences that enable the assignment of oxidation states or chemical species present within the sample. In Equation (1.1) the BE is measured with respect to the Fermi level of the sample, however, experiments performed within this dissertation used a sample holder and hemispherical analyzer that were grounded together through the same electrical cable. This configuration is used to prevent sample charging and aligns the Fermi level of the sample to that of the analyzer. Thus, the resulting measured kinetic energy of photoelectrons must only consider the work function required for the electron to enter the analyzer, eliminating the variability of ϕ_{sample} from sample to sample, and is defined by Equation (1.2)

$$E_{K^*} = h\nu + E_B + \phi_{analyzer} \quad (1.2)$$

where $\phi_{analyzer}$ is the work function of the analyzer.

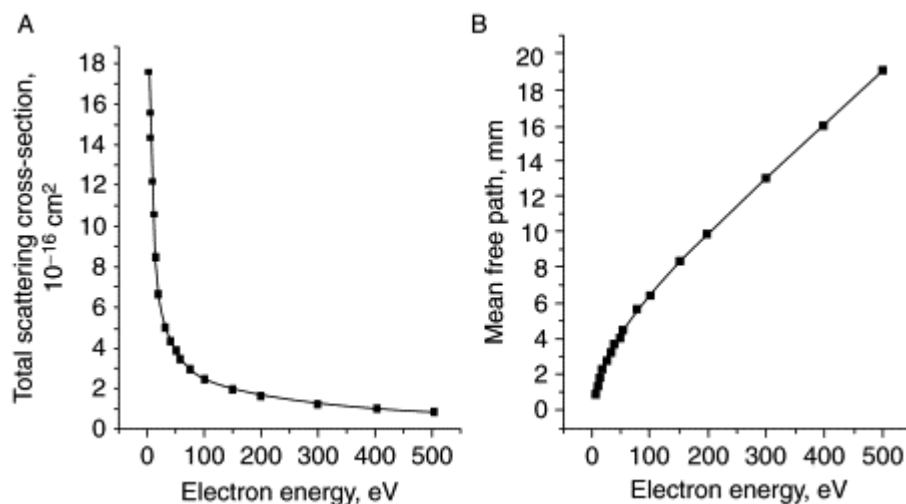


Figure 1.3: Total electron scattering by hydrogen gas (1 mbar). The scattering cross-section and IMFP of the electrons are displayed as a function of their kinetic energy. Reproduced with permission from [7].

XPS has predominantly been operated under UHV conditions. There are several reasons why UHV environments were utilized in XPS instrumentation. Firstly, the design of X-ray anodes and electron analyzers need high vacuum levels to operate. The electrons must also travel distances on the order of 1 meter to reach the analyzer and due to the large scattering cross section between electrons and gas phase molecules UHV conditions are required to stretch the mean free path of the electrons out beyond this distance for sufficient detection (**Figure 1.3**) [7]. Lastly the UHV pressures preserve the sample surface from potential contamination during the lifetime of an experiment. If one assumes a sticking coefficient of 1, than a typical surface is covered by a monolayer of gas molecules in approximately one second at a pressure of 10^{-6} Torr (1 Langmuir). Gas contaminations at the ppm or even ppb level can poison a sample in the same time it takes to collect a spectrum. UHV pressures on the order of

10^{-10} Torr and below allow for the sample to remain at contamination levels acceptable for quantifiable XPS analysis. This constraint of UHV chamber pressure limited the study of XPS to solids of low vapor pressure and a complete lack of heterogeneous systems to be studied without the aid of cryogenic sample holders to condense gases or extremely low-level dosages of gases.

1.3 Ambient Pressure X-ray Photoelectron Spectroscopy

Since the early development of XPS, K. Siegbahn recognized that the UHV environment in XPS instrumentation would significantly limit its applications to the solid-vacuum interface. In the late 1960's, Siegbahn and coworkers began to take XPS spectra of gases through the advent of differential pumping [8]. This was followed by the pursuit of examining low volatility liquids in the early 1970's [9] by K. Siegbahn and H. Siegbahn. These foundational studies were the birth of what is often referred to as ambient pressure XPS (AP-XPS), which combines the powerful utility of conventional UHV XPS with the ability to analyze samples in the presence of a surrounding gas. From the early development of the instrumentation Kai Siegbahn recognized that the UHV environment essential in conventional XPS machines were limiting the applications of this technique to the solid vacuum interface. Thus, developments such as differential pumping were made to the instrumentation to limit the electrons scattering through the gas phase, to enable the study of liquids [8,9]. Over the past few decades several advancements to the instrumentation have allowed AP-XPS systems to probe interfacial surfaces at higher pressures. These advancements include the development of a differentially pumped electrostatic lens, X-ray transparent windows, and collection apertures, (**Figure 1.3**) enabling photoelectron measurements to “bridge the pressure gap” and study interfacial systems at near

ambient pressures [1,10-12]. These developments significantly limit the distance that photoelectrons travel through the high-pressure gas phase allowing the spectrometer to efficiently collect signal despite the short IMFP of the electrons. Each successive differential pumping stage are separated by small apertures and serve to lower the pressure from the previous stage while the electrostatic lenses accelerate the photoelectrons through the gas phase and focus them through the apertures.

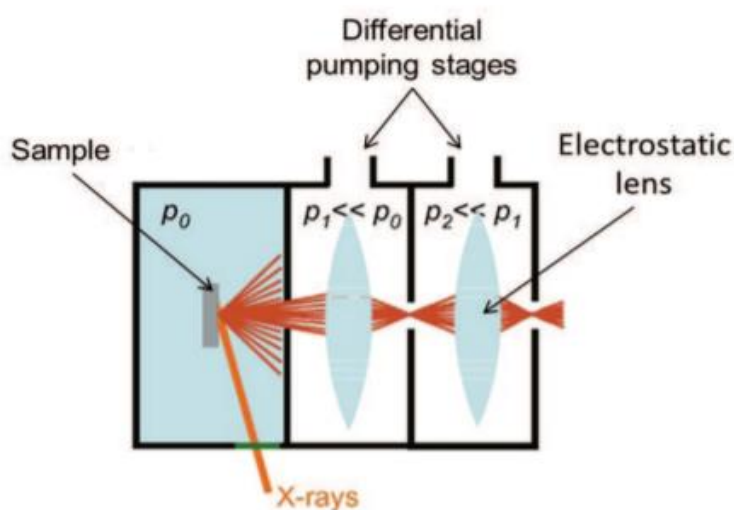


Figure 1.4: A schematic of a differentially pumped electrostatic lens system typical of modern AP-XPS systems. The electrostatic lenses focus the electrons onto the apertures between each differential pumping stage. The differential pumping stages reduce the pressure of gas the electrons increasing the mean free path and allowing more electrons to arrive at the detector. Reproduced with permission from [4].

AP-XPS systems are presently commercially available and growing in demand with instruments disbursed at synchrotrons and laboratories around the world. AP-XPS allows for samples to be probed under large ranges of temperature and pressure,

ranging from UHV up to 20 to 30 Torr. Such capabilities allow for the molecular level probing of solid-gas, liquid-gas and solid-liquid interfaces under ambient conditions. This surface science technique is a powerful, multidisciplinary tool as evidenced from a number of reviews over the past decade utilizing AP-XPS in catalysis [13-21], solid-gas interfaces [4,10,22,23], aerosols [24], energy materials [25], dielectric oxides [26], operando spectroscopy [27-32], electrochemistry and solid-liquid interfaces [33-40]. In addition, the technical developments, practical considerations and instrumental achievements of synchrotron-based and lab-based AP-XPS systems have been highlighted in a number of reviews [1,11,12,41-45]. The description of the AP-XPS within the Newberg Lab is presented in Chapter 2 on which much of the work within this dissertation was conducted, alongside discussion of system performance and exploration into the sources of signal loss present in near ambient pressure experiments.

The field of AP-XPS is ever expanding in both the science it pursues and the development of instrumentation that drives forward advances leading to new insights into important systems. To date lab-based AP-XPS systems have used either Al (1486.6 eV) or Mg (1253.7 eV) K_{α} X-ray sources. In line with recent developments of synchrotron-based AP-XPS being coupled to tender [46,47] and hard [48] X-ray sources, the use of higher energy lab-based X-ray sources would also be a power addition to the lab-based AP-XPS community. For example, a UHV XPS system has incorporated both an Al K_{α} (1486.6 eV) source and an Ag $L_{\alpha'}$ (2984.6 eV) source [49]. Coupling a Cr K_{α} (5.4 keV) X-ray source is also a possibility [50]. Such capabilities would allow for deeper sample probing with the ability to examine the solid-liquid interface of electrodes [51]. A complementary push is also being made to

be able to probe the solid-liquid interface via lab-based AP-XPS through the development of graphene membranes [52,53]. In addition to having two X-ray sources, having two analyzers, one vertically oriented and the other horizontally orientated, could offer advantages of probing a fixed sample at normal versus grazing angles. While such a system may have geometric constraints with two electrostatic lens analyzers, there does exist a UHV XPS system with this philosophy [54]. There also exists a movement toward automated operation of lab-based AP-XPS where most previous AP-XPS systems have been almost entirely manually operated by a skilled technician. The automated system is sophisticated enough to handle sample entry, manipulation, focusing, and gas handling which allows these types of system to function with faster sample turnover and less demand on the user. [55] Greatly expanding upon the ease of use could be an avenue to pursue, in hopes to potentially increase the type of research conducted and add new fields to the already established communities that utilize AP-XPS.

1.4 Overview of Dissertation

As the introductory sections would suggest, this dissertation focuses on the study of heterogeneous processes, primarily with photoelectron spectroscopy. The advent of so called ambient pressure X-ray photoelectron spectroscopy has enable the study of many heterogeneous interactions *in-situ* with extreme surface sensitivity. Within Chapter 2 the design and functionality of AP-XPS is discussed alongside foundational experiments assessing the performance and important metrics of the instrument. This dissertation looks to elucidate fundamental heterogeneous processes between a gas phase and semiconductor surface, particularly that of salts and metal oxides. The gases of interest being studied are chiefly water, a ubiquitous molecule

throughout the world, as well as oxygen. The interactions of these molecules with surfaces are involved in critical mechanisms in many important processes within the environment and technology.

In Chapter 3 the adsorption of water onto the hygroscopic salt of zinc bromide was investigated as a function of relative humidity with high pressure photoelectron spectroscopy. The solid/vapor and liquid/vapor interface between salt and water are important systems in the environment and therefore are a subject of fundamental interest. Isothermal experiments produced data sets which could be used to quantify the energetics of adsorption. Many questions remain on the behavior of ions present at the interface of a salt solution with vapor, as various ionic species have been shown to behave differently. The zinc bromide interface was probed with lab-based photoelectron spectroscopy to elucidate the nature of the anion and cation surface distribution. An anionic concentration enhancement was observed for the bromide species, in line with its chaotropic classification.

In Chapter 4, the interaction of water adsorption upon epitaxial metal oxide films supported on silver substrates was investigated. Thin-film semiconductor structures are the basis for a large part of modern electronics and have applications ranging from electrochemistry, gas sensing, to catalysis. Evidence based on experimental and theoretical analysis suggests that hydroxylation events occur on manganese and nickel oxide films that may be dependent on relative humidity and time. The chemical reactions occurring on the surfaces of films can alter properties of the film both to its benefit or detriment. The abundance of water in every environment lends its adsorption properties to be of great interest for fundamental research. The hydroxylation of the films, which was observed, differed from the literature of the

bulk material in the case of nickel oxide. The extent of water adsorption on the films leading to dissociation was in good agreement with studies of other transition metal oxide film hydroxylation reactions where the participation of water dimers is energetically favored to produce hydroxyls.

Within Chapter 5, the chemical properties of manganese oxides were investigated aimed at heterogeneous interactions involved in photocatalytic reactions. Exposures to photoreactive conditions were applied to manganese oxides of different structure and oxidation states were explored. The surfaces of naturally occurring oxide overlayers on manganese and electrodeposited manganese oxide films were characterized and evaluated for photocatalytic capacity. Lastly, Chapter 6 summarizes the main conclusions and future directions related to the fundamental heterogeneous chemistry described in this dissertation.

Chapter 2

LAB-BASED AMBIENT PRESSURE SYSTEM AND PERFORMANCE CHARACTERIZATION

2.1 Abstract

Within this chapter the design of a lab-based Ambient pressure X-ray photoelectron spectroscopy (AP-XPS) system with the capability to exchange its small volume analysis chambers is described. AP-XPS is a powerful spectroscopy tool that is able to bridge the pressure gap and probe sample surfaces under heterogeneous environments. The Ag 3d(5/2) core shell of a silver foil standard was analyzed at room temperature to determine several characteristic parameters of the instrument using three different electrostatic lens modes: angular, transmission, and acceleration. Ag 3d(5/2) peak attenuation, differential pumping stage pressures, and pump work load were assessed under varying N₂(g) analysis chamber pressures of up to 20 Torr. Efforts made to improve chamber base pressure and to remove contaminants through high temperature baking and plasma cleaning were examined through pressure gauge measurement and mass spectrometry. The aspects inherent to AP-XPS instrumentation and technique which affect signal acquisition efficacy under high pressures are outlined and the interconnected nature of the parameters are delineated.

2.2 Introduction

X-ray photoelectron spectroscopy (XPS) is a powerful tool that is both elemental and chemical specific and that has the ability to probe changes in electronic

states of surfaces with submonolayer resolution. Traditionally XPS has been performed under UHV conditions to enable the operation instrumental components, such as multichannel plates in the analyzer and detection of electrons with short mean free paths through elevated gas phase pressures. This constrained the use of XPS to the investigation of the solid/vacuum interface which provides incomplete information on the systems of study. The interface between a surface of a solid and a liquid or a gas phase, plays a prominent role in numerous industrial processes and technological entities, such as coating deposition, plasma etching, thin film depositions, magnetic and optical devices, electrochemical processes on electrodes, sensors and catalysis, as well as environmental and atmospheric processes [4,10,13,56,57].

To overcome the obstacle of pressure, or to “bridge the pressure gap” between UHV and Torr level environments, newer generation ambient pressure XPS (AP-XPS) electron spectrometers incorporate a lens system whereby the mean free path of the electrons ejected from the sample surface in the analysis chamber is lowered in most systems by bringing a cone shaped aperture (typically ~0.3 to 1.0 mm diameter) within close proximity of the sample surface [58]. Behind this initial aperture is a differentially pumped electrostatic lens system that transitions the electrons from the sample analysis chamber environment at Torr level pressures, to the electron energy analyzer under UHV conditions. The pressure drop behind the first aperture is several orders of magnitude and the amount of electron scattering by gas molecules decreases dramatically. In AP-XPS systems, the majority of the scattering occurs within the high-pressure region between the aperture and the sample. Operating under Torr level pressures in the analysis chamber also allows for gas-surface adsorption studies at

elevated temperatures, thus overcoming the “temperature gap” from cryogenic to ambient conditions mentioned in Chapter 1.

There has been a tremendous growth in APXPS studies as evidenced by reviews, reports and book chapters utilizing this technique in energy and environmental research [4,12-15,23,24,27-29,33,59-68]. However, most of these studies have been confined to the synchrotron research setting where the newest generation of APXPS technology has been developed. A synchrotron offers advantages over a laboratory X-ray source, including the ability to vary the X-ray energy, allowing for X-ray absorption studies and shallow probing depths. However, synchrotron APXPS systems also have disadvantages, being bound by limited beamtimes and, depending on the beamline, large X-ray fluxes which can be damaging to samples that are conducive to beam damage [69]. A comprehensive review of lab-based AP-XPS systems has been offered by Arble et al. [58], that provides detailed history on the development of AP-XPS instrumentation and which highlights unique results from heterogeneous chemical systems investigated within these systems.

This chapter illustrates the design and results of commissioning experiments for a lab-based APXPS system within the Newberg group at the University of Delaware. Many experimental details related to AP-XPS instrumentation used within the subsequent Chapters 3 and 5 are provided within this section. This system was designed with the removable chamber concept, allowing for the sample analysis chamber to be swapped with different analysis chambers that can be customized to a particular experiment. In this Chapter results of instrument operation under vacuum conditions and in the presence of $N_2(g)$ up to Torr level pressures are presented as well

as vigorous discussion of signal collection efficiency and vacuum base pressure procedures, reproduced with permission from [58,70].

2.3 Experimental Details

2.3.1 Sample Preparation and Methods

The following data were captured by examining the Ag 3d(5/2) peak at 368.3 eV [71] of a high purity silver foil (Alfa Aesar, 99.998%, 0.25 mm thick). Prior to analysis the foil was physically scraped with a blade to expose a fresh Ag surface. In some cases, the foil was additionally sputtered within the analysis chamber. All measurements were done with an angle of 70° from X-ray incidence to electron detection. The electrostatic lenses and analyzer were positioned 20° relative to the sample normal. Spectra for **Figure 2.2** and **2.4** were collected using a 0.8 mm curved slit and 100 eV pass energy. Spectra for **Figure 2.5** were collected 0.8 mm curved slit, 200 eV pass energy and a 3-minute acquisition. The spectra within **Figure 2.5** attained at 20 Torr N₂(g) was collected for 4.5 hours.

2.3.2 Lab-Based Ambient Pressure X-ray Photoelectron Spectroscopy (AP-XPS)

This section describes the instrumentation of the AP-XPS system used for experiments within this dissertation, full details of the system can be found in Newberg et al. [70]. The electron analyzer is a VG Scienta HIP-2 R4000, a combination of a 200 mm mean radius high resolution analyzer[72] and an electrostatic lens system (**Figure 2.1**). The lens is pumped in two different zones, Stage 1 (green) and Stage 2 (yellow). The receiving lens is pumped by Stage 3 (teal) while the dome is pumped by Stage 4 (grey). The analysis chambers were designed to

be interchangeable and are attached to an adaptor on the HIPP-2 R4000. The high-pressure zone (brown) is the sample analysis chamber and is separated from the electrostatic lens by a small differentially pumped aperture.

The hemispherical analyzer possesses nine interchangeable slits positioned on a rotating wheel which range from 0.2 mm to 4 mm in the energy dispersive direction and operates at pass energies of 50, 100 and 200 eV. The analyzer can operate in several modes, including angular, transmission, and a “swift” acceleration mode[73] (here after referred to as “acceleration mode”). The MCP/CCD electron detector includes a 40 mm diameter MCP that is used to illuminate a phosphor plate whose light intensity is captured 70 frames s^{-1} CCD camera; the signal collected by the system is outputted as a 2D array. The transmission and angular lens modes collect the information of photoelectron energy along one axis of the 2D image and preserve the spatial and angular information of the photoelectrons on the other axis, respectively. The pre-lens is separated from the high-pressure analysis chamber using exchangeable cone-shaped titanium apertures with diameters of 0.3 mm, 0.5 mm, or 0.8 mm. The data presented within this dissertation were collected with the 0.5 mm aperture. The effects of aperture size on APXPS signal as a function of pressure for the HIPP-2 R4000 has been described previously [74]. It should be noted that the 0.3 mm aperture performs better at higher pressures and that the 0.8 mm aperture performs better under vacuum conditions with the 0.5 mm being of medium efficiency over the vacuum to high pressure ranges the instrument operates under.

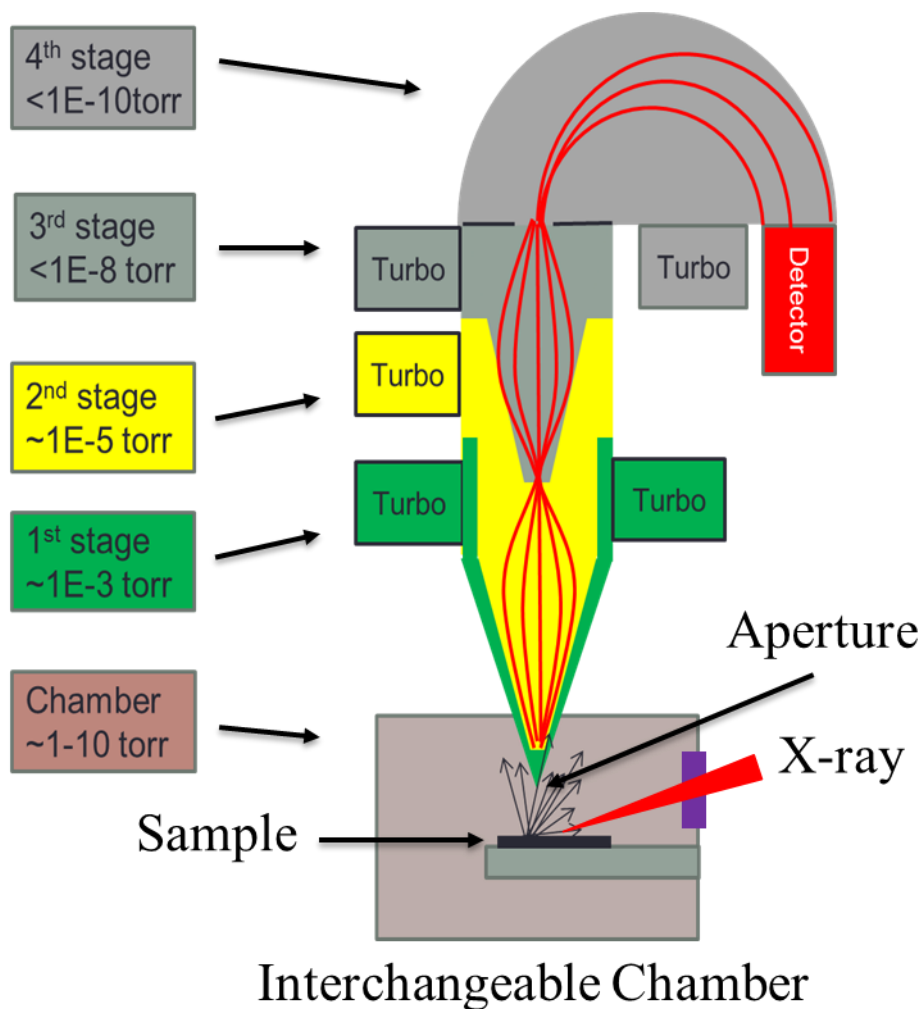


Figure 2.1: Diagram of electrostatic lens and pumping stages on the VG Scienta HiPP-2 R4000 and exchangeable analysis chamber with transparent X-ray window. Pressures presented are representative of pressures during a high-pressure experiment.

The monochromatic X-ray source (VG Scienta, MX650) consists of a 200 W (10 kV/20 mA) Al K_{α} anode (1486.7 eV) and X-ray monochromator with seven toroidal α -quartz crystals arranged in a close-packed array and mounted on a 650 mm dia. Rowland circle. The crystals are kept at a constant temperature of 55 °C to prevent thermal drift, due to ambient room temperature variations from affecting quartz crystal lattice spacing, thus maintaining a constant K_{α} photon energy and Bragg refraction angles.

The APXPS system is pumped by a suite of seven turbo pumps (Agilent, TwisTorr 304FS). One is dedicated to the monochromator, and six are dedicated to the analyzer, with two on Stage 1, two on Stage 2, one on Stage ,3 and one on Stage 4. A separate lower capacity turbo (Pfeiffer, 56 L s⁻¹ N₂) was used to pump on the analysis chamber; this pump has since been replaced by a higher capacity turbo. The system also uses three dry scroll pumps (Agilent, TriScroll 600); each of the scroll pumps were dedicated to the provide vacuum to the backing lines of the turbos, the isolated differentially pumped portions of the chamber, and the gas delivery lines. A suite of seven pressure gauges were monitored by one controller (Agilent, XGS-600), including two ion gauges (Agilent, UHV-24) on Stage 3 and the monochromator, a cold cathode (Agilent, IMG-300) on the sample analysis chamber, and four convection enhanced thermal gauges (Agilent, ConvecTorr) to measure foreline and gas delivery system pressures. Absolute pressures in the analysis chamber were measured by a capacitance manometer (MKS, 626B) or baratron gauge, depending on the pressure range during an experiment.

The vertical position of the electrostatic lenses and analyzer which 20° off the lab floor normal accommodates samples sitting parallel to the lab floor, allowing for

the study of both solids and liquids. The sample can be rotated by 30° relative to the sample normal, allowing for the largest collection (and most surface sensitive) angle of 50°. The limitation of sample rotation is due to the aperture cone in the analysis chamber; rotating it further causes a collision of the sample holder with the aperture.

The monochromatic X-ray source operates under UHV conditions and is separated from the elevated pressures of the sample chamber using a silicon nitride window (Norcada). The results within this dissertation have been produced using windows with thicknesses of 1.0, 0.5, and 0.2 μm , all of which allow for a pressure differential > 1 atm to UHV. Operating the anode at 10 kV/20 mA gives an X-ray flux to the sample of $\sim 10^9$ photons $\text{s}^{-1} \text{mm}^{-2}$ for a 1.0 μm thick window. Higher X-ray fluxes can be achieved through the use of thinner X-ray windows; it should be noted that the transmittance through 1.0, 0.5, and 0.2 μm of silicon nitride for photons of 1486.6 eV is approximately 76.7 %, 87.5 %, and 97.4 %, respectively. Care must be taken to minimize pressure bursts on either side of the window during venting and pumping of the instrument as breakage can occur from sharp deltas in pressure.

The exchangeable analysis chamber design allows for the flexibility of designing custom chambers that can be dedicated to specific AP-XPS projects. This principle was first introduced in synchrotron-based AP-XPS instruments [10,12] and has been adapted herein to work for a laboratory-based setup. The interchangeability of the analysis chambers allows for the customization of vacuum components that are potentially required for certain experiments, and the dedication of chambers to exposures to gases used in experimental exposures, preventing cross contamination. A custom-built sample holder (Heat Wave Labs) allows for sample temperatures ranging from -20 to $1,200$ °C using a ceramic button heater that is actively cooled with a lab

chiller and an ethylene glycol/water mixture. Sample cleaning is performed in the analysis chamber via Ar⁺ sputtering (IG2, RBD Instruments). Exchanging samples requires breaking vacuum and removing the sample holder from the analysis chamber.

2.3.3 Hydrogen Plasma Process and Monitoring

Plasma cleaning to the analysis chamber was performed with an attachable vacuum compatible RF plasma generator (PIE Scientific LLC, SEMI-KLEEN plasma cleaner). Treatment typically occurred after the chamber was baked; the baking temperature could only not exceed 110 °C due to Viton gaskets present in the differential pumping sections of the AP-XPS instrument. The hydrogen gas (Praxair, 99.999%) was connected to the generator through Swagelok tubing and the pressure in the RF chamber of the generator was controlled with a built-in mass flow controller. After the plasma was created in the RF chamber it proceeded to the analysis chamber through a one-centimeter aperture. The effects of the plasma treatment were monitored from the base pressure of the analysis chamber and with a mass spectrometer (MKS, e-Vision) also mounted on the analysis chamber.

2.4 Results and Discussion

2.4.1 System Performance in Vacuum and Under the Presence of Nitrogen Gas; Pressure Response and Signal Acquisition

This section provides data related to commissioning experiments that are critical in characterizing the performance of the AP-XPS and critical parameters that are used in every subsequent experiment performed on the instrument. In order to determine the optimized position of the sample relative to the aperture, experiments were conducted assessing the XPS intensity versus the sample-to-aperture distance

defined in **Figure 2.2**. The initial position of the Ag foil was in contact with the aperture which was monitored using a camera mounted on the analysis chamber. Throughout the experiment the distance between the sample and aperture (d) was increased by retracting the sample along the x-axis of the manipulator which moves along the spectrometer axis. Because of the 20° tilt, counts are observed while the sample was in contact with the aperture at $d = 0$. As the sample is retracted from the aperture the intensity initially increases, followed by a decrease as the sample moves away from the focal position of the X-ray spot and analyzer electrostatics. The data points associated with the signal relative to position along the x-axis were fit to a second order polynomial with $R^2 > 0.992$ for all fits. The derivative gives maxima located at 0.57, 0.57 and 0.56 mm for angular, transmission and acceleration modes, respectively. These results show that all three electrostatic lens modes have similar optimized positions for the sample-to-aperture distance.

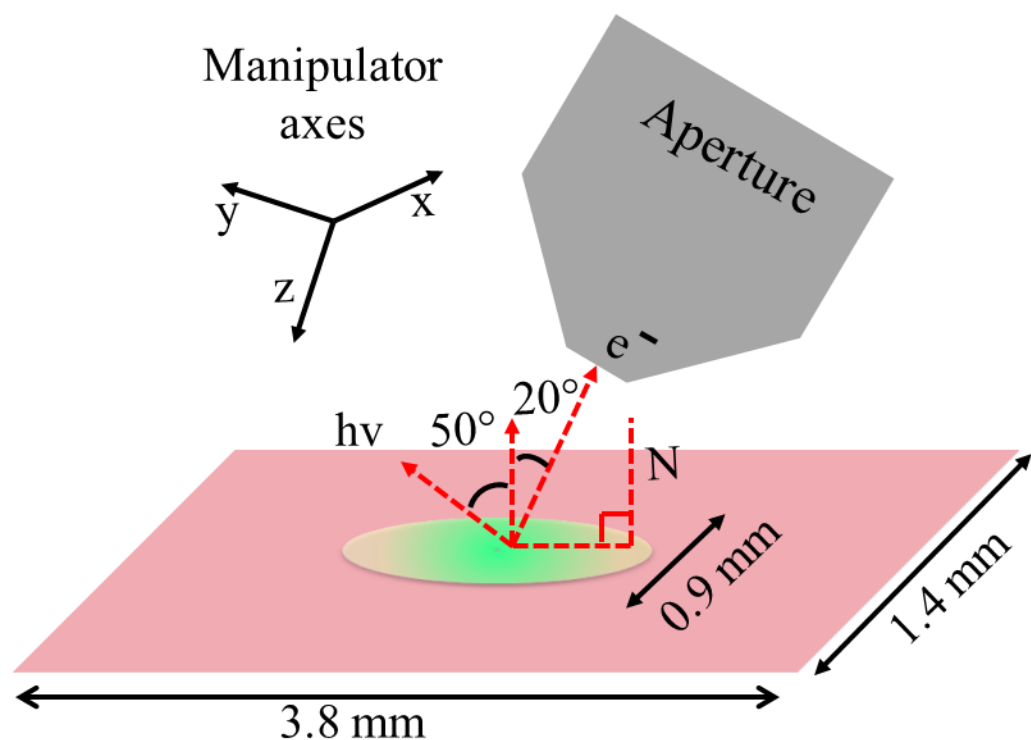


Figure 2.2: Sample analysis geometry indicating the X-ray illumination spot (red) and XPS analysis collection area (green). The z-axis is the energy axis of the analyzer and N is the sample normal with the X-rays at 55° and analyzer at 20° . Sample to aperture distance denoted by the dashed arrow pointing from the X-ray spot to the aperture cone terminated with e^- .

If the sample is too close to the aperture during an APXPS experiment the effective pressure above the sample will be smaller than that of the background pressure. This would give rise to misleading results as pressure gauges on the analysis chamber measure the background gases and are the values which get reported in publications. The gas phase pressure between the sample and aperture is 95 % that of the background pressure when the sample-to-aperture distance is equivalent to the

aperture diameter. The optimized counts occur at an ideal sample-to-aperture distance just beyond the length of the aperture diameter of 0.5 mm. Thus, at the beginning of a typical ambient pressure XPS experiment the sample is first optimized under vacuum by monitoring the counts while approaching the sample towards the aperture. When the counts have been optimized, the sample is at the ideal sample-to-aperture distance for experiments to be performed under pressure.

The X-ray spot size for the MX650 has been determined previously to be about 1.4 x 3.8 mm at 12 % and 88 % signal intensity cutoffs for a 54.7° X-ray spot projection [74]. The electron capture spot size on the sample (**Figure 2.2**) is expected to be smaller than the X-ray spot size due to the narrow angle of acceptance into the aperture. In order to assess the electron capture spot size, experiments were performed by manipulating the Ag foil along the z-axis (**Figure 2.3**) at $d = 0.5$ mm; moving along the z-axis keeps the sample-to-aperture distance constant. At the beginning of the experiment, the aperture was placed over the Ag foil at a specific z-axis manipulator position where maximum counts were obtained. The sample was then moved and XPS spectra were collected as a function of z-axis position. **Figure 2.3a** shows example Ag 3d(5/2) spectra at four different relative z-axis positions. As the electron capture spot drives off the edge of the Ag foil sample the Ag 3d(5/2) intensity decreases. **Figure 2.3b** shows results of the Ag 3d(5/2) peak areas from experiments using the angular (red), transmission (green), and acceleration mode (blue). The XPS peak areas are normalized relative to the most intense peaks during the initial manipulation. All three modes give similar results with a drop in the signal intensity starting at a relative z-axis position of 0.45 mm and zero intensity at 1.65 mm. Thus, all three modes yield a similar spot size for electron capture. The electron spot size

was determined using 12 % and 88 % signal intensity cutoffs, similar to the X-ray spot size determination,[74] and are shown as solid black lines in Figure 6b. From this we estimate the spot size to be 0.9 ± 0.1 mm, where the error is due to variation in intensity between each mode at the 12 % and 88 % cutoffs. The electron capture spot size normal to the z-axis along the sample surface was not determined. However, it is expected to be slightly elongated due to the 20° offset of the spectrometer relative to the sample normal (green spot, **Figure 2.2**).

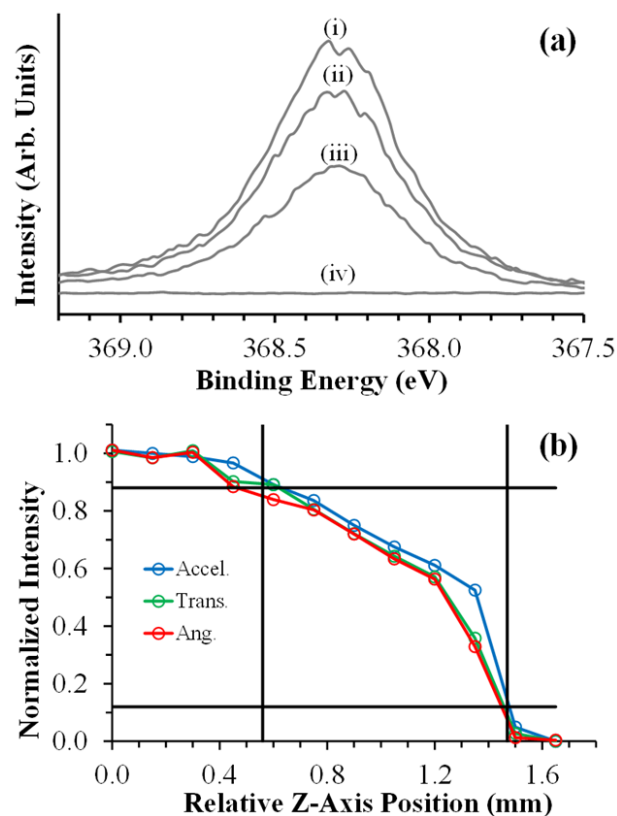


Figure 2.3: Determination of AP-XPS analysis collection area (spot size of the analyzer field of view) on a silver foil. (a) Ag 3d (5/2) spectra at relative z-axis positions moving away from the center of the foil (i) 0, (ii) 0.75, (iii) 1.35, and (iv) 1.65 mm. (b) Normalized Ag 3d (5/2) spectra area as a function of z-axis position for acceleration (blue), transmission, (green) and angular (red) modes. Black lines represent 12 % and 88 % cutoffs for area and z-axis position. Reproduced with permission from [70].

Assessment of instrument response to increasing chamber pressure is a critical parameter in determining the efficiency of the spectrometer at collecting photoelectrons through a gas phase. The rate of attenuation can be used to calculate the effective path length of which a photoelectron travels through the gas phase. The

results of normalized XPS Ag 3d(5/2) area versus analysis chamber N₂(g) pressure for angular (red), transmission (green), and acceleration (blue) modes are shown in **Figure 2.4**. Spectra were collected using the 0.8 mm curved slit, 200 eV pass energy and a 3-minute acquisition time up to 15 Torr for acceleration mode and 10 Torr for transmission and angular modes. XPS intensities (I) in **Figure 2.4** were normalized by dividing by the maximum signal under vacuum conditions (I_0) for each mode. From UHV up to 0.1 Torr attenuation is minimal. At pressures near 1 Torr the signal begins to significantly attenuate. **Figure 2.4b** shows example spectra for acceleration mode from 10⁻² to 15 Torr. A separate spectrum (**Figure 2.4b (vi)**) was collected at 20 Torr for 4.5 hours.

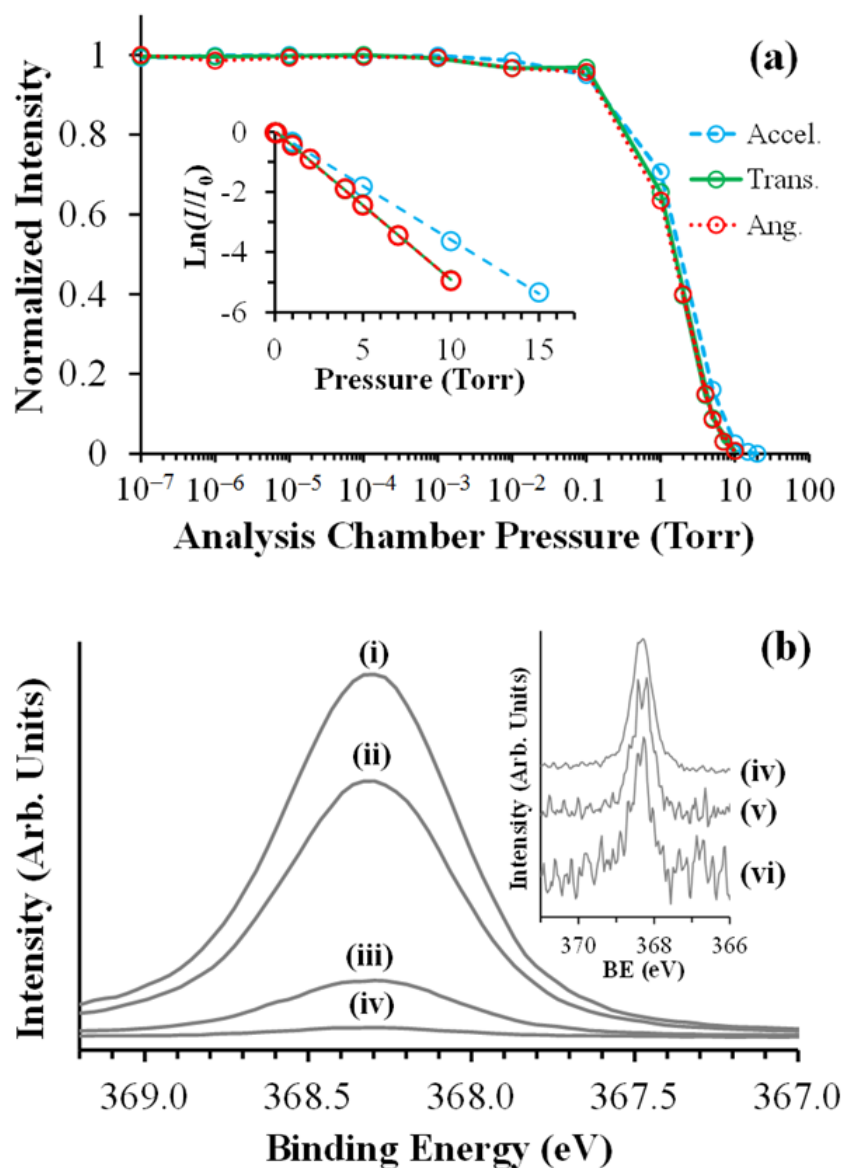


Figure 2.4: Ag 3d (5/2) signal intensity attenuation using nitrogen gas. (a) Relative Ag 3d (5/2) intensity as a function of analysis chamber pressure for acceleration (blue), transmission (green), and angular (red) modes. Inset displays exponential plot according to Equation 2.1. (b) Ag 3d (5/2) spectra collected in acceleration mode at (i) 10^{-4} , (ii) 1, (iii) 5, (iv) 10, (v) 15 and (vi) 20 Torr. Inset spectra (iv) to (vi) were normalized to give similar intensities. Reproduced with permission from [70].

XPS signal attenuation decreases exponentially as a function of pressure according to Equation 2.1 [75]

$$\ln \frac{I}{I_0} = -\frac{\sigma_e d_{\text{eff}} c}{kT} p \quad (\text{Eqn. 2.1})$$

where p is pressure in Torr, $T = 298$ K, $k = 1.38 \times 10^{-23} \text{ m}^2 \text{ kg s}^{-2} \text{ K}^{-1}$ is the Boltzmann constant, $\sigma_e = 1.9 \times 10^{-20} \text{ m}^2$ for $\text{N}_2(\text{g})$ is the total electron scattering cross section at 1120 eV kinetic energy [76], $c = 133.322$ is the conversion from Pascal to Torr, and d_{eff} is the effective path length. The effective path length is the distance the photoelectrons were to travel to the analyzer if the pressure were to be constant during its travel. The inset of **Figure 2.4a** shows linear fits using Equation 2.1. Values of d_{eff} were calculated from the slopes for acceleration, transmission and angular modes to be 0.59, 0.81 and 0.80 mm, respectively. The calculation of d_{eff} for acceleration mode was comparable to the optimum distance of 0.56 mm determined from signal maximization. However, d_{eff} for transmission and angular modes are ~ 0.2 mm greater than for acceleration lens mode. This increase in d_{eff} for transmission and angular modes, relative to acceleration, is due to the two modes operating with the first electron focusing lens (immediately behind the aperture) electrically grounded while acceleration mode applies +4000 V to this first focusing lens. The application of this high voltage immediately behind the aperture in acceleration mode increases the velocity of the photoelectrons within the higher-pressure region of the instrument sooner than transmission and angular modes, which not only improves counts significantly with little loss in resolution, but also gives d_{eff} values closer to true sample to aperture distance. Transmission and angular modes apply the electrostatic

lens bias starting at the second aperture, which is located a few millimeters behind the first aperture yielding higher d_{eff} values.

2.4.2 Chamber Pressure Response to Hydrogen Plasma

The ability of the differential pumping stages and gauges positioned on the chamber, monochromator, and third pumping stage were used to assess the pressure conditions of the system as a function of increasing analysis chamber pressure. As the analysis chamber is increased up to 1 Torr pressure, there is little increase in the Stage 3 pressure (**Figure 2.5**; left y-axis). When the pressure was increased past 1 Torr in the analysis chamber Stage 3 pressure increases, remaining at 8×10^{-7} Torr with the analysis chamber at 20 Torr. This pressure gauge is also used as an automated override to shut off the analyzer if the pressure within the third stage is $> 10^{-6}$ Torr. Beyond this pressure in the third stage the safe operation of the analyzer not adequately safeguarded. Since the analyzer (Stage 4) also has a dedicated turbo pump it will remain significantly lower than the 10^{-6} Torr Stage 3 trigger and can operate safely at 20 Torr in the analysis chamber. The load on the first stage can also be assessed by the power that the turbos in Stage 1 consume, the rise in power consumption is aligned with the increase in pressure in the analysis chamber (**Figure 2.5**; right y-axis) As the turbos in Stage 1 are the closest to the analysis chamber, they bear the most load of gas pumping by the system and were the only pumps to increase their power consumption.

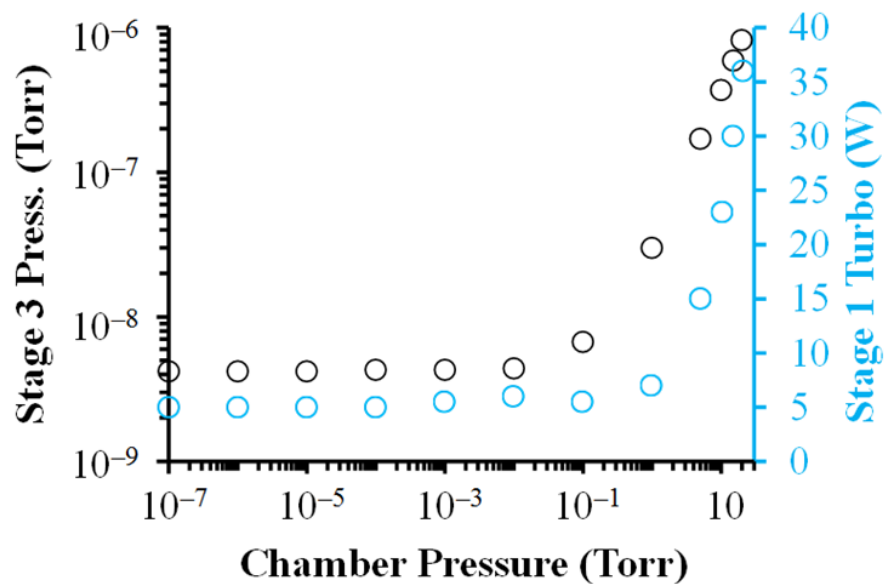


Figure 2.5: Stage 3 pressure (black) and Stage 1 turbo pump power (blue) versus analysis chamber pressure as N₂ gas was introduced. Reproduced with permission from [70].

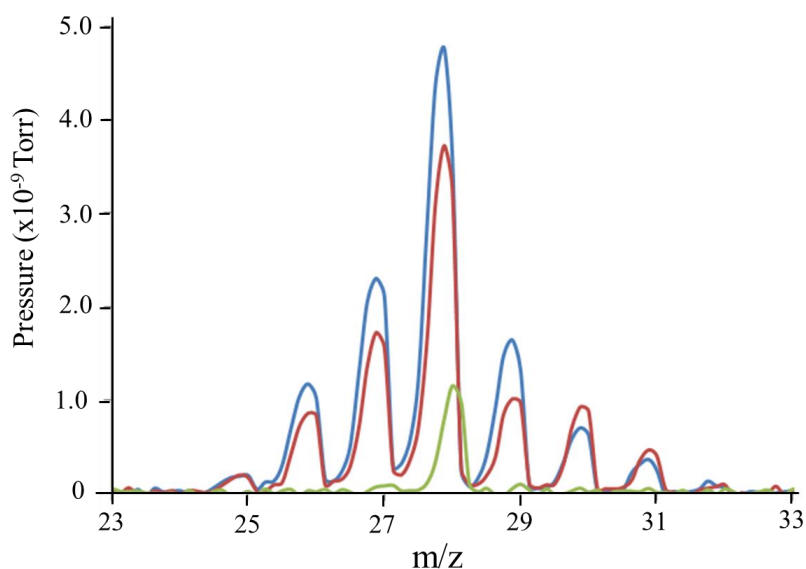


Figure 2.6: Mass spectrometer response of the analysis chamber at 110 °C (blue), after 40 minutes of H₂ plasma (0.001 Torr) at 110 °C, after vacuum evacuation at 21 °C (green).

The baseline pressure of the analysis chamber during most experiments was between 10^{-7} and 10^{-8} Torr. This was primarily water adsorbed to the chamber wall remaining present in the system after the chamber was pumped down, which was confirmed by mass spectrometry. Given that the vacuum of the analysis chamber must be broken to insert a sample, it was not possible to remove sources of water from entering the chamber. The base pressure of the system could be improved by baking the chamber, however given limitations in materials within the analysis chamber the system could not be heated above 110 °C. The high temperature is used to increase the desorption rate of vacuum contaminants from the walls, allowing them to be pumped away at greater efficiency, including water and adventitious carbon molecules. During the bake and plasma treatment, a mass spectrometer attached to the analysis chamber was used to monitor the species present in the vacuum (**Figure 2.6**). The baking procedure, given enough time, was useful in removing water molecules but it was less sufficient at removing all carbonaceous species. The presence of water and carbonaceous species can be detrimental to the analysis of samples as their adsorption and react and cause changes to surface chemistry. The use of a hydrogen plasma, which creates highly reactive hydrogen radicals, was applied to further remove vacuum contaminants. The plasma greatly reduced the amount carbon species observed by mass spectrometry. The baking and plasma treatments were able to reduce the base pressure of the instrument to 10^{-9} and 10^{-10} Torr. Mass spectrometer showed that the species at 28 m/z was the predominate remaining species and can be ascribed to CO, which is known to be present in ultra-high vacuums. However again because the chamber vacuum must be broken for samples to be introduced these

pressures are short lived and the treatments would thus also affect the samples present in the chamber.

2.4.3 Factors Influencing Signal Acquisition in Ambient Pressure X-ray Photoelectron Spectroscopy (AP-XPS)

2.4.3.1 X-ray Windows and Spot Size

The section focuses on parameters and determining factors that greatly influence the electron collection efficiency of AP-XPS systems, particularly those which are lab-based instruments. The X-ray anode materials commonly used in lab-based AP-XPS to date include Al and Mg, which produce K_{α} lines at 1486.6 eV and 1253.7 eV, respectively. The high voltage anode to produce X-rays operates in keV range and must be isolated from the high gas pressures in the analysis chamber. The ability to maintain UHV in the X-ray source is essential for the operation and sustainability of the anode. Modern lab-based AP-XPS systems use an X-ray window (**Figure 2.7a**) with high transparency to separate the UHV pressures in the X-ray source to Torr level pressures in the analysis chamber.

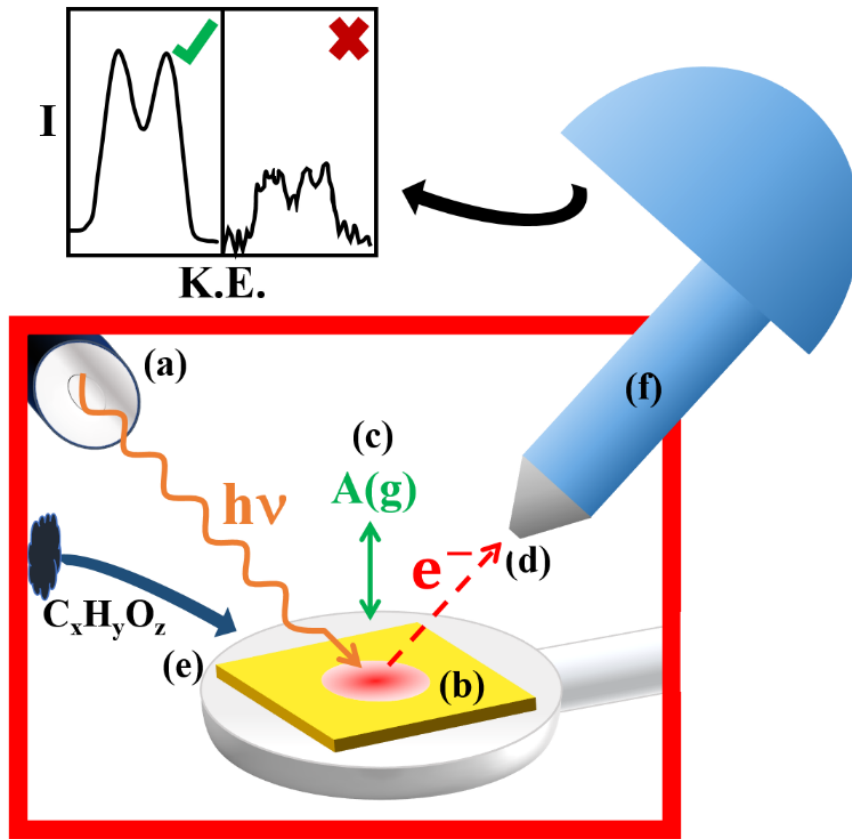


Figure 2.7: Metrics impacting lab-based AP-XPS signal and experimental quality. (a) X-ray transparent window, (b) X-ray spot size and flux onto sample, (c) gas phase pressure, (d) aperture diameter, (e) sample charging and contamination, (f) electrostatic lens system and pumping capacity. Reproduced with permission from [58].

With the use of monochromatic X-ray sources, the X-ray beam converges as it travels from the focusing crystals towards the sample surface. Thus, as the light transverses the X-ray window, it is often a few mm in diameter depending on the distance of the X-ray window from the sample surface. In order to mitigate the loss of XPS signal, the window should have as little impact on the X-rays as possible. Hence, it is essential that the X-ray window be as transparent to ~ 1 keV X-rays and as thin as

possible to reduce the light attenuation. From an instrumental sustainability perspective, it is also essential that the window material be very rigid with the ability to withstand a large pressure differential from UHV to 760 Torr. The two most commonly used X-ray window materials are Al and Si₃N₄.

It is also worth noting that a balance must be maintained between the size of the X-ray window and the distance between the X-ray window and the sample. The X-rays must travel through the sample chamber at elevated pressures. Thus, the closer the window is to the sample the less attenuation of the X-rays, and therefore less loss of XPS signal. However, if the window is too close there is also a risk of subjecting the window to high temperatures for those systems with the ability to heat samples. Finally, the X-ray window must also provide a high-quality vacuum seal between the X-ray source and analysis chamber. As the pressure in the analysis chamber increases up to the 10's of Torr range for modern systems, there should be no measurable pressure change above UHV within the X-ray source. For example, it has been shown that the high-pressure limit of a lab-based AP-XPS system can be determined by the quality of the X-ray window seal. Mangolini et al. [77] raised the pressure of their analysis chamber up to 0.4 Torr before reaching a maximum operating pressure within the monochromator because of an aluminum X-ray window.

The X-ray spot size for modern lab-based AP-XPS systems ranges from ~3 mm [70,78] to 0.3 mm [79,80] (depicted in **Figure 2.7b**). For a given power output from an X-ray source, the smaller the spot size the higher the X-ray flux to the sample. The ideal X-ray spot size should be similar to (or slightly smaller than) the diameter of the aperture above the sample surface. Typical aperture diameters can range from ~0.3 to 1.0 mm. For those X-ray spots that are larger than the aperture, there will be a

significant portion of the sample that is illuminated by X-rays for which the ejected photoelectrons will not make it through the aperture for future detection by the analyzer. Thus, an X-ray spot that is similar in size to the aperture will lead to a more efficient XPS signal.

2.4.3.2 Gas Pressure and Aperture Size

The path of emitted photoelectrons through the gas phase above the sample is a large contributor to signal loss, depicted in **Figure 2.7c**. Emitted photoelectrons can undergo either elastic or inelastic scattering upon collision with gas phase atoms or molecules. The elastically scattered electrons experience collisions which preserve their kinetic energy but may have their trajectory altered out of the spectrometer's field of view. Inelastic scattering results from a loss of kinetic energy in the form of an excitation to a new state or ionization of the gas molecule. Signal is adversely affected by the scattered electrons which decreases peak intensity while increasing the background noise. The XPS signal intensity at a given pressure (I) relative to the intensity under vacuum (I_0) follows Beers Law according to Equation 2.1:

$$I = I_0 e^{-\frac{p\sigma d_{eff}}{kT}} \quad (2.1)$$

where p is pressure, k is the Boltzmann constant, σ is the total electron scattering cross section at a certain kinetic energy and d_{eff} is the effective path length the photoelectron travels through the gas phase. Given this exponential relationship, when the length d_{eff} is close to the inelastic mean free path of electrons, there is a strong impact of pressure on the overall XPS signal. To mitigate the effects of high pressures, the sample-to-aperture distance should be minimized. However, the sample-to-aperture distance allowed in experiments is strongly a function of the aperture size (**Figure 2.7d**) and

the need to keep the pressure directly over the sample very close to the measured background chamber pressure.

If the aperture is brought too close to the sample surface, the gas phase pressure above the sample will drop below the background chamber pressure. As a general rule, the sample should remain one aperture diameter distance away. Under these conditions the pressure above the sample is >95 % of the background chamber pressure when the gas is in the viscous flow regime [81]. With the criteria of keeping the sample one aperture diameter away, it becomes apparent that the smaller the diameter of the aperture, the closer the sample can be to the aperture entrance plane. Thus, the use of smaller apertures allows for the electrons to travel through a small region of elevated pressure, and therefore dramatically increases (given exponential relation of Eqn. 2.1) the overall XPS signal for a given pressure.

However, a smaller aperture may also lead to a less efficient capture of the emitted photoelectrons if the aperture size becomes smaller than the X-ray spot (as discussed in the previous section). Under low pressures, even UHV conditions, the smaller the size of aperture the lower the collection area of emitted photoelectrons on the sample surface. For a given experiment, the aperture size remains fixed and a balance must be struck between electron attenuation by the gas phase and less efficient collection of the electrons by a reduced aperture diameter. In practice, experiments reveal that the relationship between analysis chamber pressure and aperture size creates a dynamic, in which the higher pressures require a smaller aperture and lower pressures require larger diameters [74].

It should also be noted that the value of d_{eff} in Equation. 2.1 is not strictly the sample-to-aperture distance given the pressure drop behind the aperture is not

immediate. Rather, d_{eff} is an effective path length of the scattering cross section that the electron experiences on its way to the detector. More specifically, d_{eff} should be measured experimentally for a given lab-based AP-XPS system using a gas like N₂ which has well-known σ values as a function of kinetic energy [75]. This will allow for the direct measurement of d_{eff} via Equation 2.1. It has been shown that the value of d_{eff} varies for different electrostatic lens modes which vary the electron trajectories as they travel from the sample to the electron energy analyzer [70]. Thus, the value of d_{eff} is not simply determined by the distance it travels through an elevated pressure regime but is also a function of the electron trajectory near the aperture entrance.

2.4.3.3 Sample Contamination and Charging

Another consideration that must be accounted for is the potential contamination of the sample (represented in **Figure 2.7e**). The presence of adventitious carbon or other adsorbate contaminants can dampen photoelectron signal from the underlying substrate and can block possible active sites that are of interest in adsorption studies. In conventional XPS systems where UHV pressures are achievable, samples can sit in vacuum for hours with minimal contamination. Moreover, dosing samples in the Langmuir regime using UHV systems allows for very precise control of gas exposures. The ability to mitigate adventitious adsorbates has been one of the prevailing advantages of UHV XPS.

The goal of lab-based AP-XPS measurements is to intentionally expose samples to various gases at elevated pressures. Unfortunately, the increased pressure in the analysis chamber causes the ambient background pressure of the chamber to be elevated after being evacuated, which can be a concern for freshly introduced samples. Moreover, gases introduced into the analysis chamber can displace species already

adsorbed on the chamber walls, which can in turn adsorb onto the sample surface. These processes are worsened by lower pumping speeds in the experimental chamber during high pressure measurements, where the vacuum pumps are closed off and the aperture above the sample is the only source of flow out of the chamber. For these reasons, the use of a small volume analysis chamber offers an advantage over a large volume chamber, i.e. less chamber wall surface area and faster turnover rates. Proper baking and vacuum maintenance is essential to prevent contamination from residual gases utilized in prior experiments. The cleanliness of the gas being introduced is also critically dependent upon the purity of the gas and the meticulous cleanliness of the *ex-vacuo* lines which the gas molecules travel down to the analysis chamber. Extreme care should be taken to not cross contaminate these lines by using isolated plumbing for different (non-inert) gases.

Insulating samples are often problematic in XPS due to sample charging issues. The emission of photoelectrons causes a buildup of positive charge on the surface of poorly conducting samples. This positive charge in turn interacts with ejected photoelectrons which can lead to significant shifts and broadening in XPS spectra. These effects can make it difficult to assess the chemical oxidation state of a given photoemission peak. Traditionally, UHV XPS systems have been equipped with an electron flood gun to circumvent charging artifacts in insulating samples by utilizing low energy electrons to discharge the sample surface. However, as with X-ray sources, a standard flood gun uses hot filaments which also require vacuum conditions (typically $< 10^{-4}$ Torr) to operate and thus is not conducive for use in AP-XPS systems.

The gases present during lab-based AP-XPS experiments can contribute to the alleviation of sample charging of insulating surfaces. The X-ray ionization of the gas phase species above the sample surface leads to the emission of photo, Auger, and secondary electrons which aid in partial or complete charge dissipation at the surface. However, for wide band gap materials, this mechanism of charge decapitation is often insufficient. It is also possible to induce partial charge dissipation by moderately heating the sample during XPS measurements, reducing the resistance of the system. But sample heating is not always an appropriate option due to thermal instability (decomposition), to changes in reactivity, and to the removing of experimental conditions from its desired range.

2.4.3.4 Electrostatic Lens and System Pumping

The electrostatic lens system serves to significantly increase the efficiency of photoelectron collection as they leave the sample surface (**Figure 1.4**). The closer the first region of the electrostatic lens is to the sample surface, the more the collection efficiency will be enhanced. This is often referred to as the pre-lens region, the area between the first and second differential pumping apertures. The entire electrostatic lens array is composed of numerous lenses with separately applied voltages (**Figure 2.7b**). The electrostatic lenses augment the KE of the photoelectrons to that of the pass energy of the analyzer to allow detection as a function of KE. For a given AP-XPS system, different lens modes can significantly impact the XPS intensity and resolution and can be fine-tuned to increase the capabilities of the instrument, i.e. spatial or angular resolution [70,73].

One of the major differences which cannot be avoided between a conventional XPS analyzer and one with a differentially pumped electrostatic lens is the number of

turbo pumps required. For a modern differentially pumped system, the largest load on the pumps will be on the first pumping stage (**Figure 2.1**, green). Less efficient pumping on the first stage will significantly impact the pressures immediately behind the first aperture, and therefore significantly impact the XPS intensity. The electron energy analyzer requires high vacuum conditions to the high voltages that are used. For this purpose, additional pumps are placed between first stage and the analyzer to reduce the pressure at the analyzer when the analysis chamber is under Torr level pressures. The more pumps on the differentially pumped electrostatic lens, the lower the base pressure at the analyzer entrance slits, which will increase the longevity of the electron detector. This is particularly important if the gases being used are reactive.

2.4.3.5 Other Considerations

Lab-based AP-XPS is a power tool because of its ability to probe changes in the surface chemistry of a given substrate as a function of the surrounding gas phase. However, irradiation by X-rays under *in-situ* conditions can potentially cause chemical changes in materials, with some materials being more susceptible than others, such as halide molecules and organic compounds. This is often referred to as X-ray induced damage. Reducing the overall X-ray exposure to the sample during lab-based AP-XPS experiments can help mitigate this situation. For example, coupling the spectral acquisition software to the X-ray high voltage power supply will allow for an automated shut off the X-rays at the end of a spectrum collection [70]. Another remedial measure for single crystal samples is to reduce the X-ray exposure by moving the X-rays from one spot to another along the sample surface as the experiment progresses. This method would benefit from those lab-based AP-XPS systems that have a smaller X-ray spot size.

There are several considerations that need to be made regarding sample holders employed in lab-based AP-XPS systems. Compared to UHV sample holders, those that operate under elevated pressures need special consideration. For a typical resistance heater, the temperature difference between the heat source and sample surface is exacerbated by increased gas pressures which often enter the analysis chamber at room temperature. Given the high concentration of gas molecules compared to traditional UHV setups, more scrutiny must be placed on the materials used for the sample holder, as there is an increased threat of reacting with gases at elevated temperatures. A solution to this comes via the use of an IR-laser sample heater, which would heat the sample directly [80]. There are also additional considerations to be made when cooling a sample in the presence of condensable gases like H₂O. While conventional UHV cooling systems allow for the flowing of liquid nitrogen, in a lab-based AP-XPS system, use of liquid nitrogen would lead to the condensation of H₂O onto the liquid nitrogen lines in the analysis chamber. For lab-based AP-XPS experiments in the presence of condensable gases at cold temperatures, the sample itself must be the coldest object in the analysis chamber. This can be accomplished, for example, using a vacuum compatible Peltier holder [42]. However, the Peltier device has limited thermal stability which precludes the incorporation of high temperature heating capabilities in tandem.

Modern AP-XPS systems have the electrostatic lens analyzer aligned either vertically [77,82] or horizontally relative to the lab floor [74,83]. These differences in alignment of the analyzer impact sample handling. For those systems with a vertical lens, the sample can be placed under the first aperture in a horizontal position, while those with a horizontal lens have the sample aligned vertically relative to the lab floor.

Requiring the samples to be aligned vertically may impact the ability to analyze the liquid-gas interface of bulk liquids that are thick droplets and would thus be pulled down the sample holder due to gravity.

2.5 Conclusions

This chapter was dedicated to the description of a lab-based ambient pressure X-ray photoelectron spectroscopy (APXPS) setup using a VG Scienta monochromatic Al K_{α} X-ray source and ambient pressure electron energy analyzer. The design of the instrument accommodated the ability to swap out small volume sample analysis chambers, and have samples sitting horizontally relative to the lab floor. The ability to swap small volume analysis chambers allows for versatility in designing future custom chambers for different experiment. Horizontal sample configuration allows for the study of both solids and liquid droplets in the presence of a gas phase. The instrument provides a unique opportunity to probe heterogeneous chemistry at the solid/gas and liquid/gas interfaces with elemental and chemical sensitivity. The ability to probe a static liquid droplet *in-situ* is investigated in Chapter 3. Chapter 4 and 5 examine solid/gas interfaces.

Commissioning experiments were performed using the Ag 3d(5/2) signal of a silver foil and an aperture diameter of 0.5 mm to assess the operation of three different electrostatic lens modes: acceleration, transmission, and angular. All three modes gave similar optimum XPS signals under vacuum at sample-to-aperture distances ranging from 0.56 to 0.57 mm. Likewise, all three modes gave a similar XPS analysis spot size of 0.9 ± 0.1 mm at a sample distance of 0.5 mm from the aperture using 12 and 88 % intensity cutoffs. APXPS Ag 3d(5/2) signal attenuation is first order with respect to N_2 gas pressure above 0.1 Torr up to a maximum of 20 Torr. Beyond 20 Torr the

collection statistics are not feasible to conduct an adequate experiment. From 10^{-7} to 10^{-1} Torr, signal attenuation is minimal. The use of acceleration lens mode resulted in an approximately 10-fold increase at vacuum and higher pressures, with actual magnitude of increase dependent on the pressure in the analysis chamber. Most of the gas load pumping was shown to occur in first pumping stage immediately behind the analysis chamber aperture. The X-ray window showed no evidence of leaking as seen by the monochromator UHV pressure remaining constant up to 20 Torr in the sample analysis chamber.

Chapter 3

SURFACE SPECTROSCOPY OF ZINC BROMIDE INTERFACIAL CHEMISTRY DURING DELIQUESCENCE

3.1 Abstract

Aqueous ionic interfaces are universally abundant and play a critical role in many physical, chemical, biological, environmental, and technological processes. Ions at liquid interfaces can experience an asymmetric environment that influences their interfacial composition, orientation, dielectric forces, and transport properties. Therefore, structure and chemistry of liquid/vapor interface is a topic of fundamental significance. Probing the electronic structure and interfacial concentration of aqueous electrolytes at a molecular level is technologically challenging. Within this section results are presented from ambient-pressure X-ray photoelectron spectroscopy (AP-XPS) experiments of zinc bromide, a salt utilized as an energy storage medium within zinc-bromine flow batteries, and in heterogeneous catalysis. The efficiencies of these processes can be directly impacted by the abundance of water in the local environment surrounding the salt.

AP-XPS was employed to study the solid-vapor and aqueous-vapor interfaces of zinc bromide film under ambient water vapor conditions from $<1 \times 10^{-7}\%$ to 17% relative humidity (RH). Deliquescence of zinc bromide occurs within this RH range, allowing for surface chemical measurements of ZnBr_2 to be taken as it transitions from a solid to a liquid. Zinc, bromine, and oxygen core shell spectral analysis showed clear changes in widths, shifts, and interfacial concentrations due to the phase change of

zinc bromide from a solid salt to an aqueous solution with increasing RH. The ability of a lab-based AP-XPS to investigate the interfacial concentrations of liquid solutions has previously only been observed with photoelectron spectroscopy using variable photon energy provided at synchrotron light sources. These results highlight the powerful of utility lab-based AP-XPS to interrogate changes in the electronic structure and chemical composition of salts at solid-vapor and liquid-vapor interfaces.

3.2 Introduction

The adsorption of water onto salt surfaces at heterogeneous interfaces is ubiquitous and plays important roles in industrial and natural systems. The interactions of salt ions with water at the solid-vapor and liquid-vapor interfaces have been shown to affect surface properties, such as chemical potential and ion distribution [84-87]. In this chapter, particular aspects of the liquid/vapor interface are of interest, i.e. the behavior of ions at the liquid water surface. The classical text-book description of surface ion propensity predicts a complete depletion of ions at the saline surface [88,89] however, the nature of interfacial ion segregation has become more widely accepted in the recent years as theoretical and experimental evidence mounts. Studies have investigated the nature of ion interfacial concentration at the saline solution/vapor interface and showed evidence of large polarizable halide anions having higher concentrations at the interface than the bulk [90]. This phenomenon has been studied with numerous surface sensitive techniques including X-ray photoemission, [91,92] vibrational sum frequency generation, [93,94] and aerosol uptake experiments [95,96]. Molecular dynamic simulations of saline solutions have been supported experimental observations of unsymmetrical ion densities [97,98]. These studies have purposed that the segregation of ions to the surface causes small

hard ions, such as alkali cations, to be repelled from the aqueous surface while the large polarizable anions can be enhanced in concentration at the surface, however most if not all studies investigating this ion segregation have been limited to alkali halide salts.

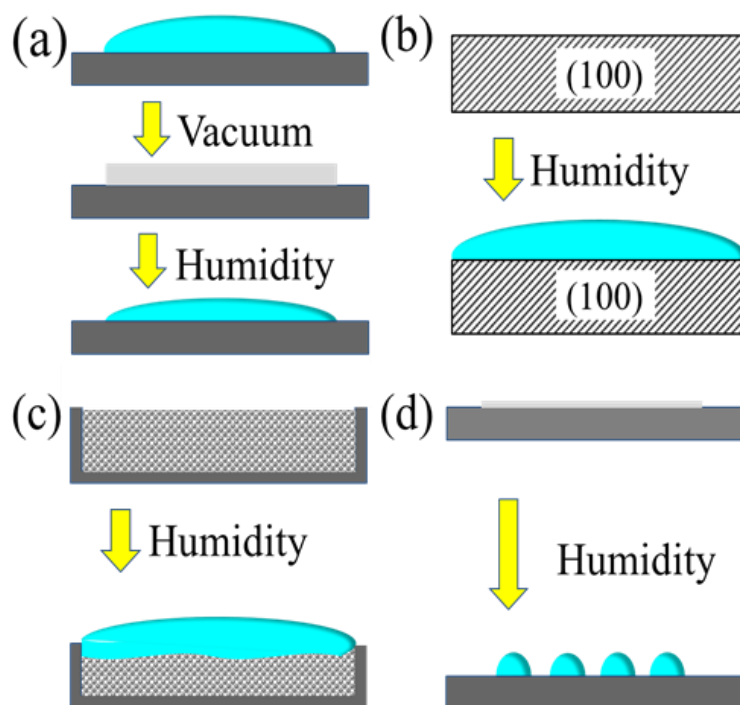


Figure 3.1: Representations of substrate configurations used in water adsorption experiments with AP-XPS (a) Concentrated salt solution deposited on substrate, evaporated under vacuum, and then exposed to humidity above deliquescence. (b) Salt single crystal exposed to humidity above deliquescence in vacuum to form continuous solution film. (c) Salt powder pressed pellet deliquesced in vacuum to form continuous solution film. (d) Thin film of salt exposed to humidity above deliquescence creating discontinuous droplets of salt solution.

Among the first experiments performed with AP-XPS after the initial development of differential pumping was made to the instrumentation to limit the electrons scattering through the gas phase was the study of the liquid-vapor interface [8,9]. Over the past few decades several advancements to the instrumentation have allowed ambient-pressure X-ray photoelectron spectroscopy (AP-XPS) to probe interfacial surfaces at higher pressures. These advancements include the development of a differentially pumped electrostatic lens, X-ray transparent windows, and collection apertures, enabling photoelectron measurements to “bridge the pressure gap” and study interfacial systems at near ambient pressures [1,10-12]. Synchrotron-based AP-XPS instruments have been used to study the interaction of water vapor with salts, including NaCl,[99-105] NaBr,[102] Br doped NaCl,[106] NaI,[102,103] NaClO₄,[105] KBr,[92,107] KI,[90,108,109] KBrO₃,[107] KIO₃,[108] RbCl,[99] and RbBr [99]. Additional studies have examined the aqueous-gas interface of liquids by combining AP-XPS with a liquid microjet (LMJ) to probe a salt solution stream whose composition, i.e. concentration and acidity, can be more readily adjusted upstream (outside of the vacuum chamber) than samples generated from solid salts [110-129]. **Figure 3.1** illustrates various experimental approaches for salt deliquescence studies. One approach is to deposit a salt solution onto an inert substrate, which is then evaporated forming a continuous solid film on which the experiment is conducted [101-105] The most common approach is the use of single crystals or thick films formed from salt evaporation onto an inert substrate, which is subsequently exposed to increasing humidity *in-vacuo* to probe deliquescence events[90,99,100,106,108,109]. Another approach is to press crystalline salt powders into a solid pellet, which

converts the most common form of commercial salts into a vacuum compatible substrate [107].

The majority of the AP-XPS studies have been conducted with the samples above the deliquescence relative humidity (DRH) of the salt, probing only the liquid-gas interface. Several studies have examined the salt interface while transitioning from a solid to a liquid, i.e. below and above the DRH [90,92,105,106]. The salt substrates are often exposed to enough humidity to form thick water multilayers while not fully deliquescing the underlying bulk salt, limiting the solution probed at a saturated concentration. If the salt film is thin enough to completely convert every salt atom to a liquid, then the amount of humidity introduced to the system can control the salt solution's concentration [92]. Experiments performed with a LMJ have greater sample customize by having full command of all salt solution parameters. Table 3.1 summarizing AP-XPS studies which have been conducted exposing solids salts to humidity and summarizes their experimental parameters. Synchrotron-based AP-XPS studies have frequently utilized variable X-ray excitation energies to adjust the interfacial probing depth in order to observe halide anion surface enhancement.

Table 3.1: AP-XPS studies of solid salts exposed to humidity with experimental parameters of substrate, humidity exposure in relation being above, below, or going through the DRH during the experiment, use of variable X-ray energy to probe interfacial ion distribution, and location of the experiment.

Year	Author Ref	Substrate	DRH	Measure Ion Dist.	Location
2016	Orlando[104]	NaCl film	Above	No	SIM/PHOENIX-SLS
2016	Tissot[103]	NaCl, NaI film	Above	No	TEMPO-SOLEIL
2015	Tissot[102]	NaCl, NaBr, NaI film	Above	Yes	TEMPO-SOLEIL
2011	Cheng[99]	RbCl, RbBr, NaCl(100) SC	Above	Yes	11.0.2 ALS
2010	Arima[92]	KBr/SiO ₂ film	Through	Yes	11.0.2 ALS
2010	Brown[108]	KIO ₃ film on KI(100) SC	Below	No	9.3.2 ALS
2010	Krepelova[101]	NaCl film	Above	Yes	11.0.2 ALS
2010	Newberg[107]	KBrO ₃ / KBr pressed pellet	Below	No	11.0.2 ALS
2009	Baer[105]	NaCl, NaClO ₄ film	Through	Yes	11.0.2 ALS
2008	Ghosal[106]	Br-doped/NaCl(100) SC	Through	Yes	11.0.2 ALS
2008	Verdaguer[100]	NaCl(100) SC	Below	No	11.0.2 ALS
2007	Krisch[109]	KI(100) SC	Above	Yes	11.0.2 ALS
2005	Ghosal[90]	KBr (100), KI(100) SC	Through	Yes	11.0.2 ALS

Microscopy studies have provided valuable information on the surface structure of salt interfaces and their changes due to the adsorption of water molecules and subsequent deliquescence. Scanning polarization force microscopy (SPFM) has enabled the study of soft surfaces, such as liquid films and aqueous solutions, which were previously challenging to image with traditional atomic force microscopy. Microscopy observations of water adsorption onto salts have been studied on NaCl [90,100,130-136], NaBr [130,131], KF [131,134], KCl [132,134], KBr

[107,131,132,134], and KI [108,132,137]. These microscopy studies mapped the physical changes that unfold on the solid surface as it interacts with water until complete solvation occurs. SPFM has provided the highest imaging resolution of the microscopic processes involved in the macroscopic transitions of solids to liquids. While spectroscopic techniques provide valuable information of water adsorption on salt, high-resolution microscopy is essential to reveal mechanistic understandings of the initial stages of adsorption and dissolution. Scanning probe microscopies revealed that salt dissolution was initiated at the sites of least coordination surface defects, such as steps or corner sites, of the salt surfaces. As the humidity is increased in the experiments layers of water molecules absorb on the salt which leads to terrace sites dissolution.

ZnBr_2 is known to be an extremely hygroscopic compound with a DRH point less than 10% at room temperature, allowing for the complete study of its phase transitions under ambient conditions [138]. Its hygroscopic nature makes it an attractive candidate to study water uptake as a system of solid-gas and liquid-gas at the salt interface, within the confines of a lab-based AP-XPS operational pressure range without having to drastically cool the sample to facilitate water condensation. Additionally, the small separation of binding energy (BE) between the Zn 3p and Br 3d core shells allowed for the investigation of anion to cation interfacial distribution of the same depth as a function of RH, which typically requires the use of adjustable synchrotron radiation to probe at a fixed depth. In this Chapter the surface chemistry of ZnBr_2 salt at both the solid-vapor and liquid-vapor interfaces upon exposure to water vapor was investigated using lab-based AP-XPS. To our knowledge this represents the first AP-XPS study on a triatomic halide salt assessing the phase change

across the DRH as well as the first AP-XPS investigation to attempt to quantify thermodynamics from isotherms over a range of temperatures. It will be shown that XPS peak widths, shifts, and relative surface composition of Zn, Br, and O change as a function of relative humidity. Herein we report the first instance of anion surface enhancement of an electrolyte using a lab-based AP-XPS technique. These results illustrate the capability of lab-based AP-XPS to investigate changes in electronic structure and surface composition of salts at heterogeneous interfaces.

3.3 Experimental Details

3.3.1 Sample Preparation

A ZnBr₂ solution was prepared by dissolving ZnBr₂ salt (Sigma Aldrich, 99.999 %, used as received) into 18.0 MΩ water. A sample was prepared for XPS analysis by depositing 2.0 μL of 0.52 M solution onto a polished and flame annealed gold foil (Alfa Aesar, 99.9975 %, 0.25 mm thick). The freshly deposited liquid drop was dried under nitrogen on a hotplate at 50 °C forming a homogeneous solid film. The film was transferred into the AP-XPS sample chamber where it was pumped for 24 hours reaching a base pressure of 1×10^{-8} Torr prior to the start of the experiments.

3.3.2 Ambient Pressure X-ray Photoelectron Spectroscopy (AP-XPS)

The surface chemistry of ZnBr₂ was probed using a lab-based ambient pressure X-ray photoelectron spectrometer (Scienta HIP-2 R4000) and a monochromatic Al anode X-ray source (Scienta MX650) operating at 20 mA and 10 kV in acceleration lens mode. AP-XPS experiments were performed over a pressure range of $\sim 10^{-8}$ to 2.5 Torr under isothermal conditions at -3.5, 8.0, and 20.0 °C to enable analysis of the

energetics of water adsorption onto the system. The temperature of the sample was controlled in each experiment with a chiller (NES Lab, RTE-140) circulating a mixture of 60% ethylene glycol and water through the XPS sample holder. Before each isothermal experiment, the ZnBr₂ salt sample was annealed to 100 °C to drive off surface adsorbed water and carbon species. Water vapor exposures were performed by back filling the AP-XPS chamber through a variable leak valve attached to a glass bulb containing 18.0 ΩM water. The water bulb was degassed by three freeze-pump-thaw cycles before each isotherm. Optical images were taken of the sample at every data point using a CCD camera (DCC1645C, Thorlabs) with a 10X lens (MLH-10X, Computar) mounted behind a CF viewport.

XPS spectra were collected in the Br 3d, Zn 2p(3/2), Zn 3p, O 1s and C 1s regions at 100 eV pass energy, while survey spectra were captured at 200 eV pass energy. All spectra were collected with the Au foil grounded to the AP-XPS spectrometer. Spectra were analyzed with Gaussian-Lorentzian fits with a Shirley background subtraction using peak fitting software (CasaXPS, v2.3.16). Doublets due to spin-orbital splitting in the Br 3d and Zn 3p regions were fit with known peak separations of 1.05 eV[139] and 3.0 eV,[140] respectively.

Due to large energy shifts in spectra before and after deliquescence, the initial discussion will center on the analysis of measured kinetic energies (KE). The KE of ejected photoelectrons is given by Equation. 3.1:

$$KE = h\nu + BE + \phi + E_c \quad (3.1)$$

where the photoelectrons are measured by the spectrometer with a work function of ϕ . Employing the conservation of energy, the relationship between light energy and kinetic energy is obtained when including the amount of charging the sample

experiences, E_c , and the orbital binding energy, BE. The amount of charging a surface experiences is dependent on X-ray flux, photoelectron emission cross-section, and the band gap of the surface which influences the ability of electrons to replenish photogenerated holes. When reporting BEs, spectra were internally referenced to the aliphatic component of the C 1s spectra at 285.0 eV in order to mitigate charging effects.

3.3.3 Scanning Electron Microscopy (SEM)

Scanning electron microscopy (SEM) is a technique which provides very high-resolution images at enhanced magnification of the topography and composition of a surface. The microscope produces high-resolution images of the sample by scanning the surface with a focused electron beam and detecting signals that are dependent on surface morphology and elemental composition. Images within this Chapter were collected in secondary electron mode where the microscope collects low-energy secondary electrons that are ejected from the core shell of the sample atoms from inelastic scattering collisions with the beam electrons. SEM (Zeiss Auriga 60 FIB/SEM) collected surface morphology images were collected in secondary electrons mode with an accelerating energy of 3 keV and a working distance of 5.0 mm.

3.4 Results and Discussion

3.4.1 Effect of Water Adsorption on Zinc Bromide Surface Charge Compensation Through Dissolution and Ionic Mobility

The system that is being studied is the adsorption of water onto a film of $ZnBr_2$ salt, of which the solid film formed after evaporation under vacuum and annealing, so the first stages of the experiment were to characterize the dry film prior to water

uptake. Optical images of the dry ZnBr₂ film (**Figure 3.2a**) perceive a thick uniform film atop the gold foil substrate that transitions after deliquescence to liquid. Clear visual changes were observed at the solid to aqueous phase transition, optically confirming the complete solvation of ZnBr₂. SEM images were taken to confirm surface morphology was homogeneous after deposition and without evidence of the underlying gold substrate beneath the film. The same homogeneity of the sample surface viewed under XPS would also be assumed given that the probing depth of secondary electrons from SEM are 10 to 100 nm which are an order of magnitude higher than electrons escape depth from XPS. A survey spectrum of ZnBr₂ at an initial base pressure of 1.2×10^{-7} Torr (**Figure 3.3**) shows Zn and Br peaks from the salt as well as C 1s and O 1s peaks due to advantageous carbon and hydrate species present on the salt surface. No other elements were detected in the survey indicating the other potential contaminants were below the detection limits of XPS. No Au peaks were observed, confirming the homogeneity of the sample covering the underlying substrate and in good agreement with microscopy images. The homogeneity of the sample surface is critical in the quantitative evaluation of water uptake, where XPS data is interpreted to be solely of ZnBr₂ and water interactions. The absence of gold in XPS and SEM observations would exclude any potential interactions of water adsorption on gold from influencing any subsequent observations during the experiment.

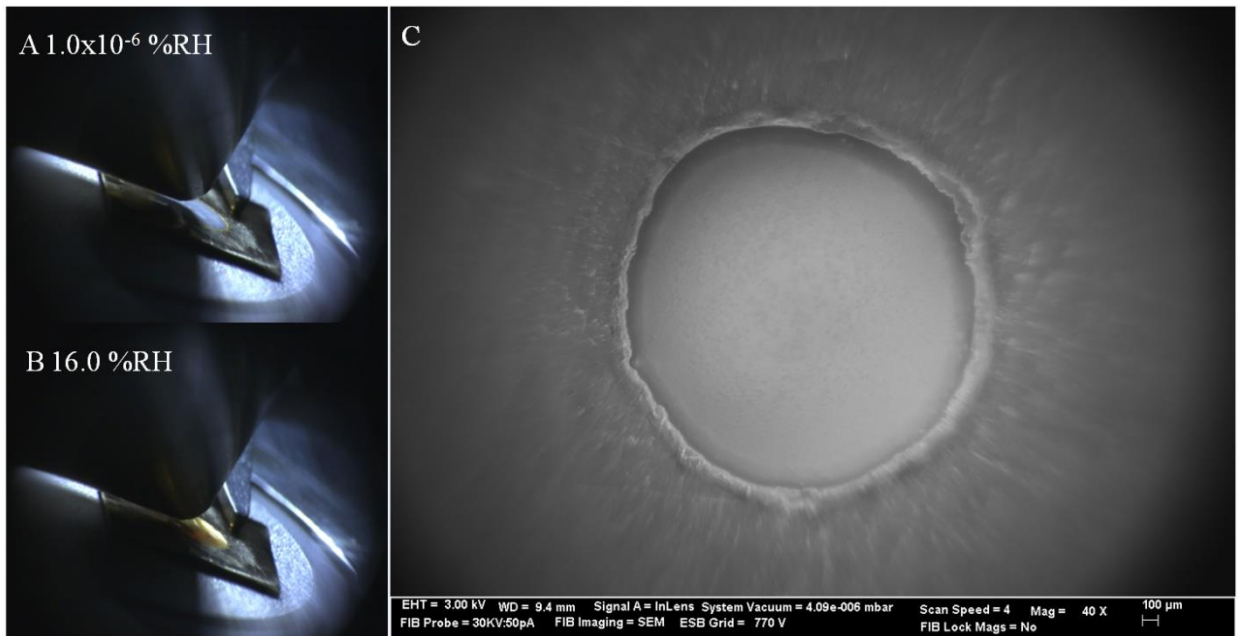


Figure 3.2: Optical images taken of the sample during the $-3.5\text{ }^{\circ}\text{C}$ isotherm where A and B correspond to the pressures of 4.0×10^{-8} and 0.61 Torr, respectively. Image C was SEM image taken using secondary electron imaging detector and with a 3.00 kV electron beam and 40x magnification.

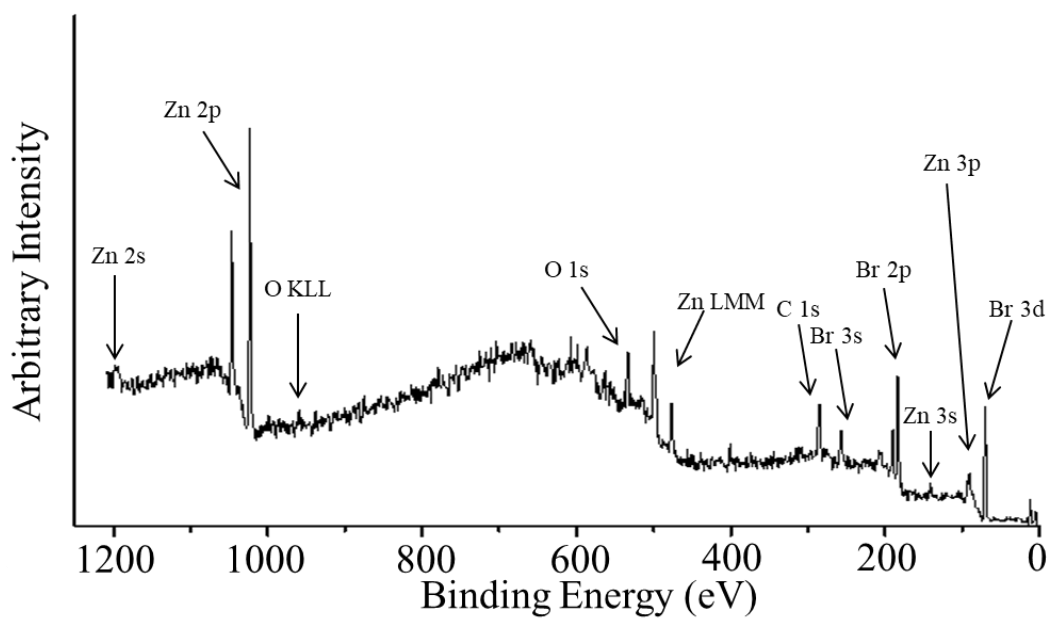


Figure 3.3: Survey spectrum of ZnBr_2 film on Au foil under vacuum.

After the characterization of the dried film the sample was incrementally dosed with increasing pressures of water vapor. The low DRH point of ZnBr_2 induced water adsorption events at low pressures which cascaded into the phase transition of the solid to an ionic solution. **Figure 3.4a** shows Zn 2p(3/2) spectra for a -3.5°C isotherm as a function of increasing RH. The salt sample initially experienced charging effects with a kinetic energy shift of ~ 18 eV, relative to the deliquesced samples, which indicates an insulating sample under vacuum conditions. Solid zinc bromide is an insulator with a wide band gap of 3.2 - 3.4 eV [141-143]. The spectra in **Figure 3.4a** are therefore representative of the changes the sample experiences due to charging. As

the RH was elevated, the amount of charging was reduced as the conductivity of the sample increases which in turn increases the KE of the ejected photoelectrons.

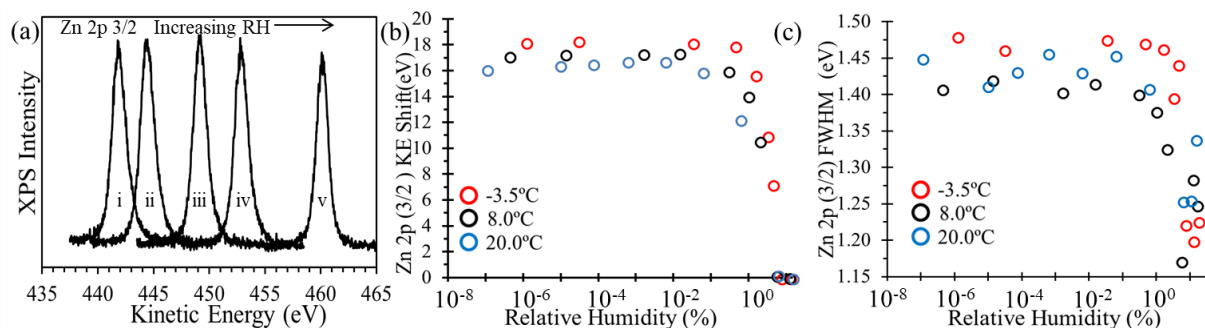


Figure 3.4: (a) Zn 2p(3/2) spectra displayed with increasing RH from the -3.5 °C isotherm. Spectra of i-v correspond to a RH of 1×10^{-6} %, 1.4 %, 2.9 %, and 6.6 % respectively. (b) plots the binding energy shift Zn 2p(3/2) of the isotherms as a function of RH. (c) FWHM values of Zn 2p(3/2) as a function of RH.

Figure 3.4b displays the shifts in kinetic energy of the Zn 2p(3/2) of each isotherm towards higher KE as RH was increased. The mechanisms of water dissolution occur in several stages, during which the water pressure is elevated high enough such that the adsorbed water can solvate surface ions thereby increasing the surface conductivity [134,144]. Molecular dynamic simulations have been conducted on NaCl dissolution which elucidated a multistep pathway from water adsorption to ion solvation to water film formation by Lui et al. [145,146] After water adsorption to the surface the dissolution process is initiated by the departure of Cl ions from the crystal lattice, then an intermediate state in which the departing anions remain partially solvated but are still contact with the crystal. Once the Cl ion is removed from the

lattice is leaving an uncoordinated Na ion exposed to water and ready for subsequent dissolution. The first stage of ion solvation would occur preferentially at defect sites, kinks, and step edges of the solid, where the Madelung constant is lower, followed by solvation of ions in the terraces of the crystals [135]. This characteristic of step solvation dependence on relative humidity has been observed by SPFM for several salts including NaCl, KCl, KBr and KI [132,133]. Changes in ionic mobility on the surface are manifested as slight shifts towards higher KE (lower BE) with the increase in RH. The final stage of solvation occurs upon ZnBr₂ deliquescence. The thick water film was then able to solvate the ions within the bulk and deliquesce the solid.

ZnBr₂ deliquesces within the range of 8.0 to 9.1 % RH when temperatures range from -3.5 to 20 °C [138]. As the water layers build up, the dissolution of the zinc bromide creates a highly concentrated ionic solution that can significantly dissipate the charging induced from photoemission. AP-XPS studies of mica samples observed apparent BE shifts of 200 eV due to the increased mobility of solvated K⁺ ions at the surface [4]. Above the deliquescence point there is no additional KE shift (**Figure 3.4b**), indicating that charging effects at the sample surface is completely removed. The BE of the fully charge equilibrated spectra, averaged over all isobars post deliquescence, (relative to C 1s alkyl = 285.0 eV) for Zn 2p(3/2) and Br 3d(5/2) are 1023.1 ± 0.1 eV and 69.4 ± 0.2 eV, respectively, which are in good agreement with literature values [147,148].

The BE shifts and full width at half maximum (FWHM) of each component become narrow at higher relative humidity, at which point the sample has deliquesced. The resolution of the spectra improves, despite the decrease in signal when the system is under pressure, where the highest pressure was at 0.61 Torr H₂O at which point the

gas phase attenuates ~67 % of the XPS signal compared vacuum conditions, due to the charging induced broadening effects being removed. **Figure 3.4c** summarizes the effect on FWHM with increasing relative humidity for Zn 2p(3/2) spectra which are the most intense spectral lines in the sample (**Figure 3.3**). As the RH was heightened over the salt, the spectra's FWHM values decrease, which can be related to the same mechanisms of water adsorption over ionic salts observed within **Figure 3.4b**. Charge dissipation does not occur until a significant amount of solvated surface ions are generated and became mobile creating an increase in conductivity. Since the sample was a crystalline powder, many surface facets were exposed, adding to the amount of energy states sampled, and ultimately contributed to a broader FWHM. Beyond ~4.0 % RH the samples appear to reach charge equilibrium given that the BE and FWHM values remain relatively constant with further increase to relative humidity. Similar behavior in spectral features have been observed by Verdaguer et al. [100] on NaCl single crystals exposed to high RH, where the core shell of Na 1s and Cl 2p shifted to lower BE and FWHM was reduced as the sample approached deliquescence.

3.4.2 Quantitative Analysis of Water Uptake with the Clausius-Claperyon Relation

The quantitative analysis of water uptake onto the ZnBr₂ salt surface begins with the analysis of the oxygen components in the O 1s spectra. Essential information can then be derived of water uptake from changes to the components of the O 1s spectra, a representative spectral set from an 8.0 °C isotherm is displayed in **Figure 3.5**. When under UHV and low humidity conditions (<0.10 % RH) a single BE feature, at a position of 532.5 eV, was observed. This species decreases in intensity with the increase of humidity, leading to a possible assignment of adsorbed oxygen

species and hydrates trapped within the bulk salt and/or carbonaceous contaminants containing oxidized species which are observable in the C 1s spectra (**Figure 3.6**). The source of the carbon is expected to be from the solution preparation of the salt film, the ambient exposure of the sample to air, and from desorbed molecules from the walls of the vacuum. The amount of carbon contamination over the course of the experiment was constant until the deliquescence point was reached at which point the amount of carbonaceous material increased, presumably having been liberated from the bulk solid and segregated towards the aqueous interface.

XPS of ZnBr_2 supported on nanoparticles of $\text{Fe}_3\text{O}_4@ \text{SiO}_2$ observed a similar species in the O 1s spectra at 532.5 eV, attributed to adsorbed oxygen and oxygen species and can be correlated with H_2O vibrational bands observed with infrared spectroscopy [149]. Given the well-known hygroscopic nature of $\text{ZnBr}_2 \cdot 2 \text{H}_2\text{O}$ [150] the ex-situ heating of the sample would not completely drive off all hydrates present in the sample as the sample is rehydrated from any exposure to atmosphere prior to entry into the vacuum and even after the sample was annealed to 100 °C not all the hydrate may be driven away nor can the possibility of hydration on the surface from water present in the vacuum be excluded. Therefore, it is likely to conclude that the hydrate remains present in the evaporated film. The existence some hydrated would thus be wholly expected to be present in the initial sample as this is the common form of ZnBr_2 occurs naturally in any environment with humidity below its DRH [151]. The hydrate form of NaCl has only been observed from the evaporation of the solution by AP-XPS and NEXAFS, and not the exposure of dry NaCl to water [101,104]. If it were to be completely attributed to the hydrate form of $\text{ZnBr}_2 \cdot 2 \text{H}_2\text{O}$ than the entire substrate would not be fully in this form as its molar ratio of hydrated oxygen to zinc

is approximately 0.52 at vacuum. The possibility of water dissociation forming a hydroxide species cannot be ruled out as the splitting has been observed at defect sites of the salt surface by several experimental techniques [152-154].

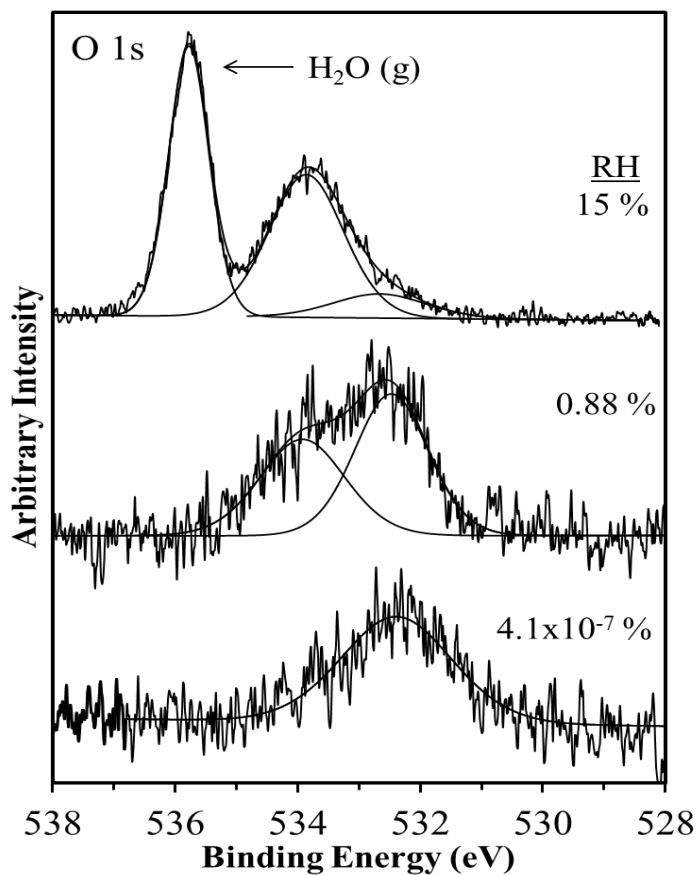


Figure 3.5: O 1s spectra displayed are from the 8.0 °C isotherm at the pressure of 3.3×10^{-8} , 7.6×10^{-2} , and 1.2 Torr corresponding to 4.1×10^{-7} , 8.8×10^{-1} , and 15%RH, respectively, shown from top to bottom.

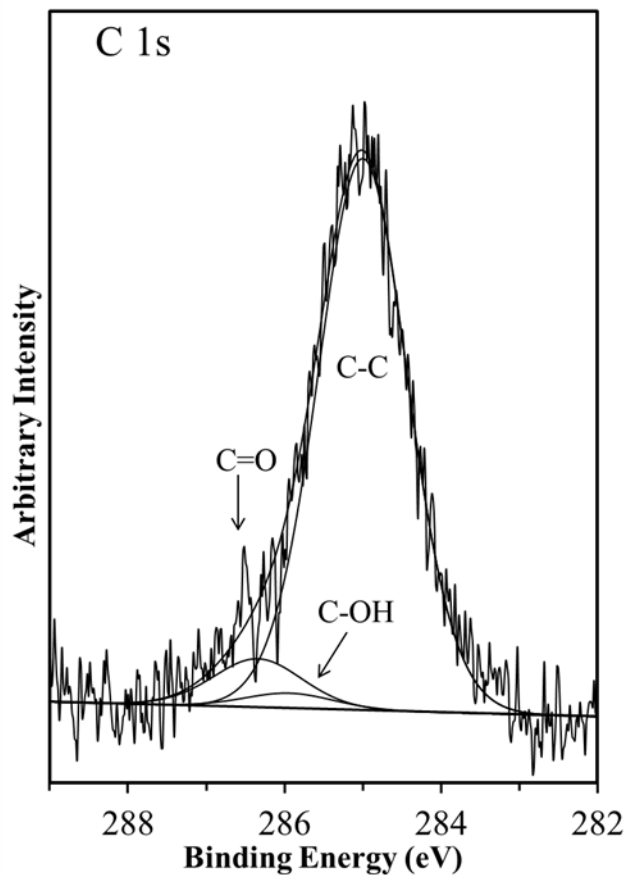


Figure 3.6: Hi resolution spectra of C1s of $-3.5\text{ }^{\circ}\text{C}$ isotherm. C 1s components were constrained to a full width at half maximum equivalent among each component at a value of $\sim 1.1\text{ eV}$. The aliphatic carbon has a binding energy of 285 eV, while alcohol and carbonyl functional groups are shifted by $+0.94$ and $+1.16$ eV respectively. Other components were not observed in the C 1s spectra.

Under hydrated conditions the spectra were fit with two unconstrained peaks with a BE difference between the components of ~ 1.5 eV, and the BE were internally referenced to the aliphatic C 1s component of 285.0 eV. The higher BE component

can be assigned to adsorbed water on the surface with a BE of ~ 534.0 eV. The peak attributed to adsorbed water increases with the rise in water pressure and is initially observed when the RH rises above 0.05%. At water pressures above 0.2 Torr an additional photoelectron contribution can be observed in the O 1s spectra at a BE of 536.0 eV. The BE of this third peak and its low FWHM of ~ 0.8 eV was indicative of photoelectrons generated from the gas phase of H_2O above the sample surface. The rise in the adsorbed component has been observed in previous reports of salt and water uptake. Arima et al. [92] observed spectral changes of thin KBr films on SiO_2 as a function of RH through the deliquescence of KBr. In **Figure 3.4c** it can be seen that the FWHM of the adsorbed water peak decreased slightly as the RH was increased which was consistent with the previous report [92].

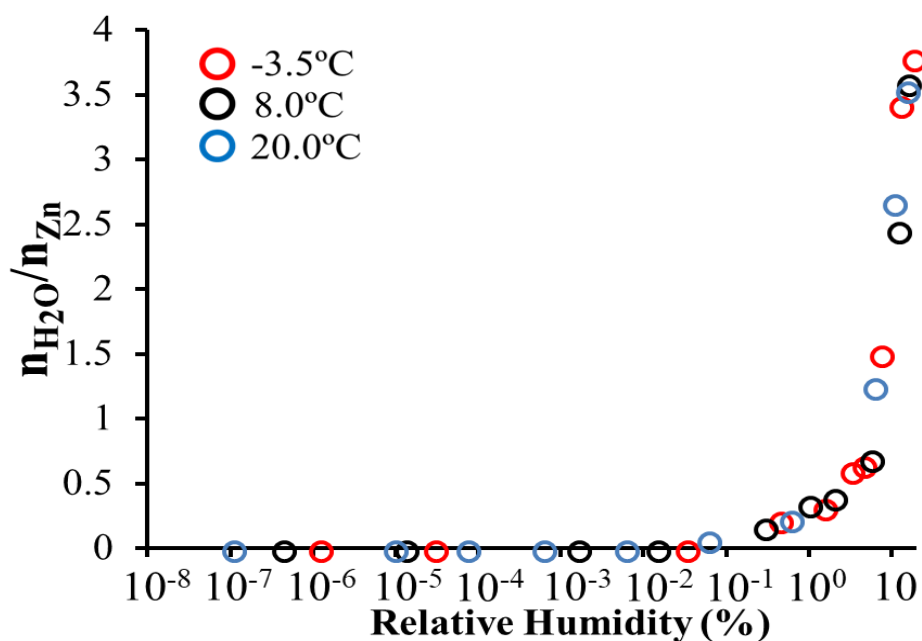


Figure 3.7: The molar ratio of adsorbed water to zinc atoms of each isotherm plotted as a function of relative humidity.

The uptake of adsorbed water was also consistent with observations made on other salt substrates. The molar ratio of the adsorbed water species to Zn atoms was plotted against relative humidity, which were calculated with correction for gas phase attenuation (Equation 3.2-3.7). In conventional UHV XPS quantitative analysis the intensity of a core shell is defined by Equation 3.2,

$$I_a^j = \Phi_{a(hv)} \sigma_{a(hv)}^j B_{a(hv)}^j T_{(KE)} N_a \lambda_{a(KE)} \cos(\theta) \quad (3.2)$$

where I is the intensity of orbital j of element a , Φ is the X-ray flux upon the sample, σ is the photoionization cross section of orbital j of element a , B is the orbital asymmetry factor of orbital j at angle θ , T is the detector efficiency of electron of a certain KE, N is the atomic concentration of element a in the sample, λ is the IMFP of an electron of element a with a certain KE through the sample, and θ is the emission angle of the photoelectron [155].

An XPS sensitivity factor can then be defined by Equation (3.3) from solving Equation (3.2) for the atomic concentration.

$$N_a = I_a^j / S_a^j \quad (3.3)$$

Where S_a^j is the sensitivity factor for an electron from orbital j of element a . Sensitivity factors are largely material independent in the UHV, as the ratio of the IMFP between two different materials is negligible since the difference in density between two solids is not typically dramatic. This is not the case with ambient pressure instruments as the difference in the density of gas above the sample surface can vary many orders of magnitude over the course of an experiment. This attenuation is dependent on the kinetic energy of the emitted photoelectron and can be

circumvented in synchrotron facilities by adjusting the energy of the probing light to have constant KE from various elements. The fixed energy X-ray source of Al K α irradiation produces photoelectrons of different kinetic energies for different elements and thus each photoelectron has its own IMFP through the gas phase. The attenuation of an electron through a gas phase can be defined by Equation (3.5),

$$I/I_0 = e^{\frac{-d_{eff}}{\lambda_{H_2O}}} \quad (3.5)$$

where I is the intensity of the sample attenuated by gas phase of H₂O, I_0 is the intensity of the sample under vacuum, d_{eff} is the effective distance the photoelectron travels through the gas phase, and λ_{H_2O} is the IMFP of the photoelectron through gas phase H₂O. The IMFP of an electron through a gas phase can be defined by Equation (3.6),

$$\lambda_{H_2O} = \frac{k_B T}{p \sigma_{H_2O}} \quad (3.6)$$

where k_B is the Boltzmann constant, T is the temperature, p is the pressure, and σ_{H_2O} is the total electron scattering cross section of an electron at a certain KE through H₂O gas. In Chapter 2 the distance d_{eff} , was defined with our AP-XPS instrument [70] and the total electron scattering cross section σ_{H_2O} was defined in a separate publication by Khalifa et al. [156] and when combined sensitivity factors derived from a single crystal of ZnO the molar composition of ZnBr₂ can be expressed in Equation (3.7).

$$N_a = I_a^j / S_a^j e^{\frac{-d_{eff} p \sigma_{H_2O}}{k_B T}} \quad (S4)$$

Taking this equation alongside the sensitivity factors obtained from XPS spectra of a ZnO single crystal yield a molar comparison of zinc atoms to water molecules.

At low RH the molar ratio of water to zinc remained unchanged until the RH was increased past 0.1 %, where the molar ratio then increases. The increase can be attributed to the appearance and growth of the adsorbed water component of the O 1s spectra. Above ~1 % RH the ratio increased more drastically, which was attributed to the formation of multilayers of water near this RH range. The growth of water layers and subsequent deliquescence of KBr films on SiO₂ has been previously quantified with AP-XPS; the rate of water uptake was shown to greatly increase past the deliquescence point [92]. Verdaguer et al. [100] observed similar behavior of the O 1s peak intensity rising with RH, directly corresponding to spectral changes within the anion and cation core shells. Growth of the O 1s core shell directly corresponds with the formation of molecularly thin water layers. When the mole ratio was plotted against RH, the increase observed in the three isotherms had the same rate of increase, indicating that the mechanism for water adsorption was dependent on RH. The deliquescence of ZnBr₂ occurs within the range of 8.0 to 9.1 % RH over the temperature range of -3.5 to 20 °C [138] beyond which there were significant increases in the adsorbed water component of the O 1s spectra corresponding to bulk water formation. The molar ratio of water to zinc during this phase transition occurs around ~ 1:1 H₂O to Zn suggesting that the conversion from solid to solution does not progress through the ZnBr₂·2 H₂O hydrate form. This is consistent with observations of the phase transitions of NaCl with AP-XPS near its eutectic point, in which the hydrate phase was only created through the evaporation of water from the system [101,104].

Isotherms collected across a range of temperatures can yield quantitative thermodynamic values yielding free energy, enthalpy, and entropy as a function of adsorbate population. Spectroscopically these adsorption energies have been thoroughly assessed for the NaCl/water system by the likes of Ewing et al. [157-159] with FTIR. There have been numerous AP-XPS studies of salt/water interfaces,[90,92,99-129,136,160] however none have attempted to quantify adsorption energies from temperature dependent isotherm studies. Clausius-Clapeyron relation of pressure and temperature (**Figure 3.8a**) were derived from the mole fraction of the adsorbed water in the system stemming from the spectral components within the O 1s and Zn 2p(3/2) derived from Equations 3.2-3.6.

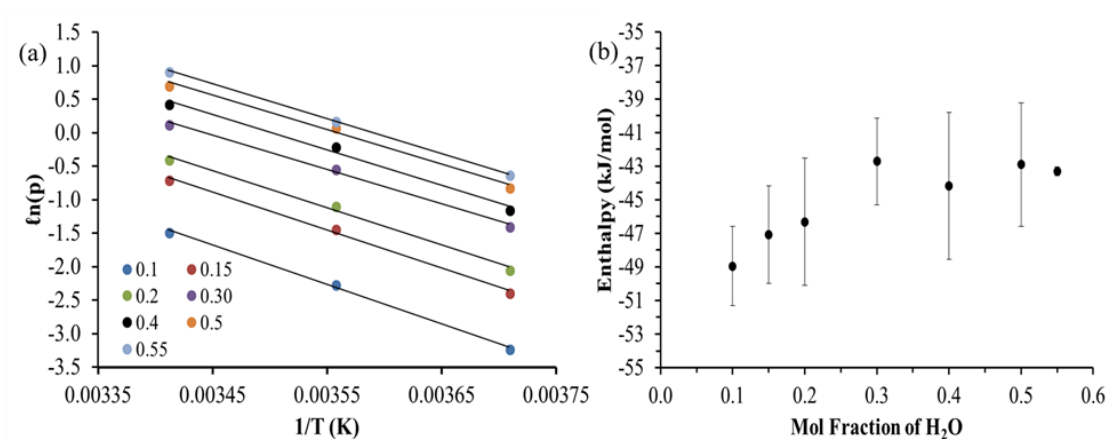


Figure 3.8: (a) Plots of the $\ln P$ vs. $1/T$ (K) of mole fractions of adsorbed water and the linear least squares regression through the three temperatures. (b) The enthalpy of water adsorption plotted as a function of water mole fraction in the $ZnBr_2$ system.

The slope from Clausius-Clapeyron relation corresponds to the enthalpy of adsorption, ΔH_{ads} , of water from gas phase onto the zinc bromide system over the mole fraction ranges of water from 0.10 to 0.55 (**Figure 3.8b**). The error bars associated from with the ΔH_{ads} was determined from the standard error of the regression slope within **Figure 3.8a**. The data indicates that the ΔH_{ads} on zinc bromide is initially more favorable than the water-water interaction. The ΔH_{ads} decreases as more oxygen is added to the system. From a molecular perspective, the low deliquescence point of ZnBr_2 would indicate that the enthalpy of adsorption be very favorable and as the relative humidity increases the gas phase water molecules at the interfacial region would interact with more water at the surface, which would cause an increase to the enthalpy of adsorption. Once the salt has deliquesced, any elevation of RH would dilute the solution and provide less favorable adsorption sites for gaseous water. Past the mole fraction of 0.30 the enthalpy of adsorption approached the enthalpy of adsorption for pure water, indicating that the enthalpy of interfacial water uptake had made a transition from water-ion interactions to water-water interactions. Under standard temperature and pressure, the ΔH_{ads} of water into pure water is -44 kJ/mol, which the experimental data would approach at infinitely increasing water mole fractions.

3.4.3 Ion Segregation at the Liquid/Gas Interface: Evidence of Anion Surface Enhancement from Coordination with Water

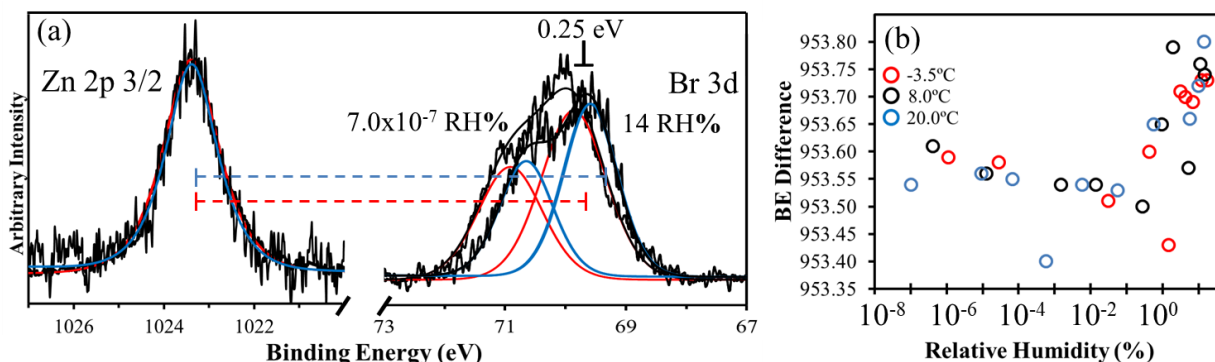


Figure 3.9: Internal relative binding energy shifts (a) Br 3d(5/2) and Zn 2p(3/2) spectra at pressures of 1.8×10^{-8} and 2.5 Torr, corresponding to 7.0×10^{-7} and 14 % RH, respectively. (b) BE difference of the Zn 2p(3/2) and Br 3d(5/2) as a function of RH.

The local electronic environment of the salt can be monitored by the BE shifts of the core shells. The low and high RH spectra of Zn 2p(3/2) and Br 3d are displayed in **Figure 3.9a**, with spectra calibrated to the aliphatic carbon species. The Br 3d shifts ~ 0.25 eV towards a lower BE, from the vacuum spectra to the deliquesced spectra, with respect to the Zn 2p(3/2) spectra fixed at the position of a constant BE of 1023.1 eV. The shift provides information about the effect of solvation on the coordination of the water molecules around the ions of the salt. **Figure 3.9b** displays the BE difference of Zn 2p(3/2) and Br 3d(5/2) as a function of increasing relative humidity, which shows a consistent shift of the Br 3d towards lower BE as relative humidity increases. Similar relative BE shifts due to solvent effects have been observed in LMJ experiments of salt solutions [119,121,122]. It has been shown that the existence of hydrogen bonding in solvents, particularly water, leads to larger solvation energies, which translates to higher core-level binding energies [121]. Studies using neutron

diffraction on ZnBr_2 aqueous solutions have reported that the solvation shell of the Br ions is composed of several water molecules bound to the anion by one hydrogen atom, whereas Zn ions are bonded to oxygen atoms of six water molecules forming an octahedron [161,162]. Given that the shifts are a function of RH, it can be assumed that the magnitude of the shift was directly related to the number of hydrogen bonds around the solvated ions. The nature of the binding energy shift corresponds to the bromide ion being solvated with a hydrogen bond from water, which would cause an increase in the binding energy relative to zinc as seen in **Figure 3.9b**, where the core hole of the bromide anion is better screened by the electron density contribution of the surrounding water molecule compared to the solid salt. Past the deliquescence point the solvation shells of the salt ions would be fully formed and the BE differences would stabilize.

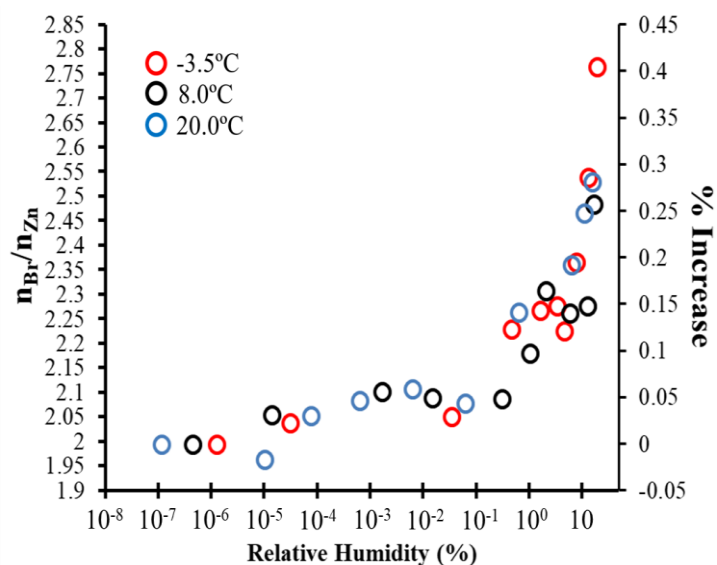


Figure 3.10: The anion to cation ratio is plotted as a function of RH. The molar ratio of the Zn 3p to Br 3d of the UHV spectra was the baseline percentage increase.

The direct enhancement of halide ions at the surface of water interfaces has been well studied in literature by AP-XPS for alkali halide salt solutions [90,92,99,101,102,106,109,112-114,124]. Typically, the enhancement can be observed with X-ray spectroscopy by tuning the excitation energy at synchrotron facilities allowing for extremely surface sensitive measurements; however, it is more difficult to observe with a traditional monochromatic X-ray source. In this study the close proximity in binding energies of the Br 3d and Zn 3p spectral lines at 68.9 eV and 89.5 eV, respectively, were utilized to approximate the anion enhancement at the surface. The proximity results in ejected photoelectrons with similar kinetic energies, allowing for the direct comparison of the core shells that are of the same escape depth and without significant differences in attenuation from the gas phase. In **Figure 3.10**, the ratios of the spectral intensities between the two elements were plotted against increasing relative humidity and normalized to their ratio under vacuum. Compared to the vacuum spectra, the fully solvated spectra display an over 25 % increase of Br/Zn molar ratio past the deliquescence point for ZnBr₂. The percent increase of the halide surface enhancement can be defined by Equation (3.7):

$$\frac{(n_{Br}/n_{Zn})_{RH}}{(n_{Br}/n_{Zn})_{UHV}} - 1 \quad (3.7)$$

Experimental and molecular simulations have focused on binary alkali halide salts as the primary substrate for observing ions at the liquid-vapor interface. There has been comparatively less work done emphasizing cations outside of the alkali metal series or of higher formal charge. The magnitude of the increase in the Br/Zn ratio was in line with that of synchrotron KBr studies that probed the surface at a KE of 200 eV, which suggests the large polarizable anion of Br in ZnBr₂ is subjected to similar

asymmetric hydration forces, leading to its enhanced anion densities at the surface. The Al K α excitation energy results in KE of the ejected photoelectrons collected within **Figure 3.10** to be approximately 1,400 eV, which produces an IMFP that is several times deeper than the typical synchrotron experiment based on the universal IMFP curve [124]. The literature generally agrees that the halide enhancement is pronounced at the surface with the larger and more polarizable ions in the series (F⁻ < Cl⁻ < Br⁻ < I⁻) and that at deeper depths within the solution the cation density would be restored and the ion pairs would reach their bulk concentrations [97]. The surface sensitivity of XPS is able to capture this depth dependent enhancement, since the majority of its signal is generated from the first few layers of the sample due to electron attenuation. The asymmetric concentration of the ions at the interface may influence kinetic rates of reactions occurring at the liquid-vapor and liquid-electrode interfaces.

3.5 Conclusions

To the author's best knowledge this is the first study by lab-based AP-XPS to characterize the water adsorption and subsequent deliquescence of a salt film. The changes in the charge compensation, core shell binding energies, and peak widths were examined on the insulating sample as a function of relative humidity. The extent of ion mobility begins with defects and steps, followed by terrace solvation beginning at a RH of ~0.10% based on the charge dissipation observed in the spectra. Complete charge equilibrium was established upon sample deliquescence beyond ~9.1% RH, at which point changes can be observed in anion/cation ratio. An enhancement of bromide was detected at the surface which can affect the chemistry of heterogeneous processes of zinc bromide solutions. The enhancement can be described purely in

terms of asymmetric hydration forces where the bromide anion forms weak interactions with water, weaker than water to water, and there can be more excluded surrounding hydrogen bond network. In contrast, the zinc cation creates stronger interactions with water molecule and is able to break a hydrogen bond of a water-water and are more hydrated than the anion. The anion then preferentially exists at the hydrophobic interface of the solution/vapor junction over being solvated. AP-XPS was shown to resolve changes in the core shells of the Zn 2p and Br 3d, which have orbitals with electronic structures that are sensitive to solvating molecules.

Chapter 4

HYDROXYLATION OF METAL OXIDE ULTRA-THIN FILMS SUPPORTED ON SILVER SINGLE CRYSTAL

4.1 Abstract

In this Chapter the interaction of water with MnO(1x1) and NiO(1x1) thin films on Ag(100) was investigated. X-ray photoemission spectroscopy (XPS) and scanning tunneling microscopy (STM) was used to measure dissociative (OH) adsorption onto submonolayer MnO(100) and NiO(100) films. The mechanism of a high barrier to water dissociation for MnO(100) films was examined by *in-situ* XPS which had increased hydroxylation associated with MnO(100) terrace sites at elevated water pressures of 2.5 Torr, wherein the surface OH concentration increases from 29 % under vacuum conditions to 66 % after exposure. The interactions of water vapor with monolayer NiO/Ag(100) were also examined in this study. Initial film growth was characterized by STM low energy electron diffraction showing the formation of NiO(1x1) after annealing of the initial deposition. XPS revealed that the deposited films of MnO and NiO oxide contained small amounts of hydroxyl groups (OH) attributed to the dissociation of background water vapor at highly reactive edge sites. XPS results indicate that upon exposing the oxide film to high water vapor pressures (maximum 2.5 Torr), extensive hydroxylation occurs which is attributed to water dissociation at terrace sites. Theoretical calculations of both film types revealed that upon aggregation of water monomers to dimers at the oxide interface the dissociated dimer is energetically stable. The results herein are consistent with previous

MgO/Ag(100) studies, further revealing that for certain metal oxides the formation of water dimers at the metal oxide-vapor interface is a key mechanism leading to extensive terrace site hydroxylation. The preference of the films to hydroxylate at increased water vapor pressures can also evidence chemical relaxation reducing the steric strain of the epitaxial films even after annealing to a stable overlayer phase.

4.2 Introduction

Hydroxylation of metal oxide interfaces are known to affect the electronic properties of the surface and to change its reactivity towards gas phase adsorbates [163-167]. The degree to which hydroxylation occurs over metal oxides depends upon the surface chemistry and morphology. The focus of this Chapter is on the investigation of the hydroxylation of two different metal oxide films of manganese oxide and nickel oxide. Understanding the surface chemistry of manganese oxides has important implications in catalytic [168-171], electrochemical [172,173], magnetic [174-176], and atmospheric aerosol processes [177-179]. Manganese oxide films have also been employed in a number of applications, including sensors [180], electrodes [181,182], ion exchange [183], and catalytic materials [184]. Ultrathin metal oxide films are used as systems for studies at the nanoscale because the issue of sample charging is circumvented. Ultrathin metal oxide films have potential to serve as substrates for metal particles for catalysis, solid fuel cells, ferroelectric ultrathin film capacitors, and tunneling magnetoresistance sensors [185,186]. Any practical application of metal oxide films would necessitate chemical and structural understanding of the interfacial region, particularly its heterogeneous interactions with water and subsequent impact on those properties.

Surface science studies of MnO thin films have been reported on many supports, including Rh(100) [187], Rh(111) [188], Pt(111) [189-192] and Pd(100) [193,194]. MnO on Ag(100) has been fairly well characterized utilizing a number of surface techniques, including scanning tunneling microscopy (STM) [195], low energy electron diffraction (LEED) [195-200], X-ray photoelectron diffraction (XPD) [198,199], near edge X-ray absorption fine structure (NEXAFS) [200], and XPS [197,200,201]. MnO films on Ag(100) are tetragonally distorted due to the lattice mismatch of about 9% [202] with a relaxation of the lattice away from the MnO/Ag(100) interface for multilayer MnO films. LEED studies on multilayer MnO/Ag(100) show there is significant rumpling of the oxygen atoms towards the vacuum [196]. However, rumpling of the top layer of a cleaved single crystal MnO(100) surface has also been observed with an outward displacement of Mn [203]. The difference may be explained by the strain films have from the substrate mismatch, photoelectron diffraction (XPD) results of MnO films indicated distortion occurring for the first few nm, while thicker films greater than 5 nm adopted bulk structure and bulk lattice constants [199]. There is a lack of STM results regarding the nature of thin MnO films on Ag(100) within the literature, recently MnO(2x1)/Ag(100) nanostripes were observed with LEED and STM on Ag(100) [195]. Structural details of submonolayer MnO films on Ag(100) have not been well under varied preparation conditions using microscopy techniques.

Nickel oxide (NiO) films have been used in a variety of technological applications ranging from optoelectronic devices [204], fuel cells [205], magnetic pinning layers [206] and sensors [207]. The dissociation of water at metal oxide interfaces leads to hydroxyl groups, thereby significantly altering chemistry and

properties of the metal oxide interface [3]. Supported metal oxide thin films can react differently towards water depending on the film thickness [208]. This suggests that the efficacy for water dissociation to occur can be fundamentally controlled. It is therefore important to understand the extent to which metal oxides hydroxylate on a molecular level upon exposure to water. Herein we examine the interaction of water with monolayer NiO supported by Ag(100) in order to reveal the mechanism of water adsorption and dissociation.

A number of vacuum-based surface science studies have examined the interaction of water with an NiO(100) single crystal and Ag(100) supported NiO films utilizing X-ray photoelectron spectroscopy (XPS), ultraviolet photoelectron spectroscopy, temperature program desorption and low-energy electron diffraction (LEED) [209-215]. These experiments suggest that defect sites are reactive towards the dissociation of water, while stoichiometric terrace sites of the NiO(100) interface are unreactive upon exposure to water vapor. The lack of extensive reactivity could be due to the low water vapor pressures used to expose samples under high vacuum.

A number of molecular simulation methods have been utilized to examine the interaction of water with NiO(100), including MSINDO [216,217] and GGA+U [218-220]. Simulation results agree with the aforementioned surface science studies, indicating that water adsorption at NiO(100) terrace sites are predicted to be more favorable in the molecular state rather than the dissociated state for low water coverages. However, there is evidence that multilayer water adsorption, a representation of NiO(100) in contact with bulk water, leads to partial dissociation within the first water layer at 293 K [218]. The aforementioned molecular simulations were performed on bulk terminated NiO(100) [216-220]. Given the lack of NiO(100)

terrace site reactivity observed experimentally for low water vapor pressures exposures[209-215], we hypothesized that exposure to higher water vapor pressures may lead to additional reactivity at terraces.

Herein we use a combination of experimental techniques to examine the interaction of water with submonolayer MnO(1x1) and NiO(1x1) deposited onto Ag(100). Film quality was assessed using LEED and STM, and surface hydroxylation was identified using XPS before and after exposure to water vapor. STM and LEED were utilized to determine film quality while the chemical composition and extent of metal oxide hydroxylation was monitored using XPS following *in-vacuo* exposures to water vapor. MnO and NiO film properties on Ag(100), the adsorption of water and the tendency of water to dissociate at the film surface were analyzed at different water pressures, reproduced with permission from [221,222]. The results were compared to experimental and computational studies and the mechanisms for water dissociation were expounded upon.

4.3 Experimental Details

Experiments were performed at the Center for Functional Nanomaterials at Brookhaven National Laboratory using an ultra-high vacuum system consisting of three chambers, including an analysis chamber, preparation chamber, and a fast entry chamber. Scanning tunneling microscopy (STM) was performed in the analysis chamber (RHK, VT-STM/AFM) at room temperature with images captured under pressures of $< 3 \times 10^{-10}$ Torr. The substrate was grounded through a Molybdenum ring that mounted the sample to the manipulator holder.

4.3.1 Sample Preparation

MnO and NiO ultra-thin films (sub one monolayer) were deposited on an Ag(100) single crystal using molecular beam epitaxy. The Ag(100) single crystal (Mateck, 99.999%, < 0.4° polishing) was cleaned by multiple cycles of sputtering in 10^{-5} Torr Ar at 1.5 kV and subsequently annealed to 700 K. Low energy electron diffraction (LEED) images showed good sample quality with (1x1) crystal structure. STM of the Ag(100) showed consistent large flat terraces (Figure 4.1). The thin films were created using molecular beam epitaxy wherein the evaporated metal atoms were deposited onto the silver target in the presence of oxygen gas. MnO thin films were prepared by e-beam evaporation (Mantis Deposition LTD, QUAD-EV-C Mini) at a rate of ~ 1 ML min^{-1} monitored using a quartz crystal microbalance (Inficon, Qpod). The MnO films were deposited from a Mn rod (Goodfellow, 99.99%) in 10^{-7} Torr O_2 with the Ag(100) substrate held at room temperature, followed by annealing in vacuum to 800 K [197]. NiO has a 2 % lattice mismatch with Ag(100)[223] and forms high quality (1x1) films on Ag(100) depending on the $\text{O}_2(\text{g})$ pressure (or dosage) and substrate temperature [224-231]. In a separate experiment NiO thin films were deposited by e-beam evaporation (Mantis Deposition LTD, QUAD-EV-C Mini) from a Ni rod (ESPI, 99.995%) in 10^{-6} Torr O_2 at a rate of ~ 1 ML min^{-1} monitored using a quartz crystal microbalance (Inficon, Qpod). The sample substrate was held at room temperature during deposition, followed by annealing in 10^{-6} Torr O_2 to 600 K for 10 minutes. Post annealing of NiO above 550 K has been shown to induce a morphology change from (2x1) to (1x1) on Ag(100) [230].

4.3.2 X-ray Photoelectron Spectroscopy (XPS)

X-ray photoelectron spectroscopy (XPS) spectra were collected in the preparation chamber with base pressures $<2 \times 10^{-9}$ Torr using a hemispherical electron energy analyzer (SPECS, PHOIBOS 100) and twin anode X-ray source (SPECS, XR50). Al K_{α} (1486.6 eV) radiation was used at 10 kV and 30 mA. The angle between the analyzer and X-ray source is 45° and photoelectrons were collected along the sample surface normal. Ag 3d, C 1s, Mn 2p and O 1s spectra were collected using 20 eV pass energy for the MnO samples. For the NiO samples Ag 3d, O 1s, Ni 2p and C 1s spectra were collected using 20 eV pass energy. All spectra were internally calibrated to Ag 3d(5/2) at 368.3 eV [71]. XPS peaks were analyzed using peak fitting software (CasaXPS, v2.3.17) with a Shirley background and Gaussian (80%) Lorentzian (20%) peak fits.

4.3.3 Scanning Tunneling Microscopy (STM)

Scanning tunneling microscopy (STM) is based on the concept of quantum tunneling of electrons between a tip and surface. When a conducting tip is brought very close to the surface to be examined and a bias voltage is applied between the two then there exists a probability of electrons to tunnel through the vacuum between them. The resulting tunneling current is a function of tip position, bias voltage, and the local density of states of the sample and reveals extremely high-resolution information on the samples topology and morphology at the atomic scale. STM experiments (RHK, VT-STM/AFM) were performed at room temperature with images captured under pressures of $< 3 \times 10^{-10}$ Torr. STM tips were composed of tungsten that were electrochemically etched in a 0.10 M KOH solution and then sputtered *in-vacuo*. STM images were acquired under constant current mode with home-built electronics and

GXSM software. STM images were processed using ImageJ software [232]. Investigations did not prove valuable to assess changes in the film morphology after water exposures partly due to the lack of atomic resolution for this STM setup and susceptibility of the STM tip to interact and “pick up” an adsorbate. Thus, the focus of STM measurements herein were on characterizing the morphology of the initial metal oxide film deposition.

4.3.4 Low Energy Electron Diffraction (LEED)

Low-Energy electron diffraction (LEED) is a technique that is used for determination of the surface structure of well-ordered single-crystalline materials by the observation of diffraction patterns resulting from the bombardment of the surface with a collimated beam of low energy electrons, typically between 20 and 200 eV. The diffraction pattern appears as an array of spots in reciprocal k-space in relation to the lattice arrangement of atoms at the samples surface. The diffraction pattern was detected on a phosphorous screen held at a high positive bias and captured with a commercial camera. LEED images (Specs, ErLEED 150) were captured at room temperature in the preparation chamber.

4.3.5 *In-Situ* Water Exposures

Water vapor exposures were performed in the fast entry chamber equipped with a precision leak valve, behind which was attached a custom glass bulb containing 18.2 M Ω water (Aqua Solutions, 2122A). Prior to water vapor exposure, the fast entry chamber was baked and maintained a base pressure of $< 2 \times 10^{-8}$ Torr and the water was freeze-degassed at least three times. After exposure to water vapor, the load lock

chamber was pumped down and the sample was transferred for XPS analysis under UHV.

4.4 Results and Discussion

4.4.1 Manganese Oxide Ultra-Thin Films on Ag(100)

4.4.1.1 Thin Film Deposition Characterization

The sputter and annealed silver single crystal were initially characterized by XPS, LEED, and STM. Each film was deposited onto a freshly cleaned silver surface which was characterized by XPS to ensure that the surface was free of metal and oxygen signals and with minimal carbon contaminations. STM of the annealed Ag(100) showed consistent large flat terraces (**Figure 4.1**) indicative of a clean well-ordered single crystal surface. LEED images of the Ag(100) (**Figure 4.2a**) displayed good sample quality with (1x1) lattice crystal structure.

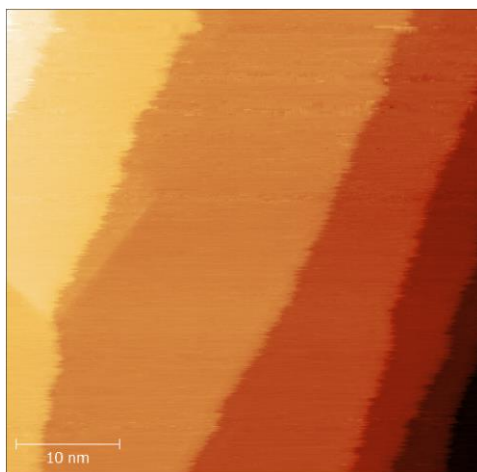


Figure 4.1: STM of cleaned silver, sputtered and annealed at 700K. 50x50 nm images collected at 0.96 V and 0.53 nA. Reproduced with permission from [221].

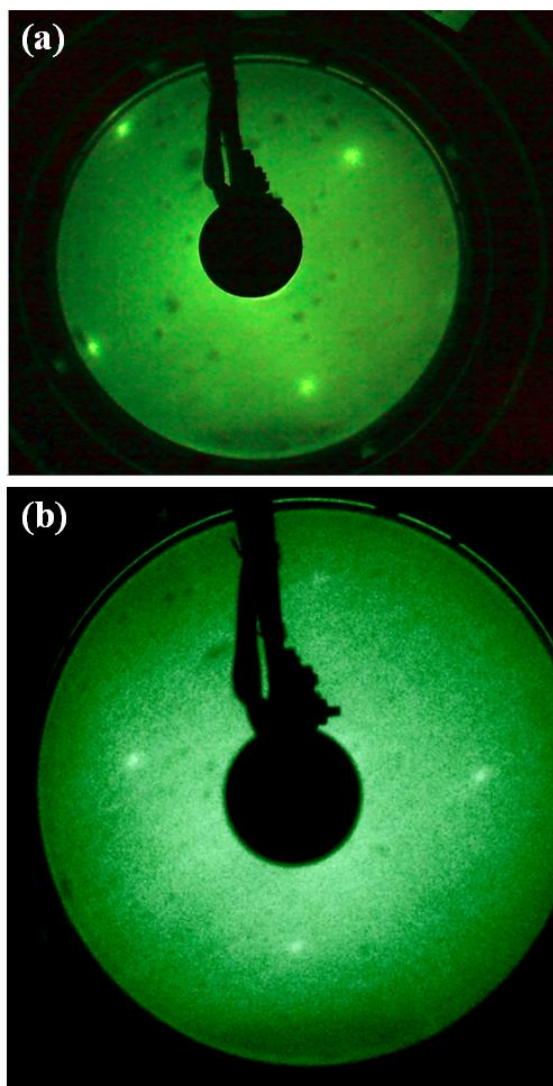


Figure 4.2: LEED images of (a) clean Ag(100) and (b) MnO film annealed to 700 K in vacuum. Images taken at 86 eV. Reproduced with permission from [221].

After preparation of MnO ultra-films on Ag(100) the sample was characterized by XPS, STM, and LEED. Results of a freshly prepared MnO/Ag(100) film are shown in **Figure 4.3**. Most of the silver substrate is covered with an extended single layer of MnO with intermittent square islands forming on top. The cubic nature of the of the

islands within the images was indicative of a (1x1) MnO structure on Ag(100), further evidenced by LEED results (**Figure 4.2b**). Three representative line scans are shown in **Figure 4.3b**. Trace 2 (black) tracks a line profile from the edge of one extended monolayer (ML) film to another, with the Ag(100) substrate in between. The apparent height in this first layer is ~0.2 nm. Trace 1 (red) shows the profile of an island on top of the extended MnO monolayer film. The apparent height of this island is similar to that of the extended MnO monolayer film (trace 2). This suggests the isolated islands are a second layer of MnO on top of the extended underlying MnO. Dark STM features are also seen in the interior of the extended MnO monolayer film with apparent heights of ~0.8 nm (trace 3). Given the lack of atomic resolution for this instrument, it is difficult to assess the nature of these dark spots although they may be due to small holes vacancies in the extended MnO film. Such dark features were not observed previously for a (2x1) MnO/Ag(100) film [195]. Based on the image in **Figure 4.3a** it can be estimated that the MnO coverage was 0.9 ML.

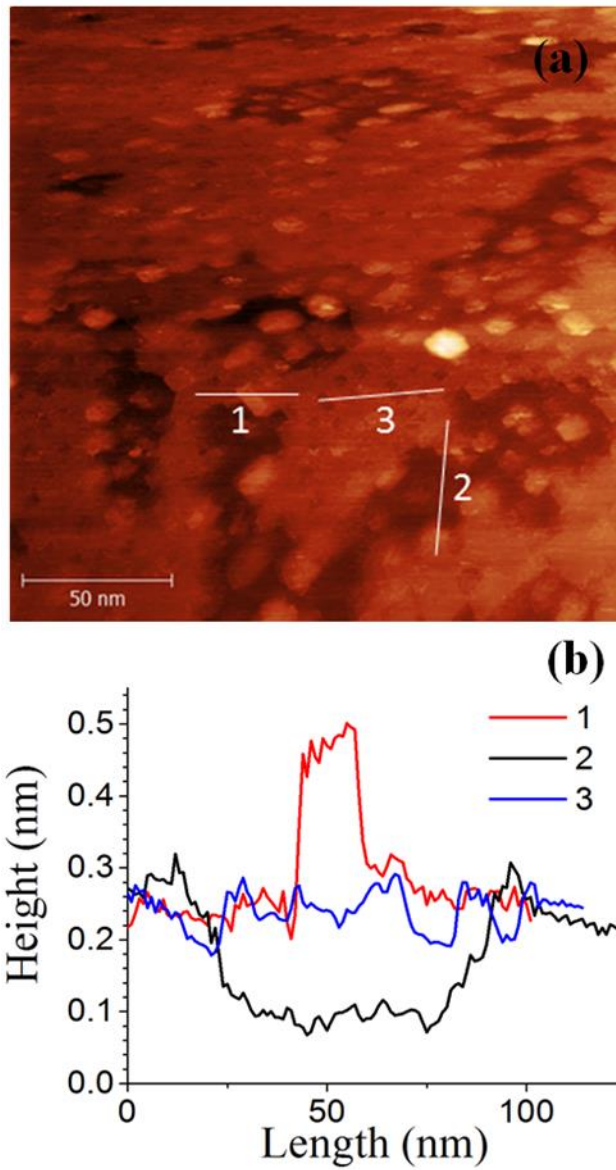


Figure 4.3: STM results of a freshly prepared MnO film annealed in vacuum to 800 K. (a) 200 x 200 nm image collected at -2.0 V and 0.40 nA. (b) Apparent height profiles of line traces within STM image. Reproduced with permission from [221].

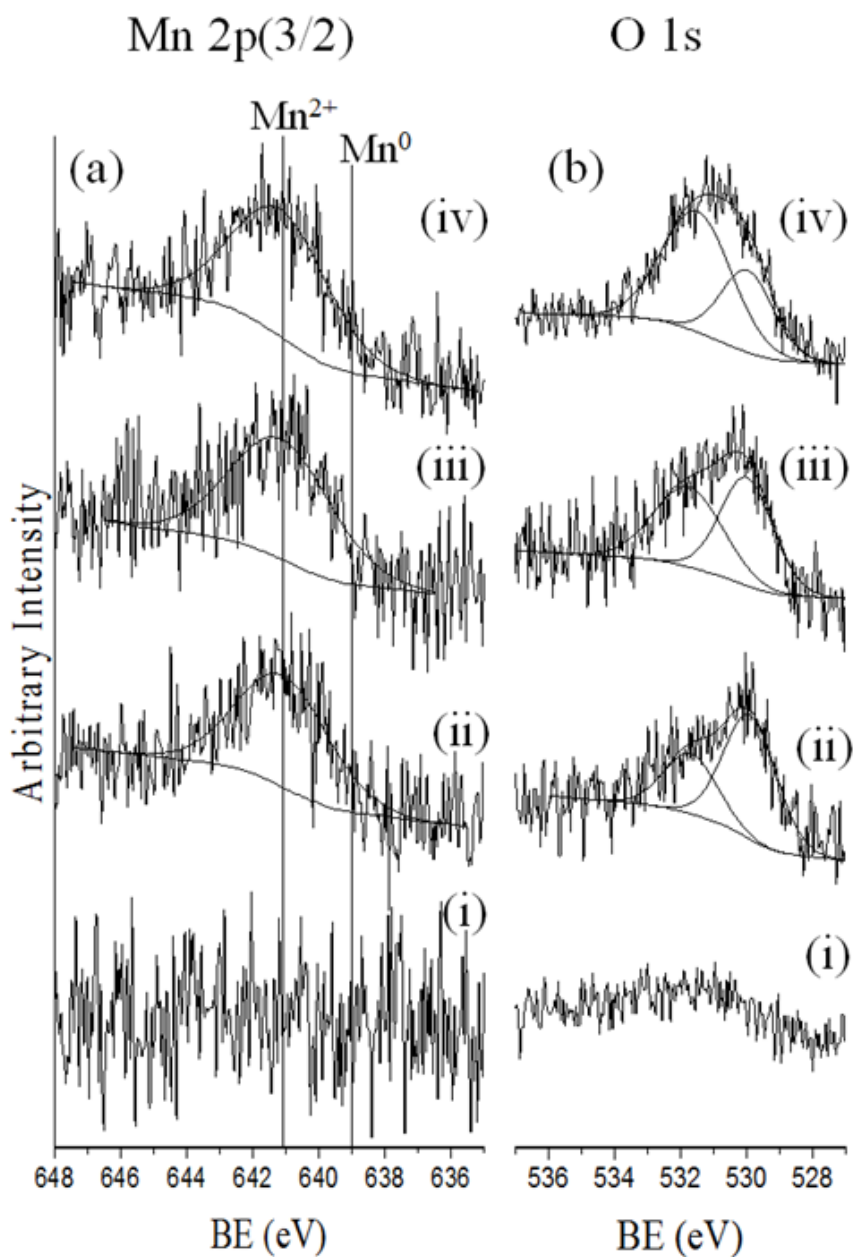


Figure 4.4: XPS spectra of MnO/Ag(100) film at different experimental conditions (a) Mn 2p(3/2) and (b) O 1s XPS spectra taken of (i) silver substrate, (ii) as deposited film of MnO, (iii) after 5-minute exposure to 9.0×10^{-3} Torr H₂O and (iv) after exposure to 2.5 Torr H₂O. Reproduced with permission from [221].

Spectroscopic characterizations of the MnO/Ag(100) film are presented by Mn 2p(3/2) and O 1s XPS spectra (**Figure 4.4**). The initial Ag(100) substrate is devoid of Mn and O species (**Figure 4.4(i)**), although there some adventitious carbon is present (SI, Figure S4a). The freshly prepared MnO film has an Mn 2p(3/2) binding energy (BE) of 641.1 eV (**Figure 4.4a(i)**), consistent with Mn²⁺ for both bulk MnO and metal supported MnO films [193,197,233,234]. These results confirm the complete conversion of Mn⁰ (BE = 639 eV) to MnO during deposition where the O₂ pressure was held at 10⁻⁷ Torr to maintain an Mn²⁺ oxidation state without further converting the film to higher Mn oxidation states. The O 1s spectra of the freshly prepared film (**Figure 4.4b(ii)**) shows a main feature at a BE of 529.9 eV due to the oxide (Ox) peak of MnO, and a smaller peak at a higher BE of 531.6 eV attributed to hydroxyl (OH) groups. The BE difference of 1.7 eV is consistent with the spacing between Ox and OH for the surface of a MnO single crystal [235]. We attribute this initial hydroxyl feature to the dissociation of residual gas phase water background at low coordinated defect sites of kinks, edges, and vacancies on the freshly prepared MnO film. The potential contribution of OH species from oxidized adventitious carbon was found to be negligible based on C 1s spectra composed primarily of C-H species at 285.0 eV (**Figure 4.5**).

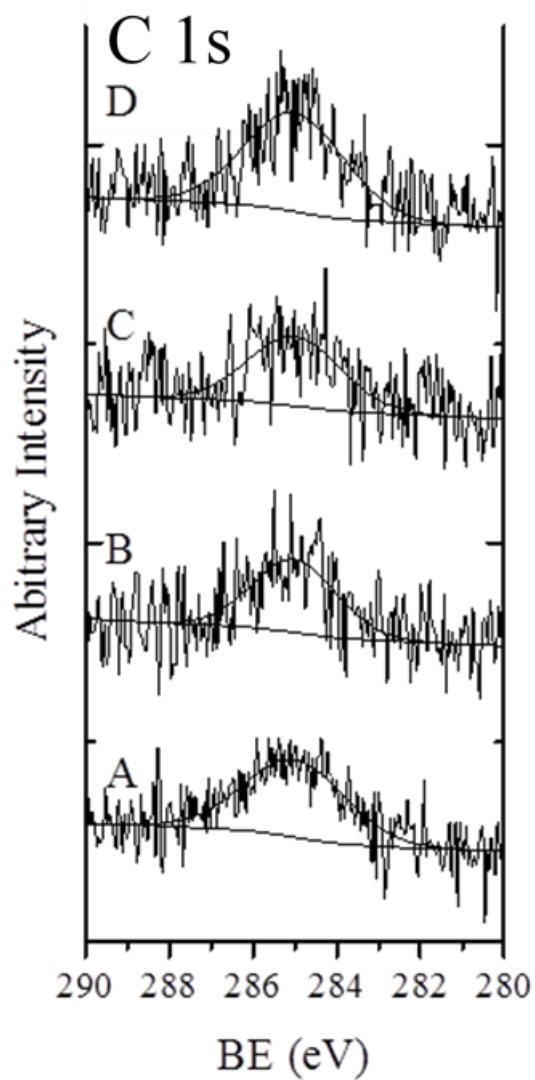


Figure 4.5: XPS C1s spectra of (a) silver substrate, (b) as deposited MnO film, (c) after exposure to 9.0×10^{-3} Torr H₂O for 5min and (d) after exposure to 2.5 Torr water vapor for 5 min. Reproduced with permission from [221].

4.4.1.2 Spectral Analysis of *In-Situ* Water Exposures

Upon exposing the freshly prepared MnO film to a water vapor pressure of 9×10^{-3} Torr for 5 minutes, the Mn 2p(3/2) remains similar to the freshly prepared film (**Figure 4.4a(iii)**) while the O 1s high binding energy OH feature increases relative to the Ox peak (**Figure 4.4b(iii)**). These results indicate that the oxidation state of Mn remains the same (Mn^{2+}) while there was an increase in water dissociation forming hydroxyl groups. The decrease in bulk oxide signal at 529.9 eV is attributed to the conversion of surface Ox species to surface OH. A similar phenomenon was reported for MgO/Ag(100) films exposed to water vapor [236,237]. Water vapor exposures to an MnO(100) single crystal showed that above a pressure “threshold” of 10^{-4} Torr at room temperature the MnO surface significantly hydroxylates [235]. Thus, our results of increased hydroxylation at an exposure of 9×10^{-3} Torr at room temperature are consistent with these observations. The MnO film was additionally exposed to 2.5 Torr for five minutes. The Mn 2p(3/2) peak (**Figure 4.4a(iv)**) remained similar to the first water exposure. The Ox peak decreased while the OH peak increased in the O 1s spectrum (**Figure 4.4b(iv)**) relative to the 9×10^{-3} Torr exposure. **Figure 4.6** plots the OH peak area relative to the total O 1s peak area for the freshly deposited MnO film, 9×10^{-3} Torr exposure and 2.5 Torr exposure. These results show that the surface OH species increases from 29 % under vacuum conditions to 66 % after exposure to 2.5 Torr (12 % RH). The experimental deposition herein prepared an MnO(1x1)/Ag(100) film evidenced both by STM and LEED. This contrasts with Obermüller et al. who observed a metastable (2x1) phase [195]. This difference in phase appears to be due to differences in annealing procedures. Our films were prepared by depositing Mn in an O_2 environment at room temperature followed by annealing under vacuum to 800 K. However, films produced by Obermüller et al. [195] were annealed in 7×10^{-8} to $4 \times$

10^{-6} Torr O_2 at 700 to 800 K. Annealing under O_2 may be responsible for the kinetically driven transition to the metastable (2x1) phase. Muller et al. quantitatively characterized thin MnO films and found well-ordered films with structure approaching bulk lattice constants after annealing to 300K and 500K [197].

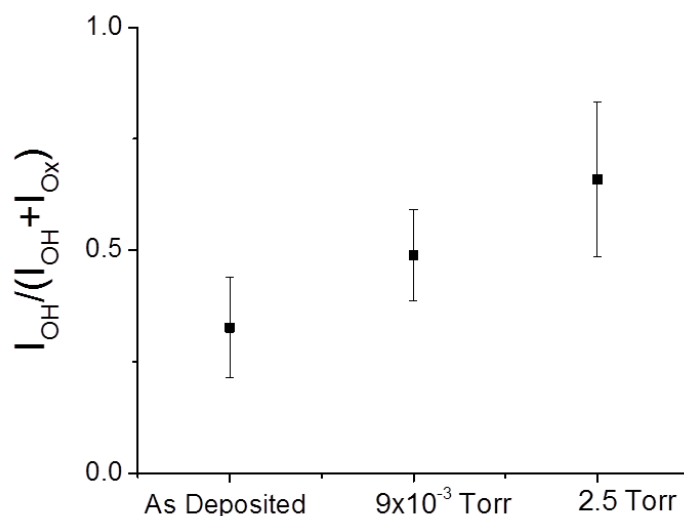


Figure 4.6: Ratio of XPS OH to Ox peak intensities for the initial MnO film, after exposure to 9.0×10^{-3} Torr H_2O , and after exposure to 2.5 Torr H_2O . Water exposures were 5 min. Reproduced with permission from [221].

The freshly prepared MnO(1x1)/Ag(100) film was observed to be partially hydroxylated under vacuum conditions (**Figure 4.4b(ii)**). We attribute this to the reactivity of residual water vapor in the chamber with MnO film nonstoichiometric defect sites (steps, kinks, corners, and sites with missing Mn and O). This is consistent with the interpretation of Brown and coworkers [235] who exposed a freshly prepared

MnO(100) single crystal surface to varying water vapor pressures. Below 10^{-4} Torr hydroxylation was slow but was observed to increase over a period of an hour. Exposures to MnO above a “threshold” pressure of 10^{-4} Torr lead to extensive and rapid hydroxylation of the surface. A similar “threshold” pressure was observed by Brown and coworkers [238] for water vapor exposures to a MgO(100) single crystal and attributed the similar reactivity of MnO(100) and MgO(100) above this threshold to extensive dissociation of water at stoichiometric terrace sites on both surfaces.

In their extensive discussion comparing water reactivity with MnO(100) and MgO(100), Brown and coworkers identified a stark contrast between the two below the “threshold” pressure. At low water vapor pressures, MnO(100) hydroxylation was observed to increase as a function of time, while MgO(100) did not. Brown and coworkers remarked that the “reason for this difference is unclear at present and requires further investigation” [235]. It has been shown experimentally that extensive hydroxylation of MgO(100)/Ag(100) films occurs under ambient water vapor conditions above a threshold relative humidity of 0.01 % using ambient pressure XPS. These results were consistent with the vacuum studies of Brown and coworkers for single crystal MgO(100) [238]. It was suggested by Newberg et al. [236] that the onset to hydroxylation was likely due to an autocatalytic dissociation process whereby water aggregation at stoichiometric terrace sites occurs, transitioning from water monomers on the surface to water dimers or trimers. Shortly thereafter Giordano and Ferrari [239] showed that while water monomers are unreactive at MgO(100) terrace sites, upon forming a water dimer one of the two waters within the dimer goes through barrierless dissociation. Thus, upon forming a water dimer at MgO terrace sites, one of the waters is dissociated into two hydroxyl groups while the other remains molecular,

stabilizing the hydroxyl groups. This behavior was found to occur for monolayer MgO(100)/Ag(100) and bulk MgO(100).

Through the DFT computational work of our collaborators Giordano and Ferrari in the work of Arble et al. [221] for the case of MnO(1x1)/Ag(100), it was calculated to be energetically favorable to have a water monomer in both the molecular and dissociated state. For MgO(100) the dissociated state is energetically unfavorable. Moreover, there is an energy barrier of ~ 0.35 eV in transitioning from the molecular to dissociated state. We believe it is this transition state which leads to the time dependent reactivity of MnO(100) observed by Brown and coworkers [235] under low water vapor conditions ($< 10^{-4}$ Torr). Moreover, the lack of hydroxylation at MgO(100) terrace sites $< 10^{-4}$ Torr is due to the inability of MgO(100) terrace sites to dissociate water monomers. **Figure 4.4** and **4.6** indicate that the hydroxyl growth follows the behavior of water monomers dissociating in the 9.00×10^{-3} Torr regime and then further growth in the regime of water dimers at 2.5 Torr.

4.4.2 Nickel Oxide Ultra-Thin Films on Ag(100)

4.4.2.1 Thin Film Deposition Characterization

After preparation of NiO ultra-films on Ag(100) the sample was characterized by XPS, STM, and LEED. NiO films were deposited onto annealed Ag(100) which showed consistent large planar terraces (**Figure 4.1**) indicative of flat single crystal surface. LEED images of the Ag(100) (**Figure 4.2a**) displayed good sample quality with (1x1) lattice crystal structure. An STM image of a freshly prepared NiO/Ag(100) film collected at a positive bias of +2.5 V and had an estimated coverage of 0.5 ML (**Figure 4.7a**). The surface is composed of square and rectangular islands (dark) on the

Ag(100) substrate (bright background) which extend laterally ranging in size from about 5 to 20 nm. The imaging of dark NiO islands on Ag(100) is consistent with previous STM studies at low positive bias [226,240]. A plot of tunneling current versus bias shows that the electronic states of the NiO are accessed at ~ 3 V and above [226]. Thus, the dark images for the islands stem from a lowering of the tunneling current relative to the metallic Ag(100) substrate. This decrease in tunneling current gives rise to a dip in line traces across the NiO islands (**Figure 4.7b**) which give an apparent height of ~ 0.2 nm. In addition to isolated islands, there are regions of extended NiO films across the surface that are several 10's of nm across (see upper right corner of **Figure 4.7a**). The cubic nature of the NiO islands is indicative of a (1 \times 1) structure on Ag(100), confirming that our post annealing procedure produces NiO(1 \times 1) structures [230]. The islands growth edges extended out rectangularly in [110] and [1-10] principal crystallographic directions of the silver substrate [230]. This (1 x 1) phase was further evidenced by performing LEED on a freshly prepared film which displayed (1 \times 1) diffraction pattern (**Figure 4.8**).

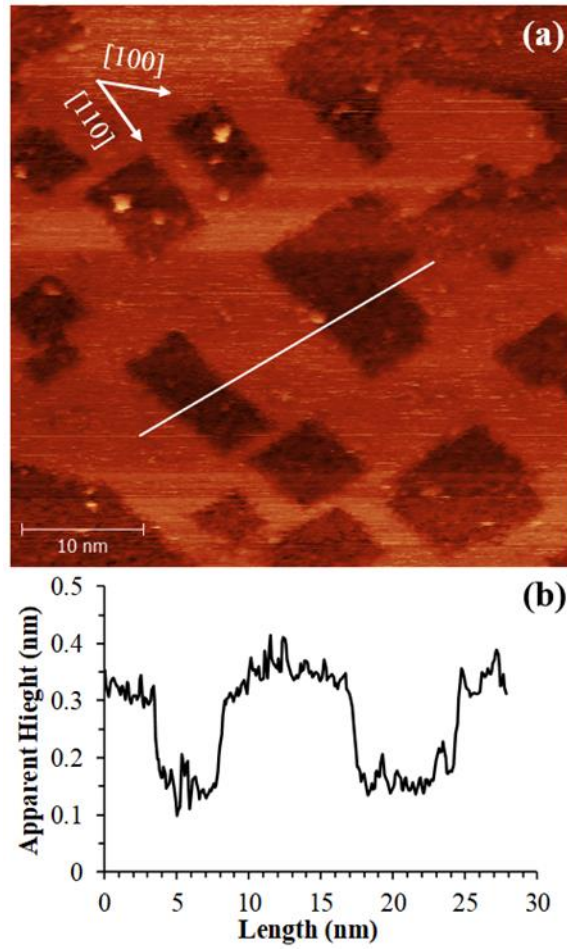


Figure 4.7: (a) STM image of NiO film collected at +2.5V and 0.5 nA. The principal crystallographic directions are indicated. (b) Topological plot of white line in (a). Reproduced with permission from [222].



Figure 4.8: LEED image of an annealed NiO(100) film collected at 88 eV. Reproduced with permission from [222].

During NiO film deposition the oxygen pressure was chosen to be held at 1×10^{-6} Torr in order to maintain a Ni^{2+} oxidation state. XPS spectrum in the Ni 2p(3/2) region for a freshly prepared film (**Figure 4.9a**) were composed of three different components consistent with the formation of NiO [71,241] where the lowest binding energy (BE) peak observed at 853.8 eV is attributed to Ni^{2+} . The two additional peaks at 856.1 eV and 861.0 eV are consistent with NiO formation, but the origin of these peaks have been attributed to a number of effects that are still debated, including non-local screening effects, defect driven states, multi-electron charge transfer excitation processes and unscreened final state effects [241-245].

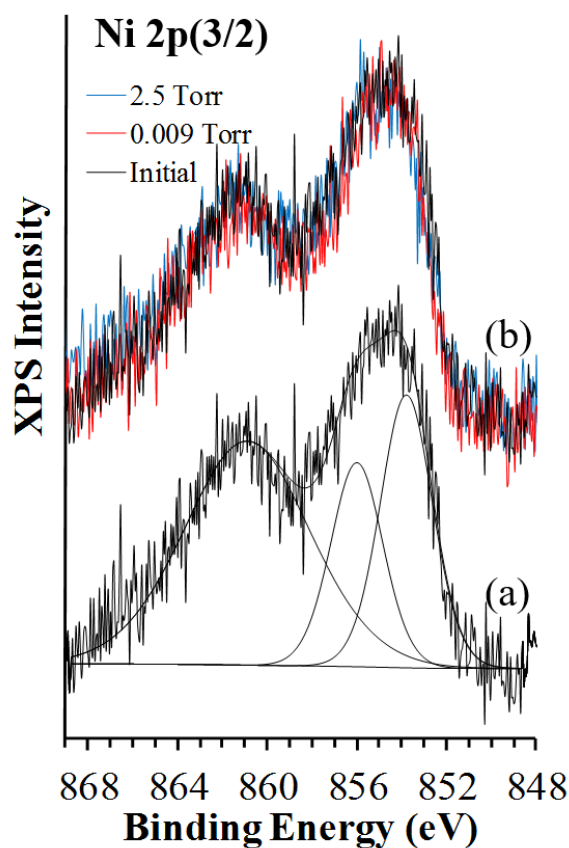


Figure 4.9: Ni 2p(3/2) spectra of NiO (a) initial film. (b) An overlay of three spectra, the initial film (black) and after 0.009 Torr (red) and 2.5 Torr (blue) water vapor exposures. Reproduced with permission from [222].

The O 1s spectrum of the freshly prepared film (**Figure 4.10a**) shows a main feature at a BE of 529.6 eV due to the oxide (Ox) O^{2-} peak of NiO, and a smaller peak at a BE of 531.1 eV attributed to hydroxyl (OH) groups. A similar observation was observed previously for NiO/Ag(100) films, with the OH peak attributed to interaction of background water vapor with reactive edge sites [246]. The potential contribution of OH species from oxidized adventitious carbon was found to be negligible on the initial NiO film based on C 1s results showing primarily of C-H species at 284.8 eV

(**Figure 4.12**, black spectrum). We therefore attribute the formation of OH species on the freshly prepared film to dissociation of background residual water in the vacuum chamber with highly reactive nonstoichiometric defects including edge and corner sites on the NiO islands.

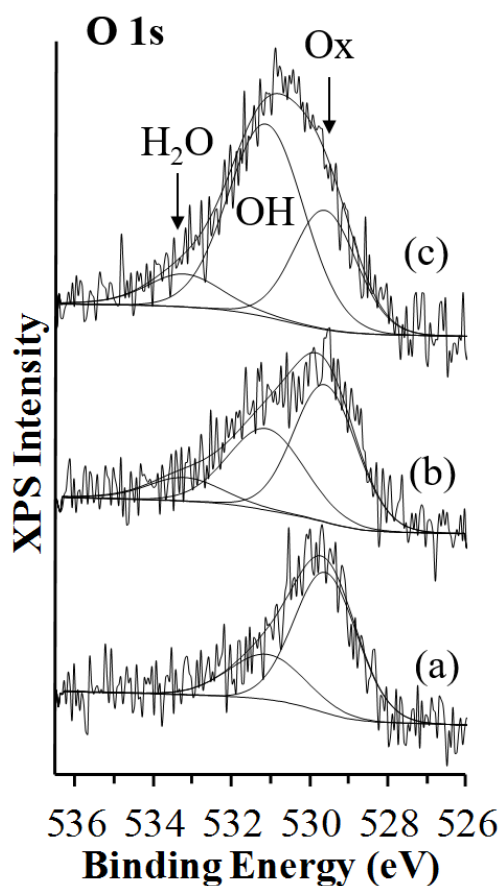


Figure 4.10: O 1s spectra of NiO (a) initial film, (b) after exposure to 0.009 Torr and (c) 2.5 Torr water vapor. Each exposure was for 15 min. Reproduced with permission from [222].

4.4.2.2 Spectral Analysis of *In-Situ* Water Exposures

After preparation of NiO ultra-films on Ag(100) the sample was characterized by XPS, STM, and LEED. In the subsequent experimental step, the NiO film was exposed to two separate water vapor pressures with XPS taken after each exposure. The first water vapor exposure was for 15 min. at a pressure of 0.009 Torr, corresponding to 0.04 % relative humidity (RH) at 25 °C. The RH was chosen to be below the critical onset humidity of 0.01 % RH, which has been shown for previous XPS studies on other metal oxide surfaces that above 0.01 % RH the surface experiences significant hydroxylation events [55-58]. As seen from **Figure 4.10b**, upon exposure to 0.04 % RH there is an increase in the OH peak and evidence of a small third peak that shows up at 3.6 eV higher BE from the Ox peak which is attributed to molecularly bound water. The next water exposure was intentionally dosed above the critical onset humidity at 2.5 Torr corresponding to 10 % RH for 15 min and led to a significant increase in the OH peak, a decrease in the Ox peak, while the molecularly bound water peak remains essentially constant.

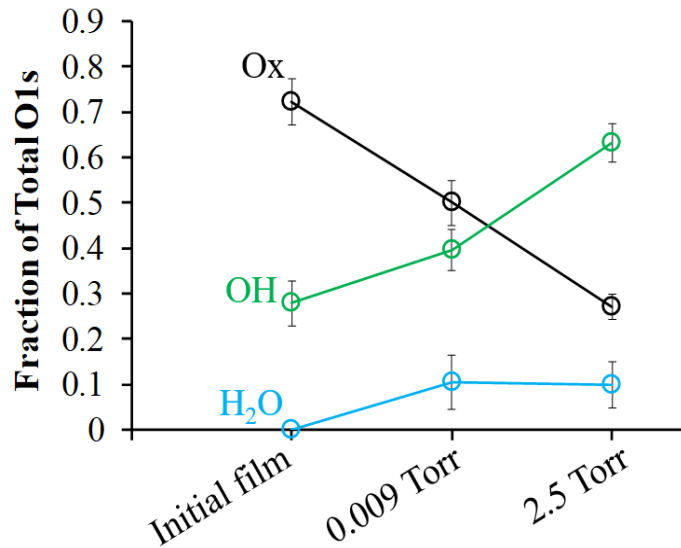


Figure 4.11: Ratio of the oxide (Ox), hydroxyl (OH) and molecularly bound water (H₂O) peak to the total O 1s peak area as a function of sample condition. Water vapor exposures were 15 min. Reproduced with permission from [222].

Figure 4.11 shows a quantitative assessment of the O 1s peak areas, taking the ratio of each of the three peaks to the total O 1s spectrum. Error bars are calculated from the individual errors associated with each peak fit generated from Casa XPS and propagated through the ratio calculation. The relative intensity of the OH peak goes from 0.28 up to 0.63 in going from the initial film to the 10 % RH exposed film. At the same time the relative Ox peak decreases from 0.72 to 0.27. This decrease in Ox intensity is due to the conversion of the oxide sites to hydroxyl sites at the interface. The significant increase in hydroxylation in going from 0.04 % to 10 % RH is consistent with previous XPS observations on other metal oxides [236,247-249]. Moreover, a 63 % OH peak area cannot be accounted for by dissociation solely at the edges of the NiO(1x1) islands in **Figure 4.7a** suggesting that the observed extensive

hydroxylation is occurring at terraces. XPS intensities of the OH and Ox species suggests that the film is 28 % hydroxylated after the 0.04 % RH exposure and 53 % hydroxylated after the 10 % RH exposure, assuming Ni(OH)₂ was formed.

The Ni 2p(3/2) spectral envelope remained largely unchanged upon exposure to water as seen from the overlaid spectra (**Figure 4.9b**), suggesting that the oxidation state of Ni remains Ni²⁺ upon NiO hydroxylation. Peaks associated with the Ni(OH)₂ species were attempted to fit in the Ni 2p(3/2) spectra, however the BEs associated with this components of the Ni(OH)₂ species closely overlaps with the satellite feature of NiO, 857.7 eV and 857.4 eV respectively [250]. Unfortunately, such fittings were inconsistent and unreliable given the low signal to noise ratio of the spectra. As such, the fittings were excluded from the figure. The absence of significant changes in the metal peak upon hydroxylation is not surprising and is dependent on the metal oxide being examined. For example, Fe 2p spectra are not very sensitive to hydroxylation of Fe₂O₃ in the presence of water vapor [251], whereas Mg 2p in MgO shows some evidence of peak broadening upon hydroxylation [247]. Moreover, the water vapor exposures did not lead to any change in the carbon spectra (**Figure 4.12**). Thus, the observed increase in hydroxylation can be attributed to water adsorption.

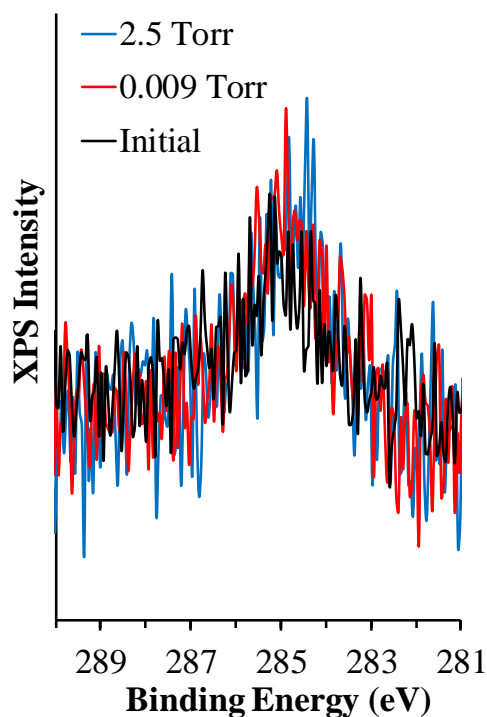


Figure 4.12: C 1s spectra of initial NiO film (black) and after water vapor exposures to 0.009 Torr (red) and 2.5 Torr (blue). Reproduced with permission from [222].

Yang et al. [215] grew a 4 ML NiO/Ag(100) with a background water vapor pressure of $\sim 1 \times 10^{-9}$ Torr at 110 K and observed three peaks in the O 1s region due to Ox, OH and molecularly bound water in the form of ice at this temperature. However, NiO/Ag(100) grown at room temperature in the same background water vapor pressure only showed two peaks (Ox and OH) similar to our spectra in Figure 3a, and no molecularly bound water. This suggests that the higher pressures used in our study lead to extensive hydroxylation and residual adsorbed water. This is likely due to strong H₂O-OH hydrogen bonding interactions that still reside under vacuum. The

existence of molecularly bound water under vacuum at room temperature is not surprising. For example, Altieri et al. [252] observed molecularly bound water on hydroxylated MgO/Ag(100) monolayer films under vacuum conditions after exposures to water vapor. These experimental results indicate that NiO monolayer films extensively hydroxylate upon exposure to near ambient water vapor pressures, while lower pressures only react at edge sites [215]. We attribute this increase in reactivity to water dissociation at terrace sites on top of the Ag(100) supported NiO film. While the XPS studies herein cannot distinguish between OH species at terrace sites versus defect sites, a peak area of 63 % for OH relative to the total O 1s peak can only be accounted for by reactions occurring at both defect sites and terraces.

DFT results provided by our collaborators, Giordano and Ferrari within Arble et al. [222], revealed that the water monomer has a stable dissociated form on Ag-supported NiO monolayer, although it is less energetically favorable compared to the molecular form. Additionally, the presence of an energy barrier to dissociation would favor the molecular form over the dissociated one. For example, a water monomer on an Ag-supported MgO monolayer has an energy barrier been estimated to exceed 0.5 eV [253]. A less energetically stable dissociate state for a water monomer is consistent with XPS results within this study and previous XPS experiments [215] which show minor hydroxylation when exposed to background water vapor pressures at room temperature. This becomes a justification for former XPS, TPD and LEED studies under low pressure water vapor exposures which reported that dissociation occurs only at defects and not at terraces [209-215]. Upon exposure to higher RH's, water aggregation occurs at terrace sites. The DFT results showed that when two monomers meet on the surface they form a hydrogen bound aggregate that easily dissociates

leading to a more stable product. These theoretical results are fully consistent with observations of increased hydroxylation at higher RH exposures observed by XPS.

4.5 Conclusions

This Chapter examined the hydroxylation of MnO(1x1)/Ag(100) and NiO(1x1)/Ag(100) with a combination of experimental techniques. The formation of (1x1) MnO on Ag(100), which is energetically more favorable than the (2x1), was prepared by evaporation of Mn onto Ag(100) at room temperature in the presence of 10^{-7} Torr O₂, followed by annealing in vacuum to 800 K. Annealing in the presence of O₂ has been shown to form metastable (2x1) MnO [195]. Upon exposure to water vapor, extensive hydroxylation of MnO(1x1)/Ag(100) occurs, consistent with previous results for an MnO(100) single crystal. The molecular simulations revealed that it is energetically favorable to go from the molecular to dissociated state of a water monomer on MnO(1x1)/Ag(100) terrace sites with an energy barrier of ~0.35 eV. This is in stark contrast to MgO(100)/Ag(100), where it is energetically unfavorable for a water monomer to dissociate at terrace sites. We believe the observations of an energy barrier for the dissociation of a water monomer on MnO(1x1)/Ag(100) helps elucidate previously unresolved observations of time dependent hydroxylation kinetics for the dissociation of water on MnO(100).

The interaction of water vapor with NiO(1x1)/Ag(100) islands was also assessed using vacuum-based XPS. Previous studies examining the interaction of water with NiO(100) suggested that dissociation does not occur at terrace sites when exposed to water vapor pressures in the high vacuum regime. Upon exposure to high water vapor pressures (maximum 2.5 Torr) at room temperature, we show that extensive hydroxylation is observed on Ag(100) supported NiO(1x1) islands. The

extent of the OH intensity was attributed to the dissociation of water at stoichiometric terrace sites upon aggregation. This interpretation was supported by DFT calculations performed by collaborators, examining the interaction of a water monomer and dimers with an Ag(100) supported NiO(1x1) film. Results indicate that the molecular form of a water monomer is more stable than that of the dissociated form. However, upon aggregation of two molecularly bound water molecules the hydrogen bounded water dimer can easily dissociate by crossing a small energy barrier, leading to a dissociated state that is more stable than the molecular dimer. This stability is mainly attributed to the H₂O-OH hydrogen bond formation and to a minor extent the structural distortion of the Ag(100) supported NiO(1x1) film. These results are consistent with the observations of extensive hydroxylation at higher RH exposures where aggregation is expected to occur.

Chapter 5

INVESTIGATION OF PHOTOCATALYTIC PROCESSES ON MANGANESE OXIDES

5.1 Abstract

Heterogeneous interactions on metal oxides are critical processes for many industrial and biological applications, particularly that of photo chemical processes. The semiconductor properties of many transition metal oxides allow the adsorption of light to promote an electron from its valance band to the conduction band. These excited electrons can catalyze reactions which lead to the photooxidation and subsequent removal of adsorbates. The interaction of UV and visible solar irradiation alongside of oxygen with a MnO surface was investigated using lab-based ambient pressure X-ray photoelectron spectroscopy (AP-XPS). Experiments were conducted under 0.09 Torr O₂ and with solar simulator light sources with ranges of 280. The combination of UV light and the presence of O₂ which react with photogenerated electrons to form reactive oxygen species were required to observe any chemical change within the core shell spectra. The intensity of the carbonyl species in the C 1s decreased by 50% upon exposure to reaction conditions with corresponding signal losses in the O 1s. Additionally, a MnO₂ film was electrodeposited onto indium tin oxide coated glass for study of photochemical processes on a more reactive surface. The morphology and chemical structure of the electrodeposited were examined with scanning electron microscopy (SEM) and XPS. The photocatalytic nature of the film

was characterized by the degradation of methylene blue from exposure to simulated sunlight.

5.2 Introduction

Photoelectron transfer processes using earth abundant metal oxide semiconductors are promising technologies which can be exploited in solar energy conversion, storage of energy, synthetic material conversion, and for destruction of volatile organic compounds from air pollution [254-256]. Photocatalytic reactions using solar energy can successfully catalyze mild oxidation of alkanes, alkenes, and alcohols on the surfaces of metal oxides or sulfides [257]. Illuminated semiconductors have appropriate chemical potentials to oxidize organic pollutants into benign products such as CO₂ and H₂O which provides a green energy solution to a growing health problem of VOC in urban areas [258]. When the semiconductors adsorb UV light, electrons are excited from the valence band to the conduction band, resulting in valence band electron vacancies. Excited state species have very short lifespans on the order of nanoseconds to picoseconds necessitating the need to carry out simple and fast chemical transformations. Such semiconductors need to have active surface sites that can adsorb reactant species such as the organic pollutant, O₂, and H₂O in order to catalyze such reactions [259].

Manganese is the tenth most abundant element in the Earth's crust and therefore one of the most inexpensive transition metals. Manganese oxides are utilized as electrode materials, catalytic substrates and in many biological and environmental systems [179,184,260,261]. Manganese oxide catalysts are generally known as oxidants due to the presence of active oxygen species (in the lattice or adsorbed on the surface) and are proven active for thermally and photochemically catalyzed reactions.

The literature has reported catalytic activity of synthetic MnO₂ in the selective photooxidation of alcohols to carbonyls,[262,263] and in VOC abatement oxidizing harmful compounds to CO₂ [178,264,265]. Manganese oxides are very common mineral components of soils and are often present in natural photoactive minerals the environment. Manganese oxide can be effectively used as photocatalyst without the need of doping due to d–d electronic transitions from partially filled d-orbitals which occur during irradiation.

Many photochemical reaction studies have focused on aqueous solutions of organics. Surface science techniques have been required to elucidate the mechanisms of photochemical reactions that occur at heterogeneous interfaces. Heterogeneous gas phase catalysis is a particularly simple and environmentally friendly method due to the ease of recovery of the catalyst and reusability. X-ray photoelectron spectroscopy is a powerful tool that can map the chemical states at the very near surface region of materials. Traditionally, XPS operates under ultra-high vacuum which deters the use of gas phase adsorbates, until recent technological developments were made to “bridge the pressure gap” in photoelectron spectroscopy. Current ambient pressure XPS systems are an excellent tool to probe surface under *in-situ* conditions; however very little work has explored photochemistry with the technique. AP-XPS has been used to investigate photochemical processes over substrates of Ta₃N₅ nanotubes [266], TiO₂(110) [267], anatase TiO₂ films [268], TiO₂ powder [104,269] and TiO₂ nanoparticles [270]. Herein an AP-XPS investigation of a heterogeneous reaction on the surface of manganese oxide is reported. The chemical state and the electronic properties of the surface investigated under UV irradiation, water, and oxygen dosage.

X-ray core-level spectroscopy characterization of the oxygen and carbon regions established a photochemical with the residual organic material on the surface.

MnO₂ is an attractive candidate for use in catalysis, electrochemical materials, and as a photoactive agent. Photocatalytic studies have been conducted using amorphous manganese oxide and have attributed much of the reactivity of the material to the MnO₂ species [271-273]. The manganese oxide surface studied within Section 5.4.1 was not fully oxidized to Mn(IV) oxide based on XPS results. Thin films of manganese oxide were electrochemically deposited onto indium tin oxide (ITO) with the goal to produce potentially more reactive MnO₂ thin films. ITO is a transparent n-type semiconductor, with a low electrical resistivity of 2×10^{-4} cm and a wide band gap (from 3.3 eV to 4.3 eV) [274]. ITO is an optoelectronic material that is widely used within both research and industry. ITO coated glass has been widely used as a support in many applications including solar cells, heat-reflecting mirrors, antireflective coatings, and gas sensors [274]. ITO has been used as the substrate in a number of studies to produce manganese oxide films and nanostructured materials. The composition of the deposited films was characterized with XPS and SEM, and their response to light was investigated by monitoring current generated electrochemically as well as the degradation of an indicator dye.

5.3 Experimental Details

5.3.1 Sample Preparation and Analysis

5.3.1.1 Native Manganese Oxide

Manganese polycrystalline solid samples (Sigma Aldrich, 99.99%) were polished using fine grit abrasive pads and 0.5 μm alumina solution. The samples then

washed with ethanol followed by DI water and then dried in the presence of nitrogen prior to the introduction into vacuum chamber for analysis.

5.3.1.2 Electrodeposited Manganese Oxide Film

Indium tin oxide coated glass electrodes (Yingkou Opv Tech New Energy Co. Ltd) (2 cm × 1 cm × 0.1 cm) were stored immersed in deionized distilled water and ultra-sonicated for 30 minutes prior to electrochemical deposition. Cyclic voltammetry (CV) was employed for the electrochemical deposition process with a potentiostat / galvanostat (Biologic, SP-300). The ITO conductive film was placed in a 0.10 M potassium chloride (KCl, Fisher Scientific, 99.8 %) electrolyte solution containing 0.10 M manganese chloride (MnCl₂·4H₂O, Sigma Aldrich, >99 %). The three-electrode setup used included the ITO working electrode, Pt wire counter electrode, and an Ag/AgCl (saturated KCl) reference electrode. CVs were conducted over a 0 to +1.5 V window versus reference at a scan rate of 10 mV/s and the CVs were repeated between 0 and 10 times to adjust the thickness of the film. Synthesized films were then removed from solution and rinsed with deionized distilled water before drying in a vacuum oven overnight.

5.3.2 Ambient Pressure X-ray Photoelectron Spectroscopy (AP-XPS)

The surface chemistry of polished manganese oxide substrate was probed using a lab-based ambient pressure X-ray photoelectron spectrometer (Scienta HIPP-2 R4000) and a monochromatic Al anode X-ray source (Scienta MX650) operating at 20 mA and 10 kV. The details of this system have been described previously in Chapter 2. All spectra were captured using acceleration mode [73] and with an aperture size of 0.5 mm. The analysis chamber base pressure was 1.0×10^{-8} Torr prior to the start of

experiments. Ambient pressure experiments were performed by introducing oxygen gas (Keen, 99.997%) through a precision variable leak valve into the analysis chamber. Mn 2p, Mn 3s, O 1s and C1s spectra were captured at 100 eV pass energy and a step size of 0.16 eV. Spectra were analyzed with 80:20 Gaussian-Lorentzian fits with a Shirley background subtraction using peak fitting software (CASAXPS, 2.3.16). All spectra were referenced to C 1s aliphatic carbon at 285.0 eV.

5.3.3 X-ray Photoelectron Spectroscopy (XPS)

XPS measurements were conducted on electrodeposited films on a UHV instrument (Thermo Fisher, KAlpha+) located in the Surface Analysis Facility of the University of Delaware. Base pressure of the instrument was 1.0×10^{-9} Torr prior of the start of spectral acquisition. Monochromatic Al K-alpha x-rays were used with a spot size of 100 μm and a flood gun was used to limit sample charging. Spectra of the Mn 2p, In 3d, Sn 3d, O 1s and C1s were collected with a pass energy of 20 eV and step size of 0.1 eV. Spectra were analyzed with 80:20 Gaussian-Lorentzian fits with a Shirley background subtraction using peak fitting software (CASAXPS, 2.3.16). All spectra were referenced to C 1s aliphatic carbon at 285.0 eV. Standards were used in the analysis of the Mn 2p peak and were as follows Mn(II) oxide (Sigma-Aldrich, 99.99 %), Mn(III) oxide (Sigma-Aldrich, 99.99 %), and Mn(IV) oxide (Sigma-Aldrich, 99.99 %).

5.3.4 Scanning Electron Microscopy (SEM) and Optical Microscopy

Scanning electron microscopy (SEM) surface morphology images within this Chapter were collected in secondary electron mode (Zeiss Auriga 60 FIB/SEM) with an accelerating energy of 3 keV and a working distance of 5.0 mm. Optical images

were collected with a light microscope (LM Zeiss AXIO Imager.M2), both SEM and light microscopy were performed at the W. M. Keck Center for Advanced Microscopy and Microanalysis at the University of Delaware.

5.3.5 Xenon Light Exposure

Sample illumination was performed in the APXPS analysis chamber using a 300 W Cermax[®] collimating Xe bulb with inline filters. For the experiments herein, a cutoff filter which emitted solar simulated light above 280 nm. The collimated light was then directed through a circulating water filter to reduce the infrared output of the Xe bulb. The collimated light was focused onto a custom fiber optic cable (LEONI Fiber Optics Inc.) housed in 0.25-inch stainless steel tube which was mounted through a vacuum flange on the analysis chamber. The vacuum compatible fiber termination was positioned approximately 1 cm from the sample surface during illumination.

For exposures to the electrodeposited sample occurred outside of vacuum in which case the light source was brought close to the sample (~5 cm) and enclosed in a dark box to prevent any stray light from impacting the observations. The deposited manganese oxide was scraped off the ITO and dissolved in deionized distilled water and sonicated for 2 hours. To this solution 200 μ M of methylene blue was added whose photodegradation was monitored by UV-Vis (B&W TEC Inc, BDS 130).

5.4 Results and Discussion

5.4.1 Native Manganese Oxide Surface and Photocatalytic Behavior

5.4.1.1 Spectral Characterization of Initial Film

The sample was transferred into the vacuum chamber immediately after the cleaning procedures of ethanol and water washes were performed. Given the samples polycrystalline structure and exposure to ambient atmosphere and the cleaning washes it would not be unexpected that the surface of the manganese metal would contain a native oxide film. Indeed, O1s spectra taken of the initial Mn surface contains several peaks indicative of metal oxide species (**Figure 5.1a**). The components of O 1s were found to be at binding energies of 530.1 eV, 531.4 eV, 532.4 eV, and 533.4 eV assigned to be oxide (Ox), hydroxyl (OH), oxygenated carbon species (OC), and adsorbed water (H₂O), respectively [275]. The binding energies of the components agree well with values reported in literature and these components were present on a hydroxylated oxide that has oxygen containing carbon species on its surface. The O 1s XPS spectra (**Figure 5.1**) indicate there is a small amount of adsorbed water on the sample even though the system was in UHV, which is not uncommon to occur for metal oxides [252,275]. The primary species of the O 1s spectra was the oxide component at 530 eV and constituted 65 % of the spectral area in the initial sample. The hydroxyl species composed 19 % of the signal whereas the oxygenated carbon component comprised 12.5 % and the adsorbed water species 3.5 %.

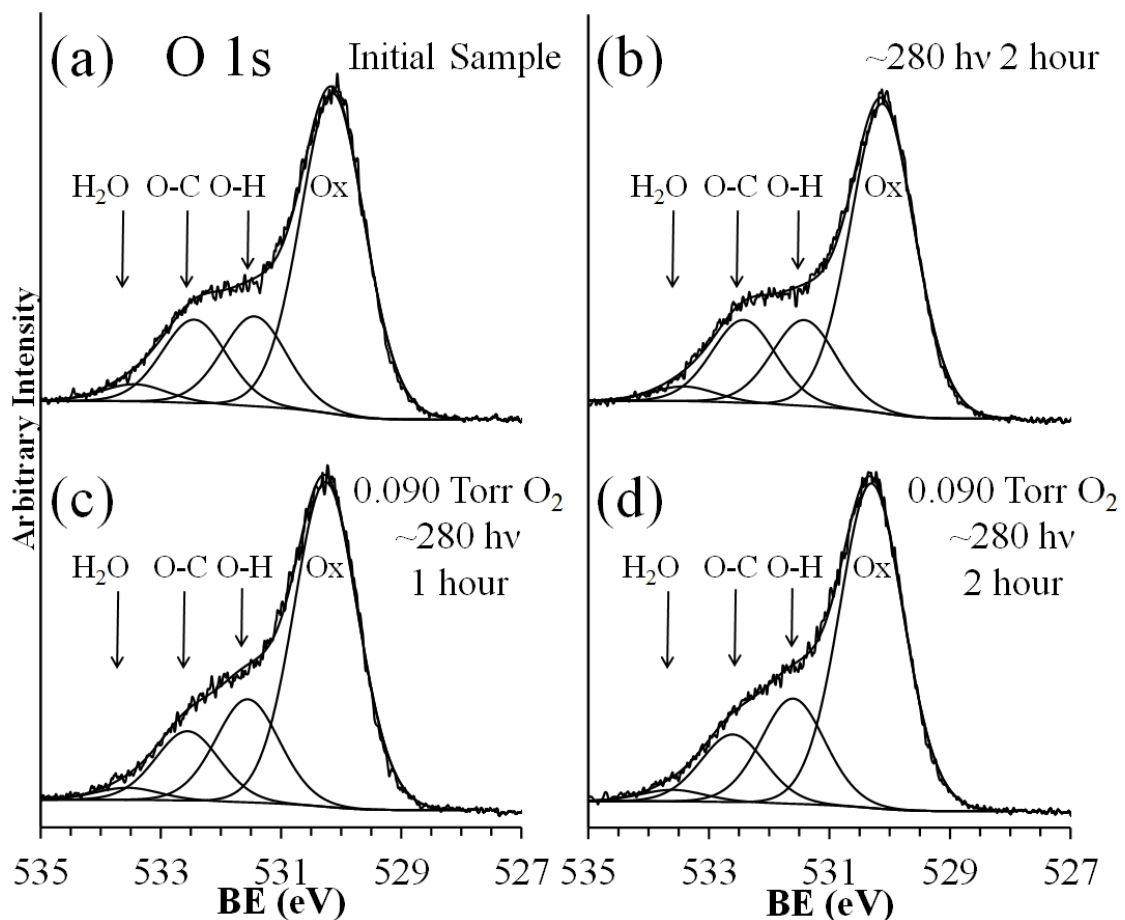


Figure 5.1: Oxygen 1s spectra taken of the (a) initial sample of the native oxide film on Mn, (b) illuminated for 2 hours, (c) under 0.09 Torr O₂ illuminated for 1 hour, and (d) 2 hours. Components fit to the oxide (Ox), hydroxyl (O-H), oxygenated carbon species (O-C), and adsorbed water (H₂O).

Corresponding C 1s spectra of the initial sample are shown in Figure 2 (a). Components were fit at binding energies of 285.0 eV, 286.5 eV, 287.5 eV, and 288.7 eV corresponding to the advantageous carbon (CH), alcohol(C-OH), carbonyl (C=O), and carboxyl (COOH) species [276-278]. The carbon species present in the initial vacuum could have originated from a number of sources such as the washes with

ethanol, exposure to the atmosphere, and desorbed molecules from the vacuum chamber walls.

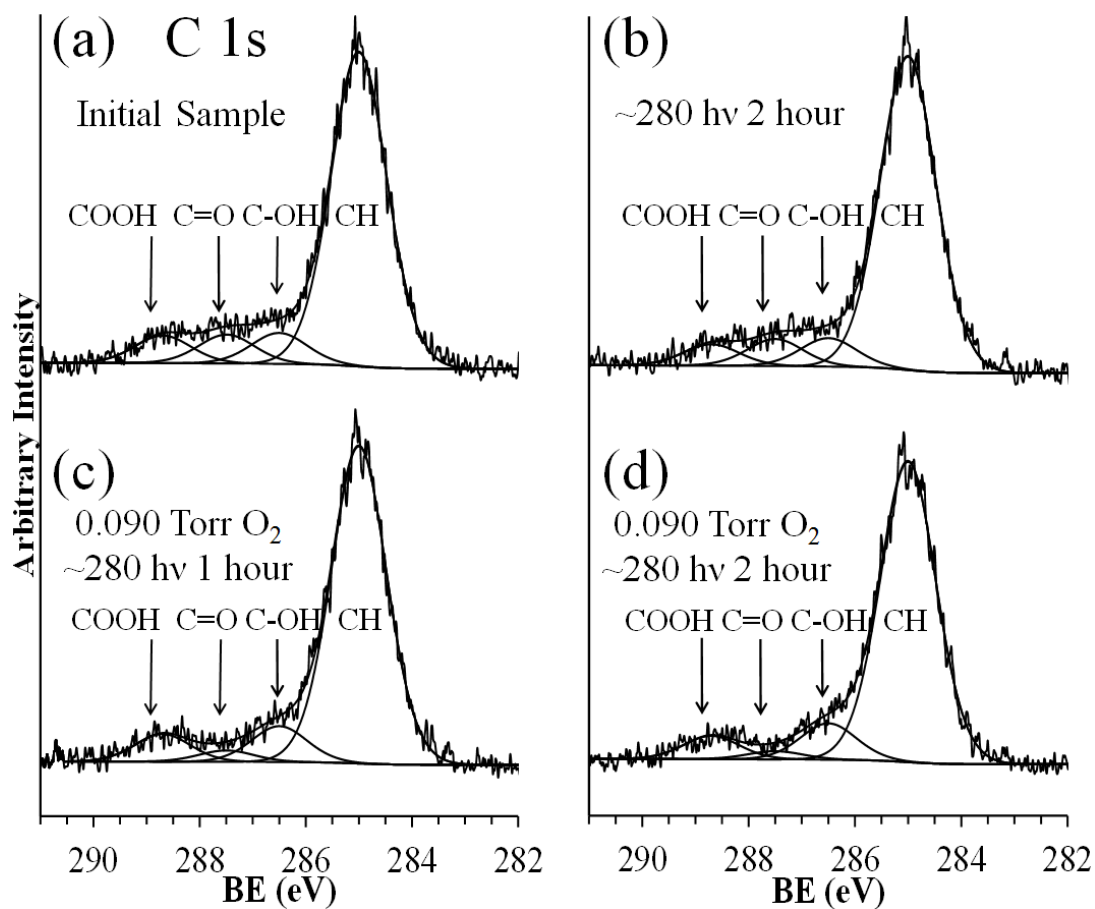


Figure 5.2: C 1s spectra taken of the (a) initial sample of the native oxide film on Mn, (b) illuminated for 2 hours, (c) under 0.09 Torr O₂ illuminated for 1 hour, and (d) 2 hours. Components fit to the advantageous carbon (CH), alcohol(C-OH), ketone (C=O), and carboxyl(COOH) species of the C1s.

5.4.1.2 Manganese Oxide Chemistry in the Presence of Oxygen, Water, and Simulated Solar Light

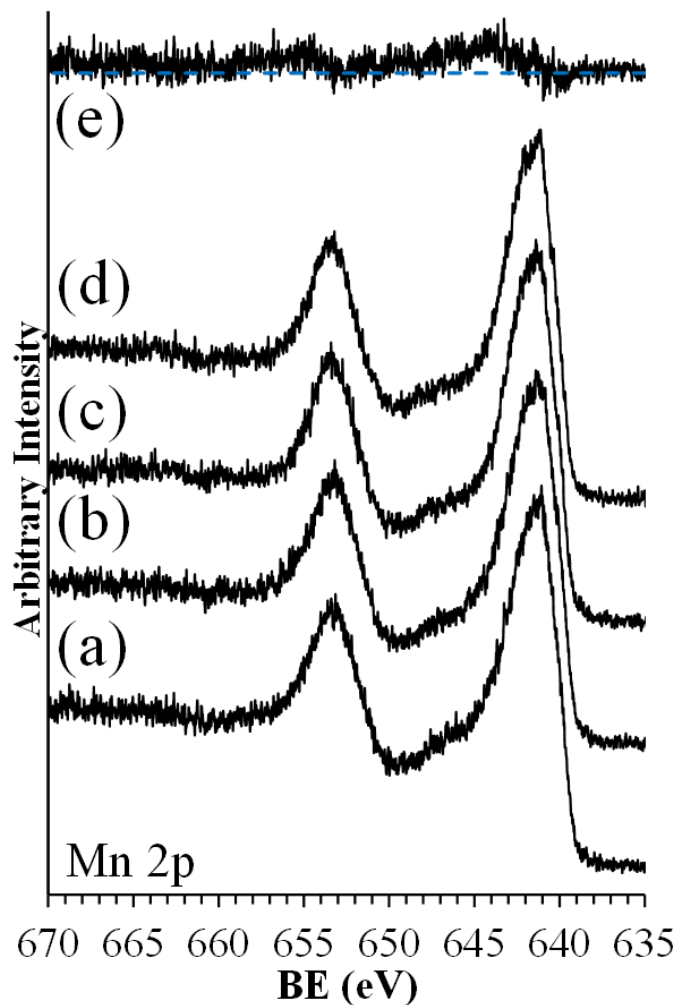


Figure 5.3: Mn 2p spectra offset of the (a) initial sample of the native oxide film on Mn, (b) illuminated for 2 hours, (c) under 0.09 Torr O₂ illuminated for 1 hour, and (d) 2 hours. (e) the difference between (a) and (d).

The manganese oxide sample was then exposed to a sequence of reaction conditions starting with solar simulated light and then a combination of light and 0.09 Torr O₂. The hope being that the combination of UV light and the presence of O₂

which react with photogenerated electrons to form reactive oxygen species would induce chemical changes on the surface of the oxide. The Mn 2p spectra are displayed vertically offset (**Figure 5.3**), under vacuum and relevant reaction conditions. The XPS signal from the Mn 2p has difficulty in quantitative analysis of for the II, III, and IV oxidation states of manganese. These Mn 2p spectra contain many multiplet-split components and have a high degree of spectral overlap [234]. A shake-up feature can be observed at approximately 646 eV which is indicative of the Mn²⁺ oxide, as this feature is not present in XPS spectra of either Mn₂O₃ or MnO₂ [279]. Metallic manganese has a distinct and narrow peak relative to manganese oxides that has a binding energy centered about 639 eV, which is not observable in the spectrum of Figure 5.3 [280]. Thus, the inference that the native oxide layer over this sample can be estimated to be at least 5.23 nm based on three times the IMFP of the Mn 2p photoelectron through MnO from NIST IMFP database using the TPP-2m predictive formula [281]. The oxidation state of Mn is often determined by the peak splitting of the Mn 3s (**Figure 5.4**), caused by the coupling of non-ionized 3s electrons with the 3d band. The Mn 3s has an average splitting of 5.80 ± 0.096 eV based on which the sample would have an oxidation state of MnO_{1.14} and would have an approximate band gap of 3.9 ± 0.4 eV [282]. Thus the light shown upon the sample above 318 nm wavelength would not cause an electron to be excited to the conduction band. With that given energetic cutoff, the majority of the photons generated from the Xenon bulb would not induce a photochemical response in the manganese sample.

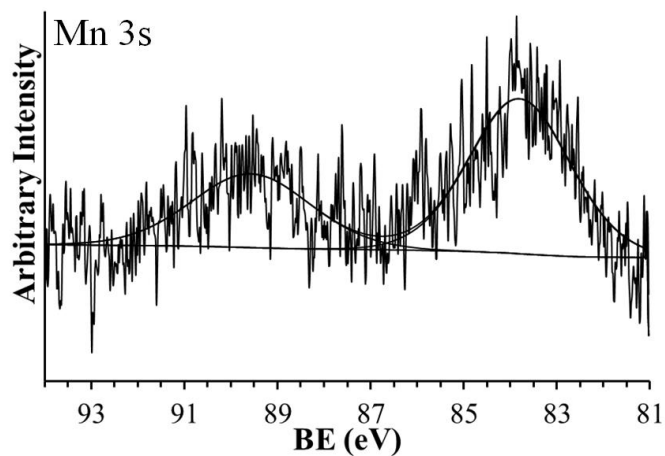


Figure 5.4: Mn 3s splitting of the initial sample of the native oxide film.

The sample was then exposed to experimental conditions which subjected the surface to light >280 nm. The total exposure of solely UV light upon the sample lasted for a total exposure time of 2 hours. The spectra of the O 1s of the sample at 2 hours of illumination (**Figure 5.1b**) indicated that the line shape did not significantly change from that of the initial sample. Previous experiments have demonstrated that UV-radiation at wavelengths below 400 nm can cause dissociation of adsorbed water molecules at low temperatures on a $\text{TiO}_2(110)$ surface under UHV conditions [283]. However, this effect was not observed in this sample of manganese oxide as the signal of the OH component indicate that the surface concentration of hydroxyl groups did not change. The spectra of Mn 2p under illumination behaved in a similar manner to the O 1s where very little change was noted from the sample under dark conditions. In contrast the C 1s region displayed evidence of light-induced degradation of adventitious carbon species. The amount of each functionalized component of C 1s

(**Figure 5.2b**) was reduced compared to the spectra of the initial sample surface. This is indicative of direct photolysis of carbonaceous species, which are events we must take into consideration in subsequent observations in the presence of UV light and oxygen gas.

After the exposure to UV light the experiment progressed with the introduction of 0.090 Torr O₂ gas. The sample was subjected under these reaction conditions for 2 hours with spectra collected at each hour. The corresponding O 1s spectra amid these conditions are displayed in **Figure 5.1c and d** after 1 and 2 hours, respectively. A clear reduction in the intensity of the oxygenated carbon species and adsorbed water components was observed. The adsorbed water on the surface of the manganese would be expected to decrease with the addition of oxygen gas due to competitive adsorption, and indeed the water intensity of the total O 1s spectra decreased from 3.5 % to approximately 2 %. The decrease in the amount of O-C in the oxygen can be directly correlated to changes observed in the C 1s spectra.

The AP-XPS spectra of the C 1s core shell was presented in **Figure 5.2 c and d** while under reaction conditions. A clear decrease in the carbonyl region is observed under reaction conditions, which coincides with the decrease in intensity of the corresponding oxygen species in the O 1s spectra. The relative abundance of oxygen species and carbon species under vacuum to reaction conditions can be plotted to quantify changes to the components composition (**Figure 5.5 a and b**). Both the carbonyl species and the corresponding oxygen component are affected in a similar fashion when exposed to UV light and oxygen gas. The O-C component was lowered by 3% of the relative composition of the O 1s spectra while the carbonyl component of the C 1s was decreased by 4% of the relative composition of the C 1s spectra. The Mn

2p spectra under light and oxygen gas (**Figure 5.3c and d**) experiences slight changes when compared to spectra under dark conditions. The intensity of the shake-up feature was reduced under reaction conditions whereas the main peaks of the 2p remain relatively unchanged. **Figure 5.3e** displays the difference spectra between the Mn 2p spectra of under dark vacuum conditions and under UV light and oxygen after 2 hours. The difference spectra revealed that there is clear decrease in intensity of the shake-up features of the 2p (3/2) and (1/2) peaks. The reduction of the shakeup peak could indicate the oxidation state of the Mn at the surface has increased as the Mn 3d subshell is filled at higher oxidation states.

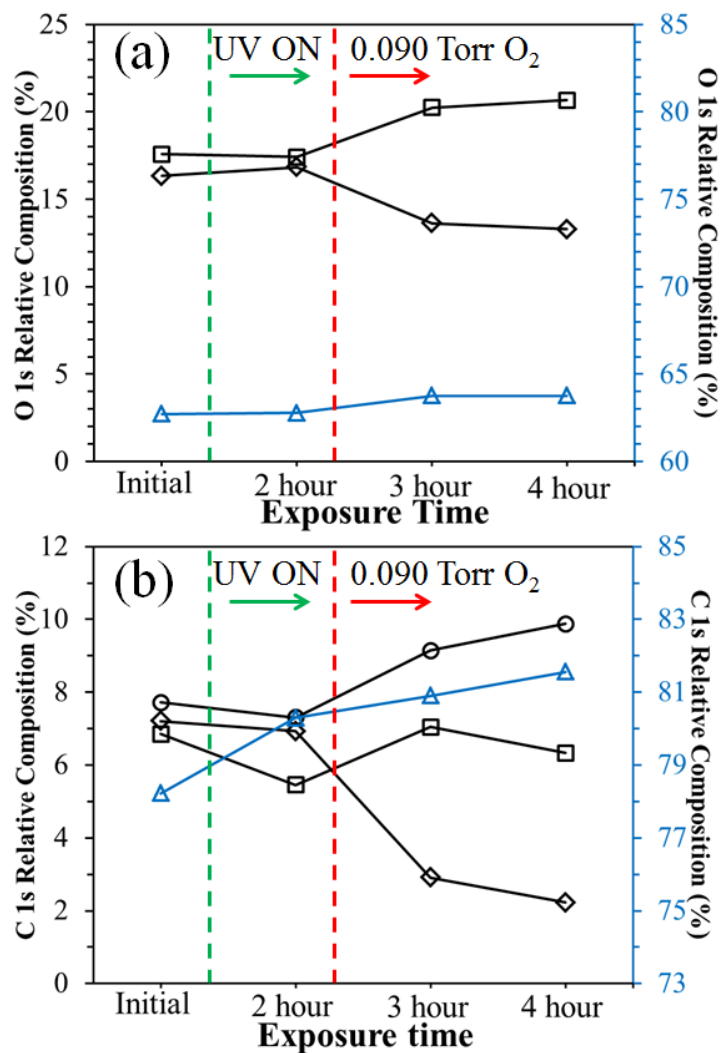


Figure 5.5: Relative abundance of oxygen and carbon species from (a) O 1s and (b) C 1s spectra taken of the initial sample of the native oxide film on Mn, 2-hour illumination, and under 0.09 Torr O₂ illuminated for 1 and 2 hours.

The ability of a semiconducting metal oxide to produce a photochemical reaction is dependent on several factors. The redox potential of the holes must be high enough to oxidize the donor species, such as target pollutant molecules, hydroxyl, among others, whereas the redox potential of the photogenerated electrons needs to be low enough to reduce electron acceptors such as O₂ and protons. The lifetime of the

photogenerated holes has an impact on the efficiency of the process and water has been known to trap hole sites on the surface. There was a small shift in binding energy that occurred when the oxygen gas and light were present in the system. Both the O1s and Mn 2p are both shifted by $\sim 0.1\text{--}0.2$ eV to higher binding energy relative to the C 1s likely due to the surface photovoltage effect (SPV) [284]. Absorbed UV-radiation induces electron/hole pairs, which are causing partial band flattening and thereby induce a BE shift and hence a shift to lower kinetic energy. The magnitude of the shift is related to the density of positive charge build up on the surface due to photogenerated electron/holes pairs.

The mechanism of aldehyde photochemical reaction on TiO_2 has been extensively studied as aldehydes are common indoor air pollutants and are appropriate targets for photocatalytic removal [259,285,286]. Small molecule carbonyl photo-oxidation on TiO_2 has been reported to progress through several parallel reaction pathways with one of the major intermediates being adsorbed carboxylate [287]. Henderson et al. [288] have reported the reaction mechanism of carbonyls as a two-step reaction where the carbonyl first reacts thermally with adsorbed oxygen to form surface bound diolate. Then a substrate mediated photodecomposition mechanism induces the fragmentation of the diolate complex into gas phase radical and surface adsorbed formate. The formate is then further oxidized to CO_2 and water. The COOH intensity under UV illumination and O_2 gas remained unchanged as the C=O species was depleted (**Figure 5.5**). This suggests that an intermediate was not observed to be adsorbed on the surface and the reaction mechanism over manganese oxide in this study does not necessarily follow the same reaction pathway, although it is possible the same end products of CO_2 and H_2O are formed. In photocatalytic synthesis MnO_2

is often employed to convert alcohols to carbonyls [262,289]. The high oxidation state of MnO_2 has a narrower band gap, of 1.8-2.7 eV, [290,291] than MnO and is typically considered catalytically more active. The data presented above would indicate that the reduced state of manganese oxide could contribute to alternate reaction pathways detrimental to the synthesis of carbonyls from alcohols.

5.4.2 Electrodeposited Manganese Oxide Film on Indium Tin Oxide (ITO) Synthesis and Photocatalytic Behavior

MnO_2 films were prepared by the electrodeposition of MnCl_2 onto indium tin oxide (ITO) coated glass slides. **Figure 5.6** shows a typical cyclic voltammogram during deposition of the manganese oxide. During the first CV cycle the current began to increase past 0.6 V, and proceeded to rise in a non-smooth fashion, until the cycle was completed, likely due to the electronic double layer taking some time to reach an equilibrium as the manganese oxide was deposited on the surface. The increase in continued increase in double layer capacitance current is indicative of film deposition on the surface of the electrode. The subsequent cycles caused observable changes in the voltammogram showing the oxidation of MnCl_2 occurring once the scanning potential reached approximately 0.8 V and the oxidation current increasing with increasing potential then in the reverse scans a reduction peak at 0.7 V was observed, consistent with literature values [292]. The oxidation of Mn^{2+} is accountable for the anodic peak and the reduction of the Mn^{4+} species is likely responsible for the cathodic peak, possibly in the form of MnOOH . The oxidation current decreases slightly in size, though not appreciable with cycle number. The deposited film gradually became

visible on the surface of the ITO after the first cycle, followed by a change in film color from brown to black as more scans were performed.

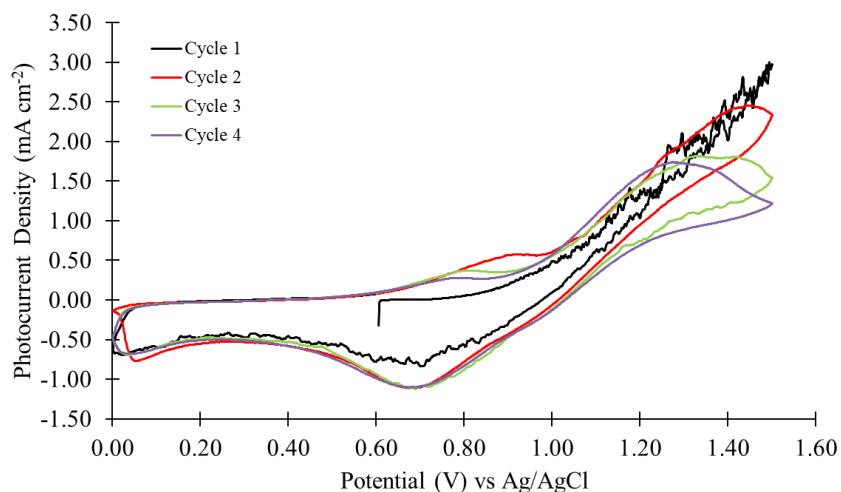


Figure 5.6: Cyclic voltammograms of an ITO glass electrode in a solution of 0.10 M MnCl_2 with a scan rate of 10 mV/s.

The surface morphology of the MnO_2 -modified ITO glass substrate was revealed by SEM (**Figure 5.7**). SEM images of the electrodeposited MnO_2 show a very high coverage of needle- or wire-like nanostructures. The needle-like structures are estimated to be about 100-200 nm in length. This pattern of nanostructure is consistent with MnO_2 films which have been electrodeposited and by acidic redox deposition [292,293]. The morphology of the electrodeposited film was also observed to be dependent on the number of CV sweeps used to form the film. The structures of manganese oxides observed are thought to be beneficial to ionic charge transport within the film due its large surface area [294,295]. The images also suggest that the coverage of manganese oxide leaves no ITO bare which is important for subsequent XPS analysis as oxygen species can thus be solely assigned to the manganese oxide

species. Optical images collected on a light microscope (**Figure 5.8**) support this claim of homogeneity of the film on a macroscale. The film appeared to be composed of a uniform layer of metal oxide coated over the ITO.

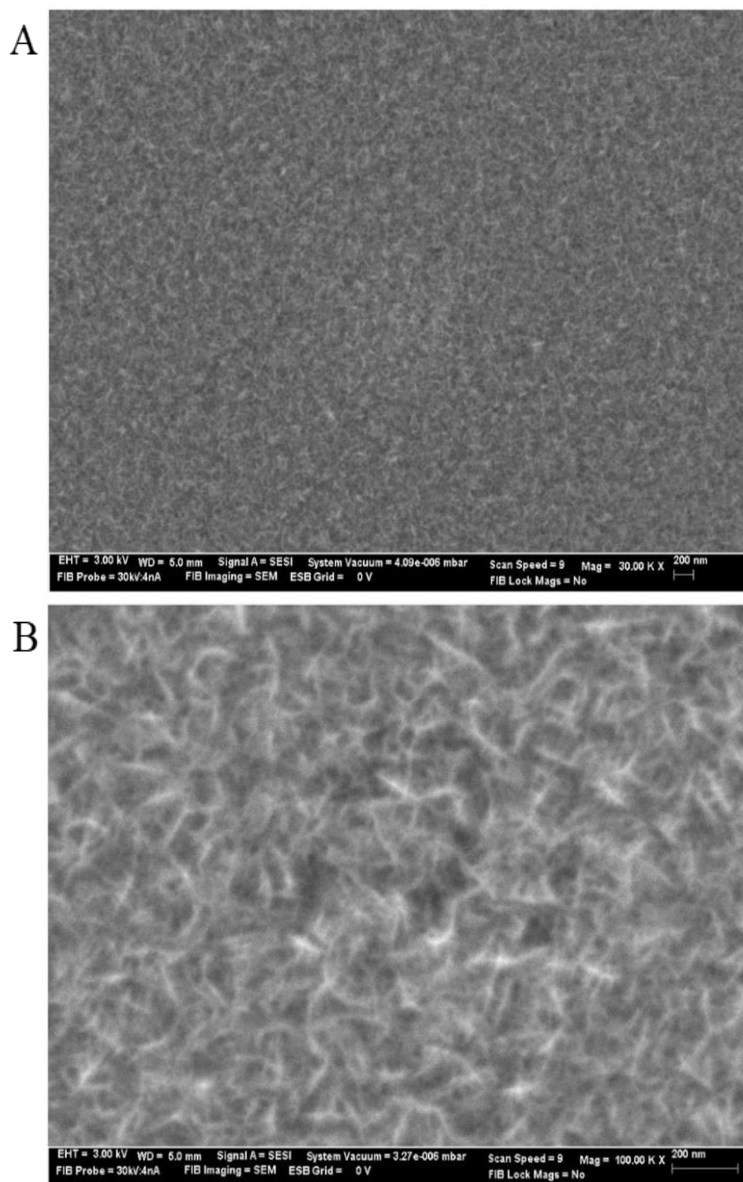


Figure 5.7: SEM images of electrodeposited MnO_2 on ITO taken at (A) 30,000x and (B) 100,000x magnification.

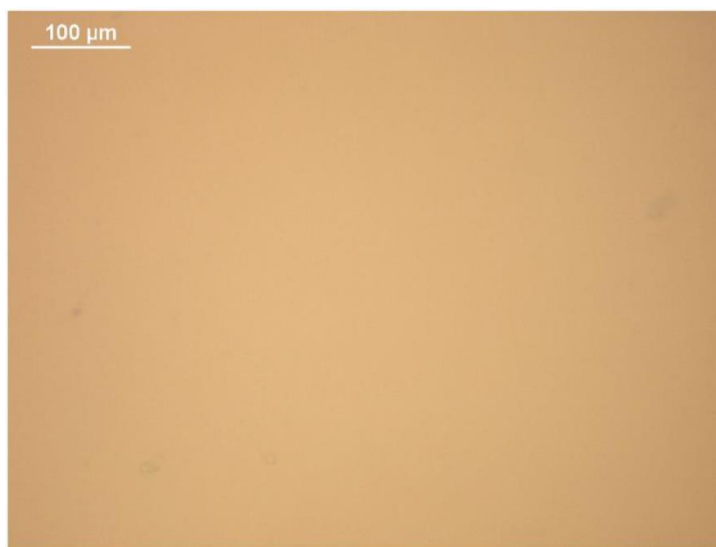


Figure 5.8: Optical image of electrodeposited MnO₂ film on ITO.

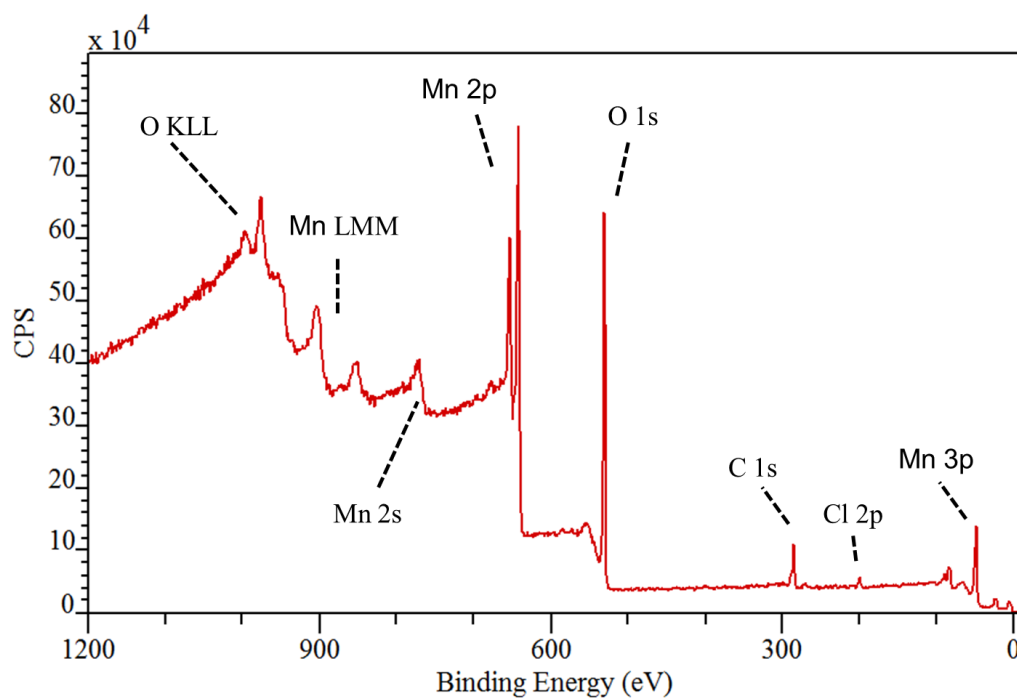


Figure 5.9: XPS survey spectra of electrodeposited MnO₂ film on ITO. Principle peaks are labeled.

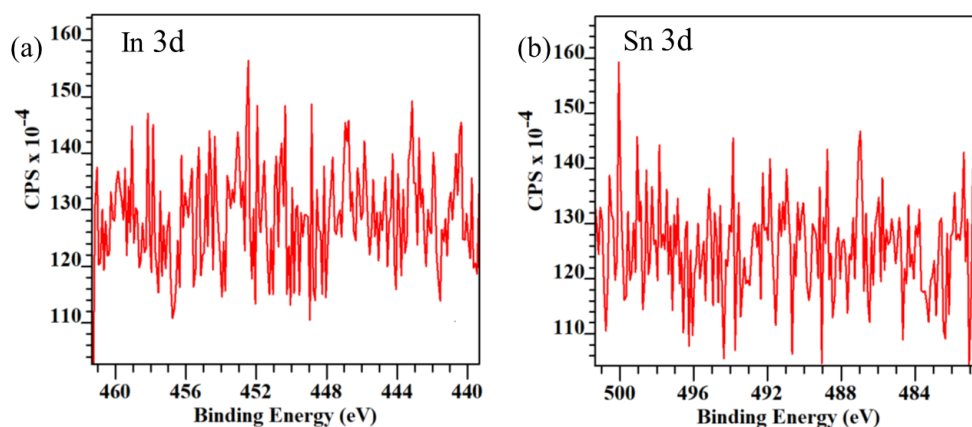


Figure 5.10: XPS spectra taken at the (a) In 3d and (b) Sn 3d regions.

XPS analysis of the electrodeposited film was used to confirm the presence of the film and characterize its elemental and chemical speciation. Survey spectra collected of the sample (**Figure 5.9**) displayed peaks only associated with a manganese oxide sample. Spectra of the In 3d (**Figure 5.10a**) and Sn 3d (**Figure 5.10b**) regions could not resolve peaks above the noise of the spectra, indicating the ITO substrate was not exposed to the vacuum and was fully covered by the electrodeposited film. Based on the Mn 2p(3/2) region of the spectra (**Figure 5.11**) the predominate species present on the sample was Mn^{4+} . The Mn 2p(3/2) spectra was fit with line shape envelopes attributed to standard Mn 2p(3/2) spectra obtained from Mn(II) oxide, Mn(III) oxide, and Mn(IV) oxides. The use of material standards with different oxidation states has been applied to many metal oxide XPS spectra, including manganese oxides [296]. Area analysis of the components revealed that the film was composed of 78 % Mn^{4+} and 22 % Mn^{3+} . This suggest that the electrodeposited film

was had an oxidation state of $\text{MnO}_{1.89}$ and that the film was either not fully oxidized to MnO_2 and contained Mn_3O_4 or MnOOH .

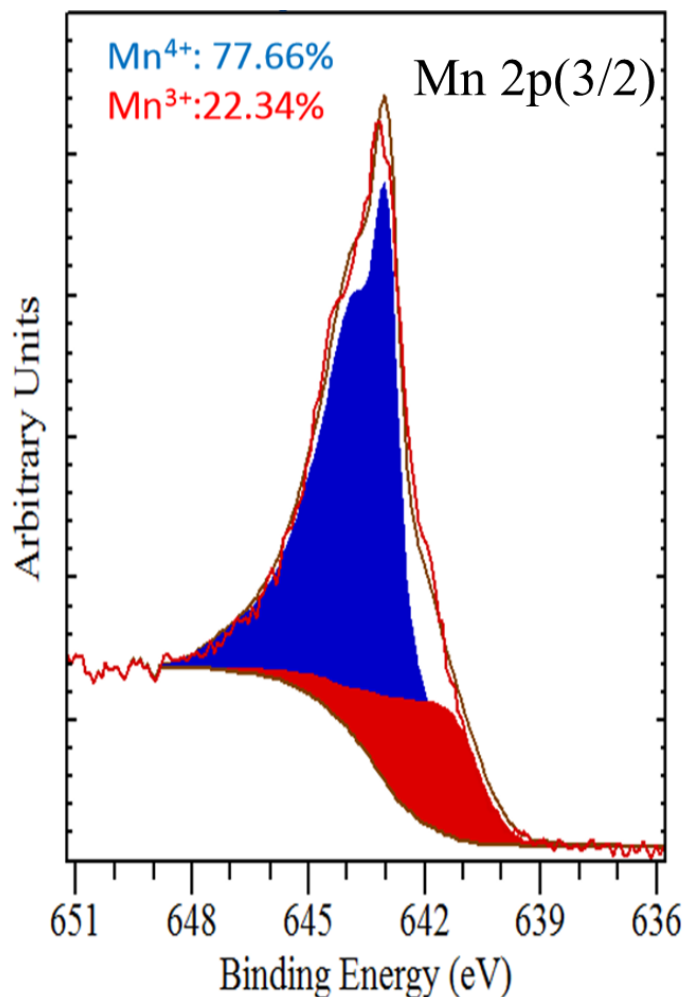


Figure 5.11: Mn 2p(3/2) XPS spectra of the electrodeposited MnO_2 film on ITO. Components fit to the contributions of Mn^{3+} (red) and Mn^{4+} (blue) oxidation states.

High resolution O1s XPS spectra (**Figure 5.12**) display a peak fit with three components. The components were assigned to oxide peak at a BE of 530.7 eV, a smaller peak at a BE of 532.3 eV attributed to hydroxyl (O-H) groups, and a third

peak associated with molecularly adsorbed water at 533.8 eV. Adsorbed water is not unexpected given that the film was generated from an aqueous solution and only pumped on with light vacuum (1×10^{-3} Torr) prior to entry into the XPS chamber. The values are in good agreement with literature values associated with those species in manganese oxides [275] and the hydroxyl species would be able to account for some of the Mn^{3+} species if it was in the form of MnOOH .

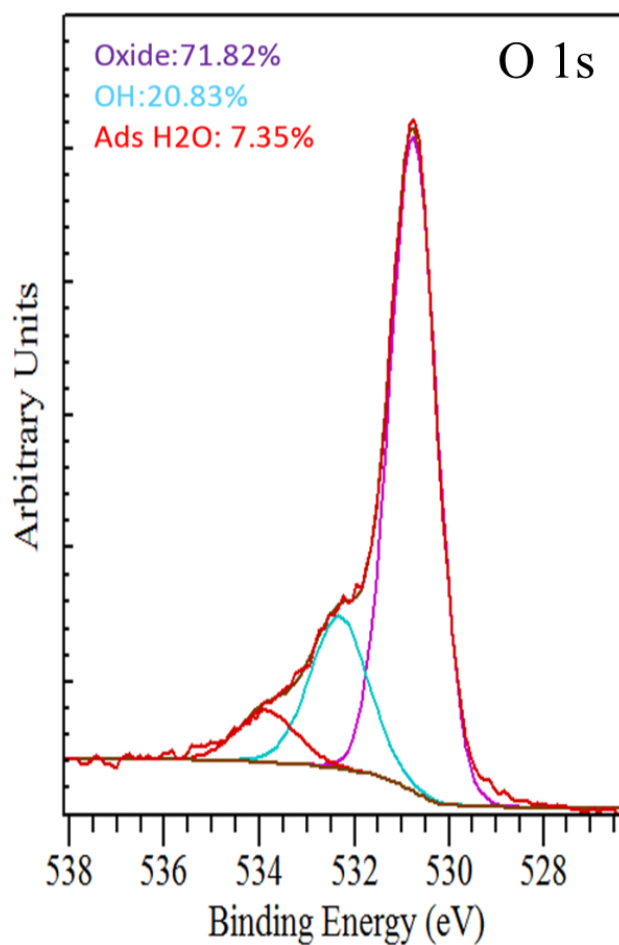


Figure 5.12: O 1s XPS spectra of the electrodeposited MnO_2 film on ITO. Components fit to the oxide (Ox), hydroxyl (O-H), and adsorbed water (H_2O).

Heterogeneous photocatalytic metal oxide semiconductors are a promising technology for water purification and volatile organic compound abatement [178][297]. The mechanism of the photocatalytic process for these metal oxides in the treatment of pollutants is as follows: a valence band electron of the metal oxide absorbs a photon with energy greater than the band gap then electron is excited to the conduction band, leaving a positively charged hole in the valence band. If the hole does not undergo recombination with the electron, then positively charged hole can oxidize water molecules to create highly-reactive hydroxyl free radicals (\bullet OH). The hydroxyl radicals are the primary reactant that remove the chemical pollutants [298]. The pollutants which analyzed for photocatalytic water treatment commonly include aromatic compounds including methylene blue which is a dye whose degradation can easily be assessed by measuring the light absorbance of the during the reaction [299]. The photocurrent generated by the electrodeposited MnO_2 film was monitored by its photocurrent density under Xenon light illumination (**Figure 5.13**). The results show film exhibited reproducible photocurrent responses with each on off cycle illumination. The current density was approximately -500 nA/cm^2 which is expected for a p-type semiconductor.

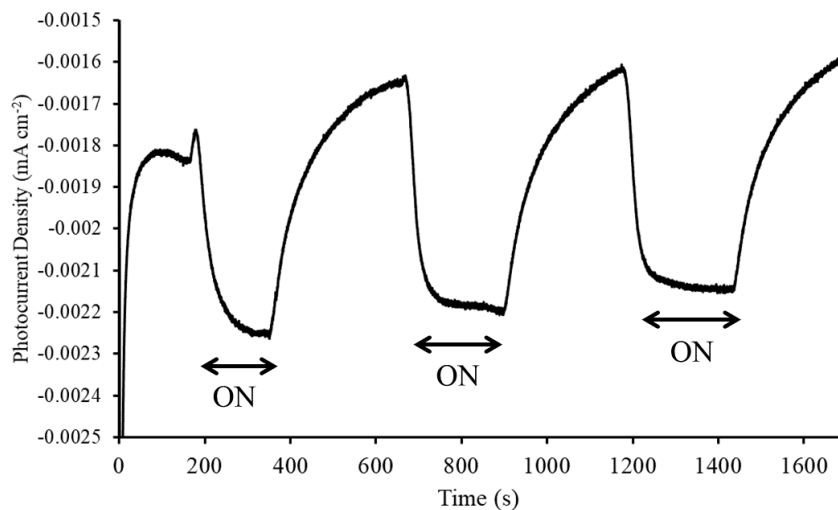


Figure 5.13: Transient photocurrents of MnO₂/ITO in 0.1 M KCl under Xenon light illumination at a 0 V bias potential.

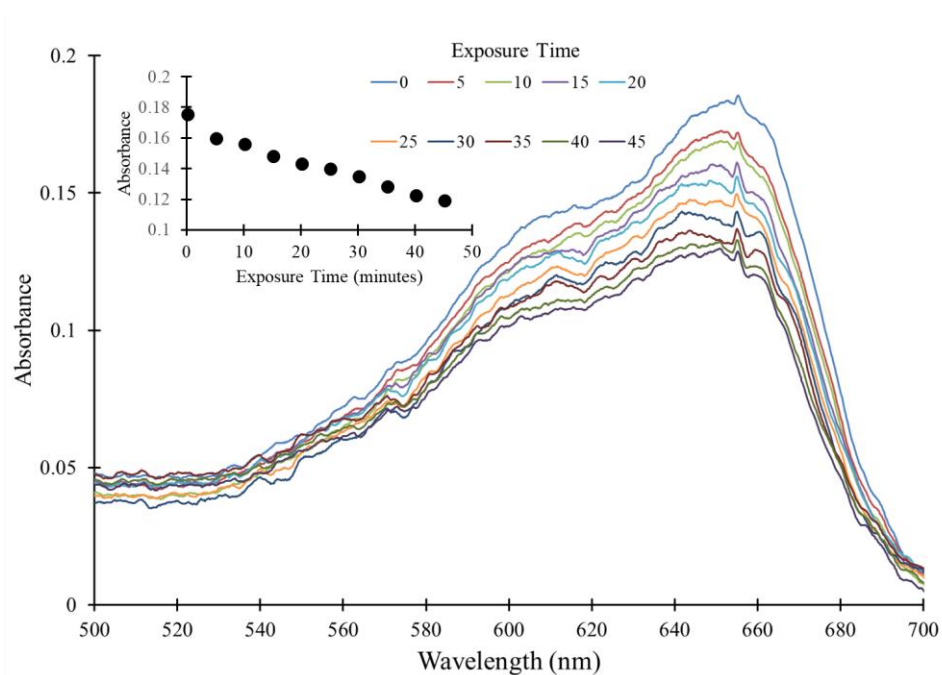


Figure 5.14: UV-Vis spectra taken of the degradation of 200 uM methylene blue in solution with MnO₂ particles during exposure to Xenon light. Inset shows absorbance degradation at the wavelength 660 nm.

The photodegradation ability of the electrodeposited film was assessed against methylene blue (**Figure 5.14**). Over the course of the 40-minute exposure the primary absorbance peak of methylene blue, 660 nm, was reduced in intensity by 32 %. The inset of **Figure 5.14** depicts the before and after illumination of the methylene blue solution. The ensuing set of the experiments on the MnO₂/ITO substrate would be to conduct further characterizations of the films, after determining the best synthetic recipe that produces high quality reproducible films. Several factors can have an effect on film integrity including concentration, pH, and electrodeposition parameters. Efforts have been made into produce films at a constant anodic potential, to possibly remove the reduction processes that occurs during the reverse sweep of the CV that may lead to MnOOH formation. The next step would be to examine the electrodeposited film *in-situ* and monitor its response to exposure to light, water, oxygen, and target molecule to be photo oxidized.

5.5 Conclusions

Photocatalysis plays an important role for the conversion of solar energy into chemical fuel, electricity, the decomposition of organic pollutants etc. Within these applications the photocatalytic reactions occur on the surface of semiconductors. The ability of manganese oxides to serve as photocatalysts was investigated with several techniques. Oxides present naturally on the surface of manganese were shown to exhibit some reactivity when exposed to UV light and oxygen. Analysis of the core level spectra of O 1s and C 1s show parallel relationship between loss of carbonyl and O-C intensity. The carbonyl was likely photooxidized from reaction with an active oxygen species to form CO₂ and water products. The photooxidation that was

observed appeared to be selective for the carbonyl reactant. Subsequent AP-XPS experiments would likely aim to incorporate H₂O in the gas phase alongside of oxygen, as it would serve as a hole scavenger and source of radical hydroxide. That should improve the capacity of the manganese oxide species present on the surface to participate in photooxidation of adsorbates. Manganese oxide films were electrodeposited onto conductive ITO coated glass. XPS analysis of the deposited films indicated that the surface was primarily composed of MnO₂ which is thought to be a highly active phase of manganese oxide. The SEM images of the films displayed a high coverage of needle like nanostructures whose high surface area is desirable in catalytic materials. The electrodeposited films produced photocurrent in response to UV illumination and displayed photocatalytic degradation of methylene blue dye. As a transition metal oxide, manganese oxide could serve as a cheap alternative material with applications to VOC abatement, water purification, and catalysis. The synthesis of the film can be further refined based on targeted process or heterogeneous adsorbate which can subsequently be probed with in-situ spectroscopy.

Chapter 6

SUMMARY AND FUTURE WORK

In this dissertation the study of heterogeneous interactions between systems of fundamental interest was addressed with photoelectron spectroscopy. This dissertation thus focuses on the analysis and interpretation of data acquired during the in-situ investigation of heterogeneous processes. To this end, ambient pressure X-ray photoelectron spectroscopy (AP-XPS) as well as conventional XPS were employed to obtain relevant chemical and electronic information ascribed to adsorption of gas molecules onto a surface. In Chapter 2 of this dissertation AP-XPS instrumentation is detailed together with introductory experiments assessing the performance and important metrics of the instrument. The foremost impediment to photoelectron spectroscopy at elevated pressures is the scattering of electrons by gas molecules, which prohibits their detection. The AP-XPS described overcomes this limitation through differentially pumped stages in conjunction with an electrostatic lens system to focus the electrons to the analyzer. Fundamental experiments collected Ag 3d(5/2) signal of a silver foil assess the operation of different electrostatic lens modes and other key aspects of instrument such as electron attenuation. These metrics alongside other consideration greatly determine experimental design of AP-XPS studies.

In Chapter 3 of this dissertation AP-XPS was utilized to chemically map the deliquescence of zinc bromide as a function of relative humidity. The solid/vapor and liquid/vapor interface between salt and water are important systems in the environment and therefore are a subject of fundamental interest. Water uptake

followed salt dissolution mechanisms outlined by scanning polarization force microscopy studies and the ionic mobility of solvated atoms was observed to have a significant impact on the surface charge equilibrium. Isothermal experiments produced data sets which could be used to quantify the energetics of adsorption. The anion and cation interfacial concentration at the zinc bromide salt solution/vapor boundary was observed to have a bromide concentration enhancement. The prevalence of the of bromide at the hydrophobic solution/vapor interface can be fully explained by asymmetrical hydration forces acting on the anion and cation. However, the influence of carbonaceous material at this interface cannot be excluded and the investigation of the influence of surfactants at the solution/vapor interface and their impact of ionic interfacial concentration and water uptake is an interesting future avenue of study.

The interaction of water adsorption upon epitaxial metal oxide thin films supported on silver substrates was offered in Chapter 4. Specifically, the hydroxylation of MnO(1x1)/Ag(100) and NiO(1x1)/Ag(100) ultra-thin films were investigated with surface characterization techniques. Observations of the extent of hydroxylation based on experimental and theoretical analysis suggested a dependence on relative humidity for water dissociation to occur on manganese and nickel oxide films and that the dissociation is likely to occur at terrace sites. The hydroxylation of the manganese oxide films coincided with the limited literature available for the interaction of water on bulk MnO and suggested that a large activation barrier can result in time dependent hydroxylation observations. It is proposed that the activation barrier can be lowered from the dissociation event being initiated by water dimers, which have been shown to be more energetically favorable than water monomer dissociation on several metal oxides. The hydroxylation of ultra-thin films of NiO

differed from the literature of the bulk material, where low pressure exposures in previous studies may not have aggregated water into dimers to enable extensive hydroxylation. A nature future direction of this project would be the analysis of the hydroxylation of bulk MnO(100) and NiO(100) single crystals, which would eliminate any contribution of the underlying silver support and steric strain the films would experience. The investigation of hydroxylation events can be applied to many metal oxide and semiconductor surface, where the results within this dissertation suggest that it is critically important that these studies be conduct approaching the ambient pressure of water to best determine hydroxylation mechanisms.

Further investigations into heterogeneous interactions of manganese oxides were briefly discussed in Chapter 5 of this dissertation. The photocatalytic properties of different manganese oxides were explored with photoelectron spectroscopy. The surfaces of native oxide overlayers on manganese and electrodeposited manganese oxide films were characterized and evaluated for photocatalytic capabilities. Although mainly preliminary tests were performed on these surfaces under reactions conditions the results obtained indicated that manganese oxide photochemistry could possibly selectively oxidize carbonyl functional groups in the presence of oxygen. Early studies of electrodeposited MnO₂/ITO displayed quality film composition and photooxidative capabilities. Further experiments with these substrates can be conducted and targeted catalysis can be explored and elucidated with AP-XPS. Particular electrodeposited MnO₂/ITO morphologies can be evaluated with respect to their reactivity and selectivity towards specific photoreaction pathways. The photocatalytic properties of manganese oxides have promising applications in the areas of volatile organic compound photooxidation wand water remediation, where the exploration of

heterogeneous interactions of target molecules under *in-situ* conditions would be of great interest.

REFERENCES

Reference List

- [1] M. Salmeron, R. Schlögl, Ambient pressure photoelectron spectroscopy: a new tool for surface science and nanotechnology, *Surf. Sci. Rep.* 63 (2008) 169-199.
- [2] P. Thiel, T. Madey, The interaction of water with solid surfaces: fundamental aspects, *Surf. Sci. Rep.* 7 (1987) 211-385.
- [3] M.A. Henderson, The interaction of water with solid surfaces: fundamental aspects revisited, *Surf. Sci. Rep.* 46 (2002) 1-308.
- [4] H. Bluhm, Photoelectron spectroscopy of surfaces under humid conditions, *J. Electron. Spectrosc. Relat. Phenom.* 177 (2010) 71-84.
- [5] C. Nordling, E. Sokolowski, K. Siegbahn, Precision method for obtaining absolute values of atomic binding energies, *Phys. Rev.* 105 (1957) 1676-1677.
- [6] M.P. Seah, W.A. Dench, Quantitative electron spectroscopy of surfaces: A standard data base for electron inelastic mean free paths in solids, *Surf. Interface Anal.* 1 (1979) 2-11.
- [7] A. Knop-Gericke, E. Kleimenov, M. Hävecker, R. Blume, D. Teschner, S. Zafeiratos, R. Schlögl, V.I. Bukhtiyarov, V.V. Kaichev, I.P. Prosvirin, X-Ray Photoelectron spectroscopy for investigation of heterogeneous catalytic processes, *Adv. Catal.* 52 (2009) 213-272.
- [8] K. Siegbahn, *ESCA Applied to Free Molecules*, North-Holland Pub. Co., 1969.
- [9] H. Siegbahn, K. Siegbahn, *ESCA applied to liquids*, *J. Electron Spectrosc. Relat. Phenom.* 2 (1973) 319-325.
- [10] D. Starr, Z. Liu, M. Hävecker, A. Knop-Gericke, H. Bluhm, Investigation of solid/vapor interfaces using ambient pressure X-ray photoelectron spectroscopy, *Chem. Soc. Rev.* 42 (2013) 5833-5857.

- [11] O. Karşlıođlu, H. Bluhm, Ambient-pressure X-ray photoelectron spectroscopy (APXPS), in: J. Frenken, I. Groot (Eds.), *Operando research in heterogeneous catalysis*, Springer, 2017, pp. 31-57.
- [12] A. Shavorskiy, O. Karşlıođlu, I. Zegkinoglou, H. Bluhm, Synchrotron-based ambient pressure X-ray photoelectron spectroscopy, *Synchrotron Radiat. News.* 27 (2014) 14-23.
- [13] D.E. Starr, H. Bluhm, Z. Liu, A. Knop-Gericke, M. Havecker, Application of ambient-pressure X-ray photoelectron spectroscopy for the in-situ investigation of heterogeneous catalytic reactions, in: J.A. Rodriguez, J.C. Hanson, P.J. Chupas (Eds.), *In-Situ Characterization of Heterogeneous Catalysts*, John Wiley & Sons, Hoboken, NJ, 2013, pp. 315-343.
- [14] M. Yoshida, H. Kondoh, In situ observation of model catalysts under reaction conditions using X-ray core-level spectroscopy, *Chem. Rec.* 14 (2014) 806-818.
- [15] R. Toyoshima, H. Kondoh, In-situ observations of catalytic surface reactions with soft X-rays under working conditions, *J. Phys. Condes. Matter.* 27 (2015) 083003.
- [16] R. Ye, T.J. Hurlburt, K. Sabyrov, S. Alayoglu, G.A. Somorjai, Molecular catalysis science: Perspective on unifying the fields of catalysis, *PNAS.* 113 (2016) 5159-5166.
- [17] C.H. Wu, B. Eren, M.B. Salmeron, Structure and dynamics of reactant coadsorption on single crystal model catalysts by HP-STM and AP-XPS: A mini review, *Top. Catal.* 59 (2016) 405-419.
- [18] Z. Liu, S.D. Senanayake, J.A. Rodriguez, Elucidating the interaction between Ni and CeO_x in ethanol steam reforming catalysts: A perspective of recent studies over model and powder systems, *Appl. Catal. B.* 197 (2016) 184-197.
- [19] S. Alayoglu, G.A. Somorjai, Ambient pressure X-ray photoelectron spectroscopy for probing monometallic, bimetallic and oxide-metal catalysts under reactive atmospheres and catalytic reaction conditions, *Top. Catal.* 59 (2016) 420-438.
- [20] A. Asthagiri, D.A. Dixon, Z. Dohnálek, B.D. Kay, J.A. Rodriguez, R. Rousseau, D.J. Stacchiola, J.F. Weaver, Catalytic chemistry on oxide nanostructures, in: F. Netzer, A. Fortunelli (Eds.), *Oxide Materials at the Two-Dimensional Limit*, Springer, 2016, pp. 251-280.
- [21] J. Dou, Z. Sun, A.A. Opalade, N. Wang, W. Fu, F.F. Tao, Operando chemistry of catalyst surfaces during catalysis, *Chem. Soc. Rev.* 46 (2017) 2001-2027.

- [22] H. Bluhm, M. Haevecker, A. Knop-Gericke, M. Kiskinova, R. Schloegl, M. Salmeron, In situ X-ray photoelectron spectroscopy studies of gas-solid interfaces at near-ambient conditions, *MRS Bull.* 32 (2007) 1022-1030.
- [23] A. Shavorskiy, H. Bluhm, Ambient pressure X-ray photoelectron spectroscopy, in: K. Wilson, A. Lee (Eds.), *Heterogeneous Catalysts for Clean Technology: Spectroscopy, Design, and Monitoring*, Wiley-VCH, Weinheim, Germany, 2013, pp. 437-468.
- [24] H. Bluhm, H.C. Siegmann, Surface science with aerosols, *Surf. Sci.* 603 (2009) 1969-1978.
- [25] X. Liu, W. Yang, Z. Liu, Recent progress on synchrotron-based in-situ soft X-ray spectroscopy for energy materials, *Adv Mater.* 26 (2014) 7710-7729.
- [26] A. Klein, Interface properties of dielectric oxides, *J. Am. Ceram. Soc.* 99 (2016) 369-387.
- [27] C. Escudero, M. Salmeron, From solid-vacuum to solid-gas and solid-liquid interfaces: in situ studies of structure and dynamics under relevant conditions, *Surf. Sci.* 607 (2013) 2-9.
- [28] M. Salmeron, Physics and chemistry of material surfaces under ambient conditions of gases and liquids: What's new? *MRS Bull.* 38 (2013) 650-657.
- [29] K. Föttinger, G. Rupprechter, In situ spectroscopy of complex surface reactions on supported Pd-Zn, Pd-Ga, and Pd(Pt)-Cu nanoparticles, *Acc. Chem. Res.* 47 (2014) 3071-3079.
- [30] H. Han, G. Melaet, S. Alayoglu, G.A. Somorjai, In situ microscopy and spectroscopy applied to surfaces at work, *ChemCatChem.* 7 (2015) 3625-3638.
- [31] E.J. Crumlin, Z. Liu, H. Bluhm, W. Yang, J. Guo, Z. Hussain, X-ray spectroscopy of energy materials under in situ/operando conditions, *J. Electron Spectrosc. Relat. Phenom.* 200 (2015) 264-273.
- [32] A. Chakrabarti, M.E. Ford, D. Gregory, R. Hu, C.J. Keturakis, S. Lwin, Y. Tang, Z. Yang, M. Zhu, M.A. Bañares, A decade of operando spectroscopy studies, *Catal. Today.* 283 (2017) 27-53.
- [33] E.J. Crumlin, H. Bluhm, Z. Liu, In situ investigation of electrochemical devices using ambient pressure photoelectron spectroscopy, *J. Electron. Spectrosc. Relat. Phenom.* 190 (2013) 84-92.

- [34] K.A. Stoerzinger, W.T. Hong, E.J. Crumlin, H. Bluhm, Y. Shao-Horn, Insights into electrochemical reactions from ambient pressure photoelectron spectroscopy. *Acc. Chem. Res.* 48 (2015) 2976-2983.
- [35] C.H. Wu, R.S. Weatherup, M.B. Salmeron, Probing electrode/electrolyte interfaces in situ by X-ray spectroscopies: old methods, new tricks, *Phys. Chem. Chem. Phys.* 17 (2015) 30229-30239.
- [36] D.M. Itkis, J.J. Velasco-Velez, A. Knop-Gericke, A. Vyalikh, M.V. Avdeev, L.V. Yashina, Probing operating electrochemical interfaces by photons and neutrons, *ChemElectroChem.* 2 (2015) 1427-1445.
- [37] H. Ogasawara, S. Kaya, A. Nilsson, Operando X-Ray photoelectron spectroscopy studies of aqueous electrocatalytic systems, *Top. Catal.* (2016) 1-9.
- [38] Z. Liu, H. Bluhm, Liquid/solid interfaces studied by ambient pressure HAXPES, in: J. Woicik (Ed.), *Hard X-Ray Photoelectron Spectroscopy (HAXPES)*, Springer, 2016, pp. 447-466.
- [39] J. Cen, Q. Wu, M. Liu, A. Orlov, Developing new understanding of photoelectrochemical water splitting via in-situ techniques: a review on recent progress, *Green Energy Environ.* 2 (2017) 100-111.
- [40] Y. Choi, H. Mistry, B.R. Cuenya, New insights into working nanostructured electrocatalysts through operando spectroscopy and microscopy, *Curr. Opin. Echem.* 1 (2017) 95-103.
- [41] A. Knop-Gericke, E. Kleimenov, M. Haevecker, R. Blume, D. Teschner, S. Zafeirotos, R. Schloegl, V.I. Bukhtiyarov, V.V. Kaichev, I.P. Prosvirin, A.I. Nizovskii, H. Bluhm, A. Barinov, P. Dudin, M. Kiskinova, X-ray photoelectron spectroscopy for investigation of heterogeneous catalytic processes, in: B. Gates, H. Knozinger (Eds.), *Advances in Catalysis*, Academic Press, Burlington, MA, 2009, pp. 213-272.
- [42] D.F. Ogletree, H. Bluhm, E.D. Hebenstreit, M. Salmeron, Photoelectron spectroscopy under ambient pressure and temperature conditions, *Nucl. Instrum. Methods Phys. Res., Sect. A.* 601 (2009) 151-160.
- [43] B.S. Mun, H. Kondoh, Z. Liu, P.N. Ross Jr, Z. Hussain, The development of ambient pressure X-Ray photoelectron spectroscopy and its application to surface science, in: J. Park (Ed.), *Current Trends of Surface Science and Catalysis*, Springer, 2014, pp. 197-229.

- [44] G. Olivieri, J.B. Giorgi, R.G. Green, M.A. Brown, 5 years of ambient pressure photoelectron spectroscopy (APPES) at the swiss light source (SLS), *J. Electron. Spectrosc. Relat. Phenom.* 216 (2017) 1-16.
- [45] L. Trotochaud, A.R. Head, O. Karshioğlu, L. Kyhl, H. Bluhm, Ambient pressure photoelectron spectroscopy: Practical considerations and experimental frontiers, *J. Phys. Condes. Matter.* 29 (2017) 053002.
- [46] S. Kato, M. Ammann, T. Huthwelker, C. Paun, M. Lampimäki, M. Lee, M. Rothensteiner, J.A. van Bokhoven, Quantitative depth profiling of Ce^{3+} in Pt/CeO₂ by in situ high-energy XPS in a hydrogen atmosphere, *Phys. Chem. Chem. Phys.* 17 (2015) 5078-5083.
- [47] S. Axnanda, E.J. Crumlin, B. Mao, S. Rani, R. Chang, P.G. Karlsson, M.O.M. Edwards, M. Lundqvist, R. Moberg, P. Ross, Z. Hussain, Z. Liu, Using "tender" X-ray ambient pressure X-ray photoelectron spectroscopy as a direct probe of solid-liquid interface, *Sci. Rep.* 5 (2015) 09788.
- [48] E. Tsunemi, Y. Watanabe, H. Oji, Y. Cui, J. Son, A. Nakajima, Hard x-ray photoelectron spectroscopy using an environmental cell with silicon nitride membrane windows, *J. Appl. Phys.* 117 (2015) 234902.
- [49] R.K. Blundell, A.E. Delorme, E.F. Smith, P. Licence, An ARXPS and ERXPS study of quaternary ammonium and phosphonium ionic liquids: utilizing a high energy Ag L α' X-ray source, *Phys. Chem. Chem. Phys.* 18 (2016) 6122-6131.
- [50] K. Kobayashi, M. Kobata, H. Iwai, Development of a laboratory system hard X-ray photoelectron spectroscopy and its applications, *J. Electron Spectrosc. Relat. Phenom.* 190 (2013) 210-221.
- [51] M. Favaro, B. Jeong, P.N. Ross, J. Yano, Z. Hussain, Z. Liu, E.J. Crumlin, Unravelling the electrochemical double layer by direct probing of the solid/liquid interface, *Nat. Commun.* 7 (2016) 12695.
- [52] J. Kraus, R. Reichelt, S. Guenther, L. Gregoratti, M. Amati, M. Kiskinova, A. Yulaev, I. Vlassiuk, A. Kolmakov, Photoelectron spectroscopy of wet and gaseous samples through graphene membranes, *Nanoscale.* 6 (2014) 14394-14403.
- [53] A. Kolmakov, D.A. Dikin, L.J. Cote, J. Huang, M.K. Abyaneh, M. Amati, L. Gregoratti, S. Günther, M. Kiskinova, Graphene oxide windows for in situ environmental cell photoelectron spectroscopy, *Nat. Nanotechnol.* 6 (2011) 651-657.

- [54] I. Niedermaier, C. Kolbeck, H. Steinrück, F. Maier, Dual analyzer system for surface analysis dedicated for angle-resolved photoelectron spectroscopy at liquid surfaces and interfaces, *Rev. Sci. Instrum.* 87 (2016) 045105.
- [55] M. Kjærviik, A. Hermanns, P. Dietrich, A. Thissen, S. Bahr, B. Ritter, E. Kemnitz, W.E. Unger, Detection of suspended nanoparticles with near-ambient pressure X-ray photoelectron spectroscopy, *J. Electron. Spectrosc. Relat. Phenom.* 29 (2017) 474002.
- [56] D.E. Starr, M. Favaro, F.F. Abdi, H. Bluhm, E.J. Crumlin, R. van de Krol, Combined soft and hard X-ray ambient pressure photoelectron spectroscopy studies of semiconductor/electrolyte interfaces, *J. Electron. Spectrosc. Relat. Phenom.* 221 (2017) 106-115.
- [57] H. Lewerenz, M.F. Lichterman, M.H. Richter, E.J. Crumlin, S. Hu, S. Axnanda, M. Favaro, W. Drisdell, Z. Hussain, B.S. Brunschwig, Operando Analyses of Solar Fuels Light Absorbers and Catalysts, *Electrochim. Acta.* 211 (2016) 711-719.
- [58] C. Arble, M. Jia, J.T. Newberg, Lab-based ambient pressure X-ray photoelectron spectroscopy from past to present, *Surf. Sci. Rep.* 73 (2017) 1-37.
- [59] C.S. Fadley, X-ray photoelectron spectroscopy: Progress and perspectives, *J. Electron. Spectrosc. Relat. Phenom.* 178 (2010) 2-32.
- [60] H. Bluhm, X-ray photoelectron spectroscopy (XPS) for in situ characterization of thin film growth, in: G. Koster, G. Rijnders (Eds.), *In Situ Characterization of Thin Film Growth*, Woodhead Publishing Limited, Sawston, Cambridge, 2011, pp. 75-98.
- [61] I.D. Baikie, A.C. Grain, J. Sutherland, J. Lawkp, Ambient pressure photoemission spectroscopy of metal surfaces, *Appl. Surf. Sci.* 323 (2014) 45-53.
- [62] X. Liu, W. Yang, Z. Liu, Recent progress on synchrotron-based in-situ soft X-ray spectroscopy for energy materials, *Adv. Mater.* 26 (2014) 7710-7729.
- [63] K. Na, Q. Zhang, G.A. Somorjai, Colloidal metal nanocatalysts: Synthesis, characterization, and catalytic applications, *J. Clust. Sci.* 25 (2014) 83-114.
- [64] J. Weissenrieder, J. Gustafson, D. Stacchiola, Reactivity and mass transfer of low-dimensional catalysts, *Chem. Rec.* 14 (2014) 857-868.
- [65] W. Yang, J. Guo, E. Crumlin, D. Prendergast, Z. Hussain, Experiments and theory of in situ and operando soft X-ray spectroscopy for energy storage, *Synchrotron Radiat. News.* 27 (2014) 4-13.

- [66] J. Yano, H. Joel, J. Gregoire, D. Friebel, A. Nilsson, F. Houle, JCAP research on solar fuel production at light sources, *Synchrotron Radiat. News.* 27 (2014) 14-17.
- [67] H. Shi, J.A. Lercher, X. Yu, Sailing into uncharted waters: recent advances in the in situ monitoring of catalytic processes in aqueous environments, *Catal. Sci. Technol.* 5 (2015) 3035-3060.
- [68] W.H. Doh, V. Papaefthimiou, S. Zafeiratos, Applications of synchrotron-based X-ray photoelectron spectroscopy in the characterization of nanomaterials, in: C.S.S.R. Kumar (Ed.), *Surface Science Tools for Nanomaterials Characterization*, Springer, Berlin, 2015, pp. 317-366.
- [69] G. Ketteler, P. Ashby, B.S. Mun, I. Ratera, H. Bluhm, B. Kasemo, M. Salmeron, In situ photoelectron spectroscopy study of water adsorption on model biomaterial surfaces, *J. Phys. Condens. Matter.* 20 (2008) 184024.
- [70] J.T. Newberg, J. Åhlund, C. Arble, C. Goodwin, Y. Khalifa, A. Broderick, A lab-based ambient pressure X-ray photoelectron spectrometer with exchangeable analysis chambers, *Rev. Sci. Instrum.* 86 (2015) 085113.
- [71] J.F. Moulder, W.F. Stickle, P.E. Sobol, K.D. Bomben, *Handbook of X-Ray Photoelectron Spectroscopy*, Physical Electronics, Inc., Eden Prairie, MN, 1995.
- [72] N. Mårtensson, P. Baltzer, P.A. Bruhwiler, J.O. Forsell, A. Nilsson, A. Stenborg, B. Wannberg, A very high-resolution electron spectrometer, *J. Electron. Spectrosc. Relat. Phenom.* 70 (1994) 117-128.
- [73] M.O. Edwards, P.G. Karlsson, S.K. Eriksson, M. Hahlin, H. Siegbahn, H. Rensmo, M. Kahk, I.J. Villar-Garcia, D.J. Payne, J. Åhlund, Increased photoelectron transmission in high-pressure photoelectron spectrometers using "Swift Acceleration", *Nucl. Instrum. Methods Phys. Res. A.* 785 (2015) 191-196.
- [74] S.K. Eriksson, M. Hahlin, J.M. Kahk, I.J. Villar-Garcia, M.J. Webb, H. Grennberg, R. Yakimova, H. Rensmo, K. Edstrom, A. Hagfeldt, H. Siegbahn, M.O.M. Edwards, P.G. Karlsson, K. Backlund, J. Ahlund, D.J. Payne, A versatile photoelectron spectrometer for pressures up to 30 mbar, *Rev. Sci. Instrum.* 85 (2014) 075119.
- [75] J. Pantforder, S. Pollmann, J. Zhu, D. Borgmann, R. Denecke, H. Steinrück, New setup for in situ X-ray photoelectron spectroscopy from ultrahigh vacuum to 1 mbar, *Rev. Sci. Instrum.* 76 (2005) 014102.

- [76] G. Karwasz, R.S. Brusa, A. Gasparoli, A. Zecca, Total cross-section measurements for e⁻-CO scattering: 80-4000 eV, *Chem. Phys. Lett.* 211 (1993) 529-533.
- [77] F. Mangolini, J. Ahlund, G.E. Wabiszewski, V.P. Adiga, P. Egberts, F. Streller, K. Backlund, P.G. Karlsson, B. Wannberg, R.W. Carpick, Angle-resolved environmental X-ray photoelectron spectroscopy: a new laboratory setup for photoemission studies at pressures up to 0.4 Torr, *Rev. Sci. Instrum.* 83 (2012) 093112.
- [78] G. Kerherve, A. Regoutz, D. Bentley, C. Hood, K. Feeley, S. Knight, A. Robson, C. Turner, N. Singh, J. Pontefract, Laboratory-based high pressure X-ray photoelectron spectroscopy: a novel and flexible reaction cell approach, *Rev. Sci. Instrum.* 88 (2017) 033102.
- [79] M.J. Jackman, A.G. Thomas, C. Muryn, Photoelectron spectroscopy study of stoichiometric and reduced anatase TiO₂(101) surfaces: the effect of subsurface defects on water adsorption at near-ambient pressures, *J. Phys. Chem. C* 119 (2015) 13682-13690.
- [80] C. Jeong, H. Yun, H. Lee, S. Muller, J. Lee, B.S. Mun, Performance test of new near-ambient-pressure XPS at Korean Basic Science Institute and its application to CO oxidation study on Pt₃Ti polycrystalline surface, *Curr. Appl. Phys.* 16 (2016) 73-78.
- [81] D. Ogletree, H. Bluhm, G. Lebedev, C. Fadley, Z. Hussain, M. Salmeron, A differentially pumped electrostatic lens system for photoemission studies in the millibar range, *Rev. Sci. Instrum.* 73 (2002) 3872-3877.
- [82] K. Roy, C.P. Vinod, C.S. Gopinath, Design and performance aspects of a custom-built ambient pressure photoelectron spectrometer toward bridging the pressure gap: oxidation of Cu, Ag, and Au surfaces at 1 mbar O₂ pressure, *J. Phys. Chem. C* 117 (2013) 4717-4726.
- [83] A. Jürgensen, N. Esser, R. Hergenröder, Near ambient pressure XPS with a conventional X-ray source, *Surf. Interface Anal.* 44 (2012) 1100-1103.
- [84] D.J. Tobias, J.C. Hemminger, Getting specific about specific ion effects, *Science*. 319 (2008) 1197-1198.
- [85] T.F. Kahan, S.N. Wren, D.J. Donaldson, A pinch of salt is all it takes: Chemistry at the frozen water surface, *Acc. Chem. Res.* 47 (2014) 1587-1594.

- [86] S. Martin, Phase transitions of aqueous atmospheric particles, *Chem. Rev.* 100 (2000) 3403-3453.
- [87] C.M. Johnson, S. Baldelli, Vibrational sum frequency spectroscopy studies of the influence of solutes and phospholipids at vapor/water interfaces relevant to biological and environmental systems, *Chem. Rev.* 114 (2014) 8416-8446.
- [88] Z. Li, Y. Li, J. Lu, Surface tension model for concentrated electrolyte aqueous solutions by the Pitzer equation, *Ind Eng Chem Res.* 38 (1999) 1133-1139.
- [89] N.N.T. Samaras, Primary salt effects in reactions in which the substrate is neutral, *J. Phys. Chem.* 37 (1933) 437-441.
- [90] S. Ghosal, J. Hemminger, H. Bluhm, B. Mun, E. Hebenstreit, G. Ketteler, D. Ogletree, F. Requejo, M. Salmeron, Electron spectroscopy of aqueous solution interfaces reveals surface enhancement of halides, *Science.* 307 (2005) 563-566.
- [91] M.A. Brown, M. Faubel, B. Winter, X-Ray photo- and resonant Auger-electron spectroscopy studies of liquid water and aqueous solutions, *Annu. Rep. Prog. Chem.* , Sect. C. 105 (2009) 174-212.
- [92] K. Arima, P. Jiang, X. Deng, H. Bluhm, M. Salmeron, Water adsorption, solvation, and deliquescence of potassium bromide thin films on SiO₂ studied by ambient-pressure x-ray photoelectron spectroscopy, *J. Phys. Chem. C.* 114 (2010) 14900-14906.
- [93] Z. Yang, Q. Li, K.C. Chou, Structures of water molecules at the interfaces of aqueous salt solutions and silica: Cation effects, *J. Phys. Chem. C.* 113 (2009) 8201-8205.
- [94] W. Hua, D. Verreault, H.C. Allen, Surface prevalence of perchlorate anions at the air/aqueous interface, *J. Phys. Chem. Lett.* 4 (2013) 4231-4236.
- [95] E.M. Knipping, M.J. Lakin, K.L. Foster, P. Jungwirth, D.J. Tobias, R.B. Gerber, D. Dabdub, B.J. Finlayson-Pitts, Experiments and simulations of ion-enhanced interfacial chemistry on aqueous NaCl aerosols, *Science.* 288 (2000) 301-306.
- [96] J.H. Hu, Q. Shi, P. Davidovits, D.R. Worsnop, M.S. Zahniser, C.E. Kolb, Reactive uptake of Cl₂(g) and Br₂(g) by aqueous surfaces as a function of Br⁻ and I⁻ ion concentration - the effect of chemical reaction at the interface, *J. Phys. Chem.* 99 (1995) 8768-8776.

- [97] P. Jungwirth, D.J. Tobias, Specific ion effects at the air/water interface, *Chem. Rev.* 106 (2006) 1259-1281.
- [98] I. Gladich, P.B. Shepson, M.A. Carignano, I. Szleifer, Halide affinity for the water-air interface in aqueous solutions of mixtures of sodium salts, *J. Phys. Chem. A.* 115 (2011) 5895-5899.
- [99] M.H. Cheng, K.M. Callahan, A.M. Margarella, D.J. Tobias, J.C. Hemminger, H. Bluhm, M.J. Krisch, Ambient pressure X-ray photoelectron spectroscopy and molecular dynamics simulation studies of liquid/vapor interfaces of aqueous NaCl, RbCl, and RbBr Solutions, *J. Phys. Chem. C.* 116 (2012) 4545-4555.
- [100] A. Verdaguer, J.J. Segura, J. Fraxedas, H. Bluhm, M. Salmeron, Correlation between charge state of insulating NaCl surfaces and ionic mobility induced by water adsorption: a combined ambient pressure X-ray photoelectron spectroscopy and scanning force microscopy study, *J. Phys. Chem. C.* 112 (2008) 16898-16901.
- [101] A. Krepelova, T. Huthwelker, H. Bluhm, M. Ammann, Surface chemical properties of eutectic and frozen NaCl solutions probed by XPS and NEXAFS, *ChemPhysChem.* 11 (2010) 3859-3866.
- [102] H. Tissot, G. Oivieri, J. Gallet, F. Bournel, M.G. Silly, F. Sirotti, F. Rochet, Cation depth-distribution at alkali halide aqueous solution surfaces, *J. Phys. Chem. C.* 119 (2015) 9253-9259.
- [103] H. Tissot, J. Gallet, F. Bournel, G. Olivieri, M.G. Silly, F. Sirotti, A. Boucly, F. Rochet, The electronic structure of saturated NaCl and NaI solutions in contact with a gold substrate, *Top. Catal.* 59 (2016) 605-620.
- [104] F. Orlando, A. Waldner, T. Bartels-Rausch, M. Birrer, S. Kato, M. Lee, C. Proff, T. Huthwelker, A. Kleibert, J. van Bokhoven, The environmental photochemistry of oxide surfaces and the nature of frozen salt solutions: A new in situ XPS approach, *Top. Catal.* 59 (2016) 591-604.
- [105] M.D. Baer, I.W. Kuo, H. Bluhm, S. Ghosal, Interfacial behavior of perchlorate versus chloride ions in aqueous solutions, *J. Phys. Chem. B.* 113 (2009) 15843-15850.
- [106] S. Ghosal, M.A. Brown, H. Bluhm, M.J. Krisch, M. Salmeron, P. Jungwirth, J.C. Hemminger, Ion partitioning at the liquid/vapor interface of a multicomponent alkali halide solution: a model for aqueous sea salt aerosols, *J. Phys. Chem. A.* 112 (2008) 12378-12384.

- [107] J.T. Newberg, T.M. McIntire, J.C. Hemminger, Reaction of bromide with bromate in thin-film water, *J. Phys. Chem. A.* 114 (2010) 9480-9485.
- [108] M.A. Brown, P.D. Ashby, M.J. Krisch, Z. Liu, B.S. Mun, R.G. Green, J.B. Giorgi, J.C. Hemminger, Interfacial dushman-like chemistry in hydrated KIO_3 layers grown on KI, *J. Phys. Chem. C.* 114 (2010) 14093-14100.
- [109] M.J. Krisch, R. D'Auria, M.A. Brown, D.J. Tobias, J.C. Hemminger, M. Ammann, D.E. Starr, H. Bluhm, The effect of an organic surfactant on the liquid-vapor interface of an electrolyte solution, *J. Phys. Chem. C.* 111 (2007) 13497-13509.
- [110] G. Olivieri, A. Goel, A. Kleibert, M.A. Brown, Effect of X-ray spot size on liquid jet photoelectron spectroscopy, *J. Synchrotron Radiat.* 22 (2015) 1528-1530.
- [111] M.A. Brown, M. Lee, A. Kleibert, M. Ammann, J.B. Giorgi, Ion spatial distributions at the air- and vacuum- aqueous K_2CO_3 interfaces, *J. Phys. Chem. C.* 119 (2015) 4976-4982.
- [112] N. Ottosson, J. Heyda, E. Wernersson, W. Pokapanich, S. Svensson, B. Winter, G. Ohrwall, P. Jungwirth, O. Bjorneholm, The influence of concentration on the molecular surface structure of simple and mixed aqueous electrolytes, *Phys. Chem. Chem. Phys.* 12 (2010) 10693-10700.
- [113] M.A. Brown, R. D'Auria, I.-W. Kuo, M.J. Krisch, D.E. Starr, H. Bluhm, D.J. Tobias, J.C. Hemminger, Ion spatial distributions at the liquid-vapor interface of aqueous potassium fluoride solutions, *Phys. Chem. Chem. Phys.* 10 (2008) 4778-4784.
- [114] M. Lee, M.A. Brown, S. Kato, A. Kleibert, A. Türler, M. Ammann, Competition between organics and bromide at the aqueous solution-air interface as seen from ozone uptake kinetics and x-ray photoelectron spectroscopy, *J. Phys. Chem. A.* 119 (2015) 4600-4608.
- [115] M.A. Brown, B. Winter, M. Faubel, J.C. Hemminger, Spatial distribution of nitrate and nitrite anions at the liquid/vapor interface of aqueous solutions, *J. Am. Chem. Soc.* 131 (2009) 8354-8355.
- [116] P. Jungwirth, B. Winter, Ions at aqueous interfaces: From water surface to hydrated proteins, *Annu. Rev. Phys. Chem.* 59 (2008) 343-366.
- [117] B. Winter, R. Weber, P.M. Schmidt, I.V. Hertel, M. Faubel, L. Vrbka, P. Jungwirth, Molecular structure of surface-active salt solutions: Photoelectron spectroscopy and molecular dynamics simulations of aqueous tetrabutylammonium iodide, *J. Phys. Chem. B.* 108 (2004) 14558-14564.

- [118] B. Winter, R. Weber, I.V. Hertel, M. Faubel, L. Vrbka, P. Jungwirth, Effect of bromide on the interfacial structure of aqueous tetrabutylammonium iodide: Photoelectron spectroscopy and molecular dynamics simulations, *Chem. Phys. Lett.* 410 (2005) 222-227.
- [119] M. El Kazzi, I. Czekaj, E.J. Berg, P. Novák, M.A. Brown, Investigation of Li-ion solvation in carbonate based electrolytes using near ambient pressure photoemission, *Top. Catal.* 59 (2016) 628-634.
- [120] M.A. Brown, Z. Abbas, A. Kleibert, R.G. Green, A. Goel, S. May, T.M. Squires, Determination of surface potential and electrical double-layer structure at the aqueous electrolyte-nanoparticle interface, *Phys. Rev. X.* 6 (2016) 011007.
- [121] S.K. Eriksson, I. Josefsson, N. Ottosson, G. Ohrwall, O. Bjorneholm, H. Siegbahn, A. Hagfeldt, M. Odelius, H. Rensmo, Solvent Dependence of the Electronic Structure of I^- and I_3^- , *J. Phys. Chem. B.* 118 (2014) 3164-3174.
- [122] J.G. Pruyne, M. Lee, C. Fabri, A.B. Redondo, A. Kleibert, M. Ammann, M.A. Brown, M.J. Krisch, Liquid-vapor interface of formic acid solutions in salt water: A comparison of macroscopic-surface tension and microscopic in situ X-ray photoelectron spectroscopy measurements, *J. Phys. Chem. C.* 118 (2014) 29350-29360.
- [123] N. Ottosson, L. Cwiklik, J. Soderstrom, O. Bjorneholm, G. Ohrwall, P. Jungwirth, Increased propensity of I_{aq}^- for the water surface in non-neutral solutions: implications for the interfacial behavior of $\text{H}_3\text{O}_{\text{aq}}^+$ and OH_{aq}^- , *J. Phys. Chem. Lett.* 2 (2011) 972-976.
- [124] N. Ottosson, M. Faubel, S.E. Bradforth, P. Jungwirth, B. Winter, Photoelectron spectroscopy of liquid water and aqueous solution: Electron effective attenuation lengths and emission-angle anisotropy, *J. Electron Spectrosc. Relat. Phenom.* 177 (2010) 60-70.
- [125] G. Olivieri, A. Goel, A. Kleibert, D. Cvetko, M.A. Brown, Quantitative ionization energies and work functions of aqueous solutions, *Phys. Chem. Chem. Phys.* 18 (2016) 29506-29515.
- [126] T.A. Gmur, A. Goel, M.A. Brown, Quantifying specific ion effects on the surface potential and charge density at silica nanoparticle-aqueous electrolyte interfaces, *J. Phys. Chem. C.* 120 (2016) 16617-16625.

- [127] M.A. Brown, A. Goel, Z. Abbas, Effect of Electrolyte Concentration on the Stern Layer Thickness at a Charged Interface, *Angew. Chem. Int. Ed.* 55 (2016) 3790-3794.
- [128] R.K. Lam, J.W. Smith, A.M. Rizzuto, O. Karşlıoğlu, H. Bluhm, R.J. Saykally, Reversed interfacial fractionation of carbonate and bicarbonate evidenced by X-ray photoemission spectroscopy, *J. Chem. Phys.* 146 (2017) 094703.
- [129] L. Artiglia, J. Edebeli, F. Orlando, S. Chen, M. Lee, P. Corral Arroyo, A. Gilgen, T. Bartels-Rausch, A. Kleibert, M. Vazdar, M. Andres Carignano, J.S. Francisco, P.B. Shepson, I. Gladich, M. Ammann, A surface-stabilized ozonide triggers bromide oxidation at the aqueous solution-vapour interface, *Nat. Commun.* 8 (2017) 700.
- [130] C.D. Zangmeister, J.A. Turner, J.E. Pemberton, Segregation of NaBr in NaBr/NaCl crystals grown from aqueous solutions: Implications for sea salt surface chemistry, *Geophys. Res. Lett.* 28 (2001) 995-998.
- [131] M. Hucher, A. Oberlin, R. Hocart, Adsorption of water vapour on cleavage surfaces of some alkali halides, *Bull. Soc. Fr. Min. Crystallogr.* 90 (1967) 320-&.
- [132] M. Luna, F. Rieutord, N.A. Melman, Q. Dai, M. Salmeron, Adsorption of water on alkali halide surfaces studied by scanning polarization force microscopy, *J. Phys. Chem. A.* 102 (1998) 6793-6800.
- [133] Q. Dai, J. Hu, M. Salmeron, Adsorption of water on NaCl (100) surfaces: Role of atomic steps, *J. Phys. Chem. B.* 101 (1997) 1994-1998.
- [134] K. Arima, P. Jiang, D.S. Lin, A. Verdaguer, M. Salmeron, Ion segregation and deliquescence of alkali halide nanocrystals on SiO₂, *J. Phys. Chem. A.* 113 (2009) 9715-9720.
- [135] A. Verdaguer, G.M. Sacha, M. Luna, D. Frank Ogletree, M. Salmeron, Initial stages of water adsorption on NaCl(100) studied by scanning polarization force microscopy, *J. Chem. Phys.* 123 (2005) 124703.
- [136] S. Ghosal, A. Verdaguer, J.C. Hemminger, M. Salmeron, In situ study of water-induced segregation of bromide in bromide-doped sodium chloride by scanning polarization force microscopy, *J. Phys. Chem. A.* 109 (2005) 4744-4749.
- [137] M.A. Brown, V. Johaneck, J.C. Hemminger, A unique dosing system for the production of OH under high vacuum for the study of environmental heterogeneous reactions, *Rev. Sci. Instrum.* 79 (2008) 024101.

- [138] L. Greenspan, Humidity fixed-points of binary saturated aqueous-solutions, *J. Res. National Bureau of Standards*. 81 (1977) 89-96.
- [139] W. Knoll, *Handbook of Biofunctional Surfaces*, CRC Press, 2013.
- [140] M. Scrocco, Satellite Structure of ZnO and Zn(II) halides studied by X-ray photoelectron-spectroscopy, *Phys. Status Solidi B-Basic Res.* 116 (1983) 137-144.
- [141] A. Jain, Shyue Ping Ong, G. Hautier, W. Chen, W.D. Richards, S. Dacek, S. Cholia, D. Gunter, D. Skinner, G. Ceder, K.A. Persson, Commentary: The Materials Project: A materials genome approach to accelerating materials innovation, *APL Mater.* 1 (2013) 011002.
- [142] S.P. Ong, W.D. Richards, A. Jain, G. Hautier, M. Kocher, S. Cholia, D. Gunter, V.L. Chevrier, K.A. Persson, G. Ceder, Python Materials Genomics (pymatgen): A robust, open-source python library for materials analysis, *Comput. Mater. Sci.* 68 (2013) 314-319.
- [143] S. Lin, J. Kuo, Towards the ionic limit of two-dimensional materials: monolayer alkaline earth and transition metal halides, *Phys. Chem. Chem. Phys.* 16 (2014) 20763-20771.
- [144] G.E. Ewing, S.J. Peters, Adsorption of water on NaCl, *Surf. Rev. Lett.* 4 (1997) 757-770.
- [145] L. Liu, M. Krack, A. Michaelides, Interfacial water: A first principles molecular dynamics study of a nanoscale water film on salt, *J. Chem. Phys.* 130 (2009) 234702.
- [146] L. Liu, A. Laio, A. Michaelides, Initial stages of salt crystal dissolution determined with ab initio molecular dynamics, *Phys. Chem. Chem. Phys.* 13 (2011) 13162-13166.
- [147] C. Wagner, Chemical-shifts of auger lines, and auger parameter, *Faraday Discuss. Chem. Soc.* 60 (1975) 291-300.
- [148] R.D. Seals, Alexandre.R, L.T. Taylor, J.G. Dillard, Core electron binding-energy study of group IIB-VIIB compounds, *Inorg. Chem.* 12 (1973) 2485-2487.
- [149] G. Fan, S. Luo, Q. Wu, T. Fang, J. Li, G. Song, ZnBr₂ supported on silica-coated magnetic nanoparticles of Fe₃O₄ for conversion of CO₂ to diphenyl carbonate, *RSC Adv.* 5 (2015) 56478-56485.

- [150] J.J. Zuckerman, A.P. Hagen, *Inorganic Reactions and Methods, the Formation of Bonds to Halogens*, John Wiley & Sons, 2009.
- [151] L.S. Dake, D.R. Baer, J.M. Zachara, Auger parameter measurements of zinc-compounds relevant to zinc transport in the environment, *Surf. Interface Anal.* 14 (1989) 71-75.
- [152] D.J. Dai, S.J. Peters, G.E. Ewing, Water adsorption and dissociation on NaCl surfaces, *J. Phys. Chem.* 99 (1995) 10299-10304.
- [153] J. Estel, H. Hoinkes, H. Kaarmann, H. Nahr, H. Wilsch, problem of water adsorption on alkali-halide cleavage planes, investigated by secondary ion mass-spectroscopy, *Surf. Sci.* 54 (1976) 393-418.
- [154] T. Gallon, I. Higginbotham, M. Prutton, H. Tokutaka, (100) Surfaces of alkali halides. 1. Air and vacuum cleaved surfaces, *Surf. Sci.* 21 (1970) 224.
- [155] D. Briggs, M.P. Seah, *Practical Surface Analysis : By Auger and X-Ray Photo-Electron Spectroscopy*, Wiley, Chichester ; New York, 1983.
- [156] Y. Khalifa, A. Broderick, J.T. Newberg, Water vapor electron scattering cross-section measurements using a hydrophobic ionic liquid. *J. Electron Spectrosc. Relat. Phenom.* 222 (2017) 162-166.
- [157] G.E. Ewing, Ambient thin film water on insulator surfaces, *Chem. Rev.* 106 (2006) 1511-1526.
- [158] M.C. Foster, G.E. Ewing, Adsorption of water on the NaCl(001) surface. II. An infrared study at ambient temperatures, 112 (2000) 6817-6826.
- [159] S.J. Peters, G.E. Ewing, Water on salt: An infrared study of adsorbed H₂O on NaCl(100) under ambient conditions, *J. Phys. Chem. B.* 101 (1997) 10880-10886.
- [160] M. Lundholm, H. Siegbahn, S. Holmberg, M. Arbman, Core electron spectroscopy of water solutions, *J. Electron Spectrosc. Relat. Phenom.* 40 (1986) 163-180.
- [161] J.E. Enderby, Diffraction studies of aqueous ionic solutions, in: M.C. Bellissent-Funel, G.W. Neilson (Eds.), *Physics and Chemistry of Aqueous Ionic Solutions. Proceedings of the NATO Advanced Study Institute*, , 1987, pp. 129; 129-145; 145.
- [162] H. Ohtaki, T. Radnai, Structure and dynamics of hydrated ions, *Chem. Rev.* 93 (1993) 1157-1204.

- [163] N. de Leeuw, S. Parker, Effect of chemisorption and physisorption of water on the surface structure and stability of alpha-alumina, *J. Am. Ceram. Soc.* 82 (1999) 3209-3216.
- [164] N.A. Deskins, R. Rousseau, M. Dupuis, Localized electronic states from surface hydroxyls and polarons in TiO₂(110), *J. Phys. Chem. C* 113 (2009) 14583-14586.
- [165] T. Fujino, M. Katayama, K. Inudzuka, T. Okuno, K. Oura, T. Hirao, Surface hydroxyl formation on vacuum-annealed TiO₂(110), *Appl. Phys. Lett.* 79 (2001) 2716-2718.
- [166] C. Niu, K. Shepherd, D. Martini, J. Tong, J. Kelber, D. Jennison, A. Bogicevic, Cu interactions with alpha-Al₂O₃(0001): effects of surface hydroxyl groups versus dehydroxylation by Ar-ion sputtering, *Surf. Sci.* 465 (2000) 163-176.
- [167] K.A. Stoerzinger, W.T. Hong, G. Azimi, L. Giordano, Y. Lee, E.J. Crumlin, M.D. Biegalski, H. Bluhm, K.K. Varanasi, Y. Shao-Horn, Reactivity of perovskites with water: Role of hydroxylation in wetting and implications for oxygen electrocatalysis, *J. Phys. Chem. C* 119 (2015) 18504-18512.
- [168] M. Baldi, E. Finocchio, C. Pistarino, G. Busca, Evaluation of the mechanism of the oxy-dehydrogenation of propane over manganese oxide, *Appl. Catal. A* 173 (1998) 61-74.
- [169] H. Chu, L.W. Wu, The catalytic incineration of ethyl mercaptan over a MnO/Fe₂O₃ catalyst, *J. Environ. Sci. Health. Part A* 33 (1998) 1119-1148.
- [170] C. Zhang, L. Han, W. Liu, H. Yang, X. Zhang, X. Liu, Y. Yang, Facile synthesis of novel MnO_x nano-structures and their catalytic performance on CO oxidation, *CrystEngComm* 15 (2013) 5150-5155.
- [171] R. Xu, X. Wang, D. Wang, K. Zhou, Y. Li, Surface structure effects in nanocrystal MnO₂ and Ag/MnO₂ catalytic oxidation of CO, *J. Catal.* 237 (2006) 426-430.
- [172] D.A. Tompsett, S.C. Parker, M.S. Islam, Rutile (beta-)MnO₂ surfaces and vacancy formation for high electrochemical and catalytic performance, *J. Am. Chem. Soc.* 136 (2014) 1418-1426.
- [173] G. Mattioli, I. Zaharieva, H. Dau, L. Guidoni, atomistic texture of amorphous manganese oxides for electrochemical water splitting revealed by ab initio calculations combined with X-ray spectroscopy, *J. Am. Chem. Soc.* 137 (2015) 10254-10267.

- [174] V. Bayer, C. Franchini, R. Podloucky, Ab initio study of the structural, electronic, and magnetic properties of MnO(100) and MnO(110), *Phys. Rev. B.* 75 (2007) 035404.
- [175] C. Franchini, V. Bayer, R. Podloucky, G. Parteder, S. Surney, F. Netzer, Density functional study of the polar MnO(111) surface, *Phys. Rev. B.* 73 (2006) 155402.
- [176] K. Chahara, T. Ohno, M. Kasai, Y. Kozono, Magnetoresistance in magnetic manganese oxide with intrinsic antiferromagnetic spin structure, *Appl. Phys. Lett.* 63 (1993) 1990-1992.
- [177] P. Hu, Z. Huang, W. Hua, X. Gu, X. Tang, Effect of H₂O on catalytic performance of manganese oxides in NO reduction by NH₃, *Appl. Catal. , A.* 437 (2012) 139-148.
- [178] L. Lamaita, M.A. Peluso, J.E. Sambeth, H.J. Thomas, Synthesis and characterization of manganese oxides employed in VOCs abatement, *Appl. Catal. , A.* 61 (2005) 114-119.
- [179] J. Post, Manganese oxide minerals: Crystal structures and economic and environmental significance, *Proc. Natl. Acad. Sci. U. S. A.* 96 (1999) 3447-3454.
- [180] Z. Pei, X. Ma, P. Ding, W. Zhang, Z. Luo, G. Li, Study of a QCM dimethyl methylphosphonate sensor based on a ZnO-modified nanowire-structured manganese dioxide film, *Sensors.* 10 (2010) 8275-8290.
- [181] S.W. Lee, J. Kim, S. Chen, P.T. Hammond, Y. Shao-Horn, Carbon nanotube/manganese oxide ultrathin film electrodes for electrochemical capacitors, *ACS Nano.* 4 (2010) 3889-3896.
- [182] M. Chigane, M. Ishikawa, Manganese oxide thin film preparation by potentiostatic electrolyses and electrochromism, *J. Electrochem. Soc.* 147 (2000) 2246-2251.
- [183] O. Giraldo, S.L. Brock, W.S. Willis, M. Marquez, S.L. Suib, S. Ching, Manganese oxide thin films with fast ion-exchange properties, *J. Am. Chem. Soc.* 122 (2000) 9330-9331.
- [184] K.L. Pickrahn, Y. Gorlin, L.C. Seitz, A. Garg, D. Nordlund, T.F. Jaramillo, S.F. Bent, Applications of ALD MnO to electrochemical water splitting, *Phys. Chem. Chem. Phys.* 17 (2015) 14003-14011.

- [185] H. Freund, G. Pacchioni, Oxide ultra-thin films on metals: new materials for the design of supported metal catalysts, *Chem. Soc. Rev.* 37 (2008) 2224-2242.
- [186] L. Giordano, G. Pacchioni, Oxide films at the nanoscale: new structures, new functions, and new materials, *Acc. Chem. Res.* 44 (2011) 1244-1252.
- [187] H. Nishimura, T. Tashiro, T. Fujitani, J. Nakamura, Surface structure of MnO/Rh(100) studied by scanning tunneling microscopy and low-energy electron diffraction, *J. Vac. Sci. Technol. A.* 18 (2000) 1460-1463.
- [188] L. Zhang, Z. Tang, S. Wang, D. Ding, M. Chen, H. Wan, Growth and vibrational properties of MnOx thin films on Rh(111), *Surf. Sci.* 606 (2012) 1507-1511.
- [189] G.A. Rizzi, M. Petukhov, M. Sambri, R. Zanoni, L. Perriello, G. Granozzi, An X-ray photoelectron diffraction structural characterization of an epitaxial MnO ultrathin film on Pt(111), *Surf. Sci.* 482 (2001) 1474-1480.
- [190] Y. Martynova, M. Soldemo, J. Weissenrieder, S. Sachert, S. Polzin, W. Widdra, S. Shaikhutdinov, H. Freund, CO oxidation over monolayer manganese oxide films on Pt (111), *Catal. Lett.* 143 (2013) 1108-1115.
- [191] C. Hagendorf, S. Sachert, B. Bochmann, K. Kostov, W. Widdra, Growth, atomic structure, and vibrational properties of MnO ultrathin films on Pt(111), *Phys. Rev. B.* 77 (2008) 075406.
- [192] S. Sachert, S. Polzin, K. Kostov, W. Widdra, Thickness dependent vibrational and electronic properties of MnO(100) thin films grown on Pt(111), *Phys. Rev. B.* 81 (2010) 195424.
- [193] F. Li, G. Parteder, F. Allegretti, C. Franchini, R. Podloucky, S. Surnev, F.P. Netzer, Two-dimensional manganese oxide nanolayers on Pd(100): the surface phase diagram, *J. Phys. Condens. Matter.* 21 (2009) 134008.
- [194] C. Franchini, R. Podloucky, F. Allegretti, F. Li, G. Parteder, S. Surnev, F.P. Netzer, Structural and vibrational properties of two-dimensional Mn_xO_y layers on Pd(100): Experiments and density functional theory calculations, *Phys. Rev. B.* 79 (2009) 035420.
- [195] T. Obermüller, W. Steurer, S. Surnev, G. Barcaro, L. Sementa, A. Stroppa, A. Fortunelli, F.P. Netzer, Kinetic asymmetry in the growth of two-dimensional Mn oxide nanostripes, *Phys. Rev. B.* 88 (2013) 235410.

- [196] E. Soares, R. Paniago, V. de Carvalho, E. Lopes, G. Abreu, H. Pfannes, Quantitative low-energy electron diffraction analysis of MnO(100) films grown on Ag(100), *Phys. Rev. B.* 73 (2005) 035419.
- [197] F. Muller, R. de Masi, D. Reinicke, P. Steiner, S. Hufner, K. Stowe, Epitaxial growth of MnO/Ag(001) films, *Surf. Sci.* 520 (2002) 158-172.
- [198] A. Chasse, C. Langheinrich, F. Mueller, S. Huefner, Growth and structure of thin MnO films on Ag(001) in dependence on film thickness, *Surf. Sci.* 602 (2008) 597-606.
- [199] A. Chasse, C. Langheinrich, M. Nagel, T. Chasse, Photoelectron diffraction studies of Ag(001), MnO(001) and epitaxial MnO films, *Surf. Sci.* 605 (2011) 272-281.
- [200] M. Nagel, I. Biswas, H. Peisert, T. Chasse, Interface properties and electronic structure of ultrathin manganese oxide films on Ag(001), *Surf. Sci.* 601 (2007) 4484-4487.
- [201] M. Nagel, I. Biswas, P. Nagel, E. Pellegrin, S. Schuppler, H. Peisert, T. Chasse, Ultrathin transition-metal oxide films: Thickness dependence of the electronic structure and local geometry in MnO, *Phys. Rev. B.* 75 (2007) 195426.
- [202] W.B. Pearson, *A Handbook of Lattice Spacings and Structures of Metals and Alloys*, Pergamon Press, New York, 1958.
- [203] T. Okazawa, Y. Kido, Surface structure and lattice vibrations of MnO(001) analyzed by high-resolution medium energy ion scattering spectroscopy, *Surf. Sci.* 556 (2004) 101-108.
- [204] Y. Zhang, Thermal oxidation fabrication of NiO film for optoelectronic devices, *Appl. Surf. Sci.* 344 (2015) 33-37.
- [205] S. deSouza, S. Visco, L. DeJonghe, Thin-film solid oxide fuel cell with high performance at low-temperature, *Solid State Ion.* 98 (1997) 57-61.
- [206] D.T. Dekadjevi, A. Suvorova, S. Pogossian, D. Spenato, J. Ben Youssef, Experimental evidence for the role of nonuniform modes in the asymmetric magnetization reversal of a Ni/NiO system, *Phys. Rev. B.* 74 (2006) 100402.
- [207] I. Hotovy, J. Huran, L. Spiess, R. Capkovic, S. Hascik, Preparation and characterization of NiO thin films for gas sensor applications, *Vacuum.* 58 (2000) 300-307.

- [208] E. Carrasco, M.A. Brown, M. Sterrer, H. Freund, K. Kwapien, M. Sierka, J. Sauer, Thickness-dependent hydroxylation of MgO(001) thin films, *J. Phys. Chem. C*. 114 (2010) 18207-18214.
- [209] J.M. McKay, V.E. Henrich, Surface electronic structure of NiO: Defect states, O₂ and H₂O interactions, *Phys. Rev. B*. 32 (1985) 6764-6772.
- [210] D. Cappus, C. Xu, D. Ehrlich, B. Dillmann, C.A. Ventrice, K. Alshamery, H. Kuhlenbeck, H.J. Freund, Hydroxyl groups on oxide surfaces: NiO(100), NiO(111) and Cr₂O₃(111), *Chem. Phys.* 177 (1993) 533-546.
- [211] R. Reissner, U. Radke, M. Schulze, E. Umbach, Water coadsorbed with oxygen and potassium on thin NiO(100) films, *Surf. Sci.* 402 (1998) 71-75.
- [212] M. Schulze, R. Reissner, M. Lorenz, U. Radke, W. Schnurnberger, Photoelectron study of electrochemically oxidized nickel and water adsorption on defined NiO surface layers, *Electrochim. Acta.* 44 (1999) 3969-3976.
- [213] R. Reissner, M. Schulze, Multilayer adsorption of water on NiO(100) at 120 and 143K, *Surf. Sci.* 454 (2000) 183-190.
- [214] M. Schulze, R. Reissner, Adsorption of water on epitaxial NiO(100), *Surf. Sci.* 482 (2001) 285-293.
- [215] S. Yang, J.S. Kim, Effects of residual water molecules on growth of NiO films on Ag(100), *J. Korean Chem. Phys. Soc.* 52 (2008) 532-535.
- [216] D.J. Simpson, T. Bredow, A.R. Gerson, MSINDO study of water adsorption on NiO surfaces, *Theor. Chem. Acc.* 114 (2005) 242-252.
- [217] D.J. Simpson, T. Bredow, A.R. Gerson, MSINDO study of acid promoted dissolution of planar MgO and NiO surfaces, *J. Comput. Chem.* 30 (2009) 581-588.
- [218] K. Sebbari, J. Roques, C. Domain, E. Simoni, Uranyl ion interaction at the water/NiO(100) interface: A predictive investigation by first-principles molecular dynamic simulations, *J. Chem. Phys.* 137 (2012) 164701.
- [219] N. Yu, W. Zhang, N. Wang, Y. Wang, B. Tang, Water adsorption on a NiO(100) surface: A GGA+U study, *J. Phys. Chem. C*. 112 (2008) 452-457.
- [220] C.J. O'Brien, Z. Rak, D.W. Brenner, Free energies of (Co, Fe, Ni, Zn)Fe₂O₄ spinels and oxides in water at high temperatures and pressure from density functional

- theory: results for stoichiometric NiO and NiFe₂O₄ surfaces, *J. Phys. Condens. Matter.* 25 (2013) 445008.
- [221] C. Arble, X. Tong, L. Giordano, A.M. Ferrari, J.T. Newberg, Water dissociation on MnO(1x1)/Ag(100), *Phys. Chem. Chem. Phys.* 18 (2016) 25355-25363.
- [222] C. Arble, X. Tong, L. Giordano, J.T. Newberg, A.M. Ferrari, Terrace site hydroxylation upon water dimer formation on monolayer NiO/Ag(100), *Thin Solid Films.* 660 (2018) 365-372.
- [223] G. Barcaro, I.O. Thomas, A. Fortunelli, Validation of density-functional versus density-functional plus U approaches for oxide ultrathin films, *J. Chem. Phys.* 132 (2010) 124703.
- [224] C. Giovanardi, A. di Bona, S. Valeri, Oxygen-dosage effect on the structure and composition of ultrathin NiO layers reactively grown on Ag(001), *Phys. Rev. B.* 69 (2004) 075418.
- [225] T. Bertrams, H. Neddermeyer, Growth of NiO(100) layers on Ag(100): Characterization by scanning tunneling microscopy, *J. Vac. Sci. Technol. B.* 14 (1996) 1141-1144.
- [226] I. Sebastian, T. Bertrams, K. Meinel, H. Neddermeyer, Scanning tunnelling microscopy on the growth and structure of NiO(100) and CoO(100) thin films, *Faraday Discuss.* 114 (1999) 129-140.
- [227] C. Giovanardi, A. di Bona, S. Altieri, P. Luches, M. Liberati, F. Rossi, S. Valeri, Structure and morphology of ultrathin NiO layers on Ag(001), *Thin Solid Films.* 428 (2003) 195-200.
- [228] M. Caffio, A. Atrei, B. Cortigiani, G. Rovida, STM study of the nanostructures prepared by deposition of NiO on Ag(001), *J. Phys. : Condens. Matter.* 18 (2006) 2379-2384.
- [229] S. GroBer, C. Hagendorf, H. Neddermeyer, W. Widdra, The growth of thin NiO films on Ag(001) studied by scanning tunneling microscopy and spectroscopy, *Surf. Interface Anal.* 40 (2008) 1741-1746.
- [230] W. Steurer, F. Allegretti, S. Surnev, G. Barcaro, L. Sementa, F. Negreiros, A. Fortunelli, F.P. Netzer, Metamorphosis of ultrathin Ni oxide nanostructures on Ag(100), *Phys. Rev. B.* 84 (2011) 115446.

- [231] W. Steurer, S. Surnev, A. Fortunelli, F.P. Netzer, Scanning tunneling microscopy imaging of NiO(100)(1 x 1) islands embedded in Ag(100), *Surf. Sci.* 606 (2012) 803-807.
- [232] C.A. Schneider, W.S. Rasband, K.W. Eliceiri, NIH Image to ImageJ: 25 years of image analysis, *Nat. Methods.* 9 (2012) 671-675.
- [233] J.S. Foord, R.B. Jackman, G.C. Allen, An x-ray photoelectron spectroscopic investigation of the oxidation of manganese, *Philos. Mag. A.* 49 (1984) 657-663.
- [234] V. Dicasro, G. Polzonetti, XPS study of MnO oxidation, *J. Electron. Spectrosc. Relat. Phenom.* 48 (1989) 117-123.
- [235] T. Kendelewicz, C. Doyle, X. Carrier, G. Brown, Reaction of water with clean surfaces of MnO(100), *Surf. Rev. Lett.* 6 (1999) 1255-1263.
- [236] J.T. Newberg, D.E. Starr, S. Yamamoto, S. Kaya, T. Kendelewicz, E.R. Mysak, S. Porsgaard, M.B. Salmeron, G.E. Brown Jr., A. Nilsson, H. Bluhm, Autocatalytic surface hydroxylation of MgO(100) terrace sites observed under ambient conditions, *J. Phys. Chem. C.* 115 (2011) 12864-12872.
- [237] J.T. Newberg, Surface Thermodynamics and Kinetics of MgO (100) Terrace Site Hydroxylation, *J. Phys. Chem. C.* 118 (2014) 29187-29195.
- [238] P. Liu, T. Kendelewicz, G. Brown, G. Parks, Reaction of water with MgO(100) surfaces. Part I: Synchrotron X-ray photoemission studies of low-defect surfaces, *Surf. Sci.* 412-13 (1998) 287-314.
- [239] L. Giordano, A.M. Ferrari, Modified ion pair interaction for water dimers on supported MgO ultrathin films, *J. Phys. Chem. C.* 116 (2012) 20349-20355.
- [240] A. Rota, S. Altieri, S. Valeri, Growth of oxide-metal interfaces by atomic oxygen: Monolayer of NiO(001) on Ag(001), *Phys. Rev. B.* 79 (2009) 161401.
- [241] C. Bianchi, M. Cattania, P. Villa, XPS characterization of Ni and Mo oxides before and after insitu treatments, *Appl. Surf. Sci.* 70 (1993) 211-216.
- [242] H. Nesbitt, D. Legrand, G. Bancroft, Interpretation of Ni 2p XPS spectra of Ni conductors and Ni insulators, *Phys. Chem. Miner.* 27 (2000) 357-366.
- [243] A. Grosvenor, M. Biesinger, R. Smart, N. McIntyre, New interpretations of XPS spectra of nickel metal and oxides, *Surf. Sci.* 600 (2006) 1771-1779.

- [244] D. Alders, F. Voogt, T. Hibma, G. Sawatzky, Nonlocal screening effects in 2p X-ray photoemission spectroscopy of NiO(100), *Phys. Rev. B.* 54 (1996) 7716-7719.
- [245] S. Altieri, L. Tjeng, A. Tanaka, G. Sawatzky, Core-level X-ray photoemission on NiO in the impurity limit, *Phys. Rev. B.* 61 (2000) 13403-13409.
- [246] S. Yang, J. Kim, Chemical defects in ultrathin NiO films on Ag(001), *J. Korean Phys. Soc.* 56 (2010) 659-665.
- [247] J.T. Newberg, D.E. Starr, S. Yamamoto, S. Kaya, T. Kendelewicz, E.R. Mysak, S. Porsgaard, M.B. Salmeron, G.E. Brown, A. Nilsson, Formation of hydroxyl and water layers on MgO films studied with ambient pressure XPS, *Surf. Sci.* 605 (2011) 89-94.
- [248] A. Shavorskiy, K. Müller, J.T. Newberg, D.E. Starr, H. Bluhm, Hydroxylation of ultrathin Al₂O₃/NiAl(110) films at environmental humidity, *J. Phys. Chem. C.* 118 (2014) 29340-29349.
- [249] T. Kendelewicz, S. Kaya, J.T. Newberg, H. Bluhm, N. Mulakaluri, W. Moritz, M. Scheffler, A. Nilsson, R. Pentcheva, G.E. Brown Jr., X-ray photoemission and density functional theory study of the interaction of water vapor with the Fe₃O₄(001) surface at near-ambient conditions, *J. Phys. Chem. C.* 117 (2013) 2719-2733.
- [250] M.C. Biesinger, B.P. Payne, L.W. Lau, G. Andrea, R.S. Smart, X-ray photoelectron spectroscopic chemical state quantification of mixed nickel metal, oxide and hydroxide systems, *Surf. Interface Anal.* 41 (2009) 324-332.
- [251] S. Yamamoto, T. Kendelewicz, J.T. Newberg, G. Ketteler, D.E. Starr, E.R. Mysak, K.J. Andersson, H. Ogasawara, H. Bluhm, M. Salmeron, G.E. Brown Jr., A. Nilsson, Water adsorption on alpha-Fe₂O₃(0001) at near ambient conditions, *J. Phys. Chem. C.* 114 (2010) 2256-2266.
- [252] S. Altieri, S.F. Contri, S. Valeri, Hydrolysis at MgO(100)/Ag(100) oxide-metal interfaces studied by O 1s x-ray photoelectron and MgKL₂₃L₂₃ Auger spectroscopy, *Phys. Rev. B.* 76 (2007) 205413.
- [253] J. Jung, H. Shin, Y. Kim, M. Kawai, Controlling water dissociation on an ultrathin MgO film by tuning film thickness, *Phys. Rev. B.* 82 (2010) 085413.
- [254] A.O. Ibadon, P. Fitzpatrick, Heterogeneous Photocatalysis: Recent Advances and Applications, *Catalysts.* 3 (2013) 189-218.
- [255] S.J. Teichner, The origins of photocatalysis, *J. Porous Mat.* 15 (2008) 311-314.

- [256] U. Diebold, The surface science of titanium dioxide, *Surface Science Reports*. 48 (2003) 53-229.
- [257] S. Lacombe, T. Tran-Thi, C. Guillard, J. Herrmann, V. Keller-Spitzer, N. Keller, M. Maurette, P. Pichat, T. Pigot, C. Pulgarin, A. Rincon, D. Robert, Photocatalysis used against pollutants, *Actualite Chimique*. (2007) 79-93.
- [258] L. Huang, J. Mo, J. Sundell, Z. Fan, Y. Zhang, Health risk assessment of inhalation exposure to formaldehyde and benzene in newly remodeled buildings, Beijing, *PLoS One*. 8 (2013) e79553.
- [259] Q. Guo, C. Zhou, Z. Ma, Z. Ren, H. Fan, X. Yang, Elementary photocatalytic chemistry on TiO₂ surfaces, *Chem. Soc. Rev.* 45 (2016) 3701-3730.
- [260] G. Brown, V. Henrich, W. Casey, D. Clark, C. Eggleston, A. Felmy, D. Goodman, M. Gratzel, G. Maciel, M. McCarthy, K. Neelson, D. Sverjensky, M. Toney, J. Zachara, Metal oxide surfaces and their interactions with aqueous solutions and microbial organisms, *Chem. Rev.* 99 (1999) 77-174.
- [261] W.A. McClenny, K.D. Oliver, H.H. Jacumin, E.H. Daughtrey, Ambient level volatile organic compound (VOC) monitoring using solid adsorbents - recent US EPA studies, *J. Environ. Monit.* 4 (2002) 695-705.
- [262] J. Chen, J.C. Lin, V. Purohit, M.B. Cutlip, S.L. Suib, Photoassisted catalytic oxidation of alcohols and halogenated hydrocarbons with amorphous manganese oxides, *Catal. Today*. 33 (1997) 205-214.
- [263] H. Cao, S.L. Suib, Highly Efficient Heterogeneous Photooxidation of 2-Propanol to Acetone with Amorphous Manganese Oxide Catalysts, *J. Am. Chem. Soc.* 116 (1994) 5334-5342.
- [264] V.P. Santos, M.F.R. Pereira, J.J.M. Orfao, J.L. Figueiredo, Synthesis and characterization of manganese oxide catalysts for the total oxidation of ethyl acetate, *Top. Catal.* 52 (2009) 470-481.
- [265] H.C. Genuino, S. Dharmarathna, E.C. Njagi, M.C. Mei, S.L. Suib, Gas-phase total oxidation of benzene, toluene, ethylbenzene, and xylenes using shape-selective manganese oxide and copper manganese oxide catalysts, *J. Phys. Chem. C*. 116 (2012) 12066-12078.
- [266] Y. He, J. Thorne, C. Wu, P. Ma, C. Du, Q. Dong, J. Guo, D. Wang, What limits the performance of Ta₃N₅ for solar water splitting? *Chem.* 1 (2016) 640-655.

- [267] M. Lampimäki, S. Schreiber, V. Zelenay, A. Kämpelov, M. Birrer, S. Axnanda, B. Mao, Z. Liu, H. Bluhm, M. Ammann, Exploring the environmental photochemistry on the TiO₂(110) surface in situ by near ambient pressure X-ray photoelectron spectroscopy, *J. Phys. Chem. C.* 119 (2015) 7076-7085.
- [268] R. Jribi, E. Barthel, H. Bluhm, M. Grunze, P. Koelsch, D. Verreault, E. Sondergard, Ultraviolet Irradiation suppresses adhesion on TiO₂, *J. Phys. Chem. C.* 113 (2009) 8273-8277.
- [269] P. Krishnan, M. Liu, P.A. Itty, Z. Liu, V. Rheinheimer, M.H. Zhang, P.J. Monteiro, L.E. Yu, Characterization of photocatalytic TiO₂ powder under varied environments using near ambient pressure X-ray photoelectron spectroscopy, *Sci. Rep.* 7 (2017) 43298.
- [270] O. Rosseler, M. Sleiman, V. Nahuel Montesinos, A. Shavorskiy, V. Keller, N. Keller, M.I. Litter, H. Bluhm, M. Salmeron, H. Destailats, Chemistry of NO_x on TiO₂ surfaces studied by ambient pressure XPS: products, effect of UV irradiation, water, and coadsorbed K⁺, *J. Phys. Chem. Lett.* 4 (2013) 536-541.
- [271] B. Nanda, A.C. Pradhan, K.M. Parida, A comparative study on adsorption and photocatalytic dye degradation under visible light irradiation by mesoporous MnO₂ modified MCM-41 nanocomposite, *Microporous Mesoporous Mater.* 226 (2016) 229-242.
- [272] J. Zhao, J. Nan, Z. Zhao, N. Li, J. Liu, F. Cui, Energy-efficient fabrication of a novel multivalence Mn₃O₄-MnO₂ heterojunction for dye degradation under visible light irradiation, *Appl. Catal., B.* 202 (2017) 509-517.
- [273] J. Shan, Y. Zhu, S. Zhang, T. Zhu, S. Rouvimov, F. Tao, Catalytic performance and in situ surface chemistry of pure alpha-MnO₂ nanorods in selective reduction of NO and N₂O with CO, *J. Phys. Chem. C.* 117 (2013) 8329-8335.
- [274] K. Kim, N. Park, T. Kim, K. Cho, J. Lee, H. Chu, G. Sung, Indium tin oxide thin films grown on polyethersulphone (PES) substrates by pulsed-laser deposition for use in organic light-emitting diodes, *ETRI J.* 27 (2005) 405-410.
- [275] J. Junta, M. Hochella, Manganese(II) oxidation at mineral surfaces: A microscopic and spectroscopic study, *Geochim. Cosmochim. Acta.* 58 (1994) 4985-4999.
- [276] K. Prabhakaran, C. Rao, Adsorption of carbonyl-compounds on clean and modified Cu(110) Surfaces - a combined EELS-UPS Study, *Appl. Surf. Sci.* 44 (1990) 205-210.

- [277] K. Schulz, D. Cox, Oxidation, reduction, and isomerization of allyl alcohol and 1-propanol over Cu₂O(100), *J. Phys. Chem.* 97 (1993) 647-655.
- [278] K. Schulz, D. Cox, Surface-Reactions of Acrolein and Propionaldehyde on Cu₂O(100) - Nonselective Oxidation and Enolate-Mediated Side Reactions to C-3 Products, *J. Phys. Chem.* 97 (1993) 3555-3564.
- [279] H. Nesbitt, D. Banerjee, Interpretation of XPS Mn(2p) spectra of Mn oxyhydroxides and constraints on the mechanism of MnO₂ precipitation, *Am. Mineral.* 83 (1998) 305-315.
- [280] M.C. Biesinger, B.P. Payne, A.P. Grosvenor, L.W.M. Lau, A.R. Gerson, R.S.C. Smart, Resolving surface chemical states in XPS analysis of first row transition metals, oxides and hydroxides: Cr, Mn, Fe, Co and Ni, *Appl. Surf. Sci.* 257 (2011) 2717-2730.
- [281] C. J. Powell, A. Jablonski, NIST Electron Inelastic-Mean-Free-Path Database - Version 1.2, (2010).
- [282] F. Tran, P. Blaha, Accurate band gaps of semiconductors and insulators with a semilocal exchange-correlation potential, *Phys. Rev. Lett.* 102 (2009) 226401.
- [283] S. Tan, H. Feng, Y. Ji, Y. Wang, J. Zhao, A. Zhao, B. Wang, Y. Luo, J. Yang, J.G. Hou, Observation of Photocatalytic Dissociation of Water on Terminal Ti Sites of TiO₂(110)-1 x 1 Surface, *J. Am. Chem. Soc.* 134 (2012) 9978-9985.
- [284] L. Kronik, Y. Shapira, Surface photovoltage phenomena: theory, experiment, and applications, *Surf. Sci. Rep.* 37 (1999) 1-206.
- [285] J. Rasko, J. Kiss, Adsorption and surface reactions of acetaldehyde on TiO₂, CeO₂ and Al₂O₃, *Appl. Catal. A.* 287 (2005) 252-260.
- [286] A. Mattsson, L. Osterlund, Adsorption and Photoinduced Decomposition of Acetone and Acetic Acid on Anatase, Brookite, and Rutile TiO₂ Nanoparticles, *Journal of Physical Chemistry C.* 114 (2010) 14121-14132.
- [287] J. Szanyi, J.H. Kwak, Photo-catalytic oxidation of acetone on a TiO₂ powder: An in situ FTIR investigation, *J. Mol. Catal. A-Chem.* 406 (2015) 213-223.
- [288] M.A. Henderson, N.A. Deskins, R.T. Zehr, M. Dupuis, Generation of organic radicals during photocatalytic reactions on TiO₂, *J. Phys. Chem. A.* 279 (2011) 205-212.

- [289] H. Cao, S.L. Suib, Highly efficient heterogeneous photooxidation of 2-propanol to acetone with amorphous manganese oxide catalysts, *J. Am. Chem. Soc.* 116 (1994) 5334-5342.
- [290] D. Sherman, Electronic structures of iron(III) and manganese(IV) (hydr)oxide minerals: Thermodynamics of photochemical reductive dissolution in aquatic environments, *Geochim. Cosmochim. Acta.* 69 (2005) 3249-3255.
- [291] B.A. Pinaud, Z. Chen, D.N. Abram, T.F. Jaramillo, Thin Films of Sodium Birnessite-Type MnO_2 : Optical Properties, Electronic Band Structure, and Solar Photoelectrochemistry, *J. Phys. Chem. C.* 115 (2011) 11830-11838.
- [292] K. Ding, Cyclic voltammetrically-prepared MnO_2 coated on an ITO glass substrate, *J. Chin. Chem. Soc.* 56 (2009) 175-181.
- [293] M. Wu, G. Snook, G. Chen, D. Fray, Redox deposition of manganese oxide on graphite for supercapacitors, *Electrochem. Commun.* 6 (2004) 499-504.
- [294] M. Wu, Y. Huang, C. Yang, H. Jow, Electrodeposition of nanoporous nickel oxide film for electrochemical capacitors, *Int. J. Hydrogen Energy.* 32 (2007) 4153-4159.
- [295] X. Yang, Y. Wang, H. Xiong, Y. Xia, Interfacial synthesis of porous MnO_2 and its application in electrochemical capacitor, *Electrochim. Acta.* 53 (2007) 752-757.
- [296] E.S. Ilton, J.E. Post, P.J. Heaney, F.T. Ling, S.N. Kerisit, XPS determination of Mn oxidation states in Mn (hydr)oxides, *Appl. Surf. Sci.* 366 (2016) 475-485.
- [297] Z. Xiong, H. Dou, J. Pan, J. Ma, C. Xu, X.S. Zhao, Synthesis of mesoporous anatase TiO_2 with a combined template method and photocatalysis, *Crystengcomm.* 12 (2010) 3455-3457.
- [298] Q. Li, S. Mahendra, D.Y. Lyon, L. Brunet, M.V. Liga, D. Li, P.J.J. Alvarez, Antimicrobial nanomaterials for water disinfection and microbial control: Potential applications and implications, *Water Res.* 42 (2008) 4591-4602.
- [299] C. Quinones, J. Ayala, W. Vallejo, Methylene blue photoelectrodegradation under UV irradiation on Au/Pd-modified TiO_2 films, *Appl. Surf. Sci.* 257 (2010) 367-371.

Appendix A

COPYRIGHT PERMISSIONS

JOHN WILEY AND SONS LICENSE TERMS AND CONDITIONS

Jun 25, 2018

This Agreement between University Of Delaware -- Christopher Arble ("You") and John Wiley and Sons ("John Wiley and Sons") consists of your license details and the terms and conditions provided by John Wiley and Sons and Copyright Clearance Center.

License Number	4376051048656
License date	Jun 25, 2018
Licensed Content Publisher	John Wiley and Sons
Licensed Content Publication	Surface & Interface Analysis
Licensed Content Title	Quantitative electron spectroscopy of surfaces: A standard data base for electron inelastic mean free paths in solids
Licensed Content Author	M. P. Seah, W. A. Dench
Licensed Content Date	Sep 15, 2004
Licensed Content Volume	1
Licensed Content Issue	1
Licensed Content Pages	10
Type of use	Dissertation/Thesis
Requestor type	University/Academic
Format	Print and electronic
Portion	Figure/table
Number of figures/tables	1
Original Wiley figure/table number(s)	Figure 1c
Will you be translating?	No
Title of your thesis / dissertation	HETEROGENEOUS SMALL MOLECULE INTERACTIONS ON SURFACES PROBED WITH AMBIENT PRESSURE X-RAY PHOTOELECTRON SPECTROSCOPY
Expected completion date	Jul 2018
Expected size (number of pages)	200
Requestor Location	University Of Delaware 221 Academy Street NEWARK, DE 19711 United States Attn: Christopher Arble
Publisher Tax ID	EU826007151
Total	0.00 USD

ELSEVIER LICENSE
TERMS AND CONDITIONS

Jun 25, 2018

This Agreement between University Of Delaware -- Christopher Arble ("You") and Elsevier ("Elsevier") consists of your license details and the terms and conditions provided by Elsevier and Copyright Clearance Center.

License Number	4376060202529
License date	Jun 25, 2018
Licensed Content Publisher	Elsevier
Licensed Content Publication	Elsevier Books
Licensed Content Title	Advances in Catalysis
Licensed Content Author	Axel Knop-Gericke,Evgueni Kleimenov,Michael Hävecker,Raoul Blume,Detre Teschner,Spiros Zafeiratos,Robert Schlögl,Valerii I. Bukhtiyarov,Vasily V. Kaichev,Igor P. Prosvirin,Alexander I. Nizovskii,Hendrik Bluhm,Alexei Barinov,Pavel Dudin et al.
Licensed Content Date	Jan 1, 2009
Licensed Content Pages	60
Start Page	213
End Page	272
Type of Use	reuse in a thesis/dissertation
Intended publisher of new work	other
Portion	figures/tables/illustrations
Number of figures/tables/illustrations	1
Format	both print and electronic
Are you the author of this Elsevier chapter?	No
Will you be translating?	No
Original figure numbers	Figure 9
Title of your thesis/dissertation	HETEROGENEOUS SMALL MOLECULE INTERACTIONS ON SURFACES PROBED WITH AMBIENT PRESSURE X-RAY PHOTOELECTRON SPECTROSCOPY
Expected completion date	Jul 2018
Estimated size (number of pages)	200
Requestor Location	University Of Delaware 221 Academy Street NEWARK, DE 19711 United States Attn: Christopher Arble
Publisher Tax ID	98-0397604
Total	0.00 USD

ELSEVIER LICENSE
TERMS AND CONDITIONS

Jun 25, 2018

This Agreement between University Of Delaware -- Christopher Arble ("You") and Elsevier ("Elsevier") consists of your license details and the terms and conditions provided by Elsevier and Copyright Clearance Center.

License Number	4376060475726
License date	Jun 25, 2018
Licensed Content Publisher	Elsevier
Licensed Content Publication	Journal of Electron Spectroscopy and Related Phenomena
Licensed Content Title	Photoelectron spectroscopy of surfaces under humid conditions
Licensed Content Author	Hendrik Bluhm
Licensed Content Date	Mar 1, 2010
Licensed Content Volume	177
Licensed Content Issue	2-3
Licensed Content Pages	14
Start Page	71
End Page	84
Type of Use	reuse in a thesis/dissertation
Intended publisher of new work	other
Portion	figures/tables/illustrations
Number of figures/tables/illustrations	1
Format	both print and electronic
Are you the author of this Elsevier article?	No
Will you be translating?	No
Original figure numbers	Figure 4
Title of your thesis/dissertation	HETEROGENEOUS SMALL MOLECULE INTERACTIONS ON SURFACES PROBED WITH AMBIENT PRESSURE X-RAY PHOTOELECTRON SPECTROSCOPY
Expected completion date	Jul 2018
Estimated size (number of pages)	200
Requestor Location	University Of Delaware 221 Academy Street NEWARK, DE 19711 United States Attn: Christopher Arble
Publisher Tax ID	98-0397604
Total	0.00 USD

**AIP PUBLISHING LICENSE
TERMS AND CONDITIONS**

Jun 25, 2018

This Agreement between University Of Delaware -- Christopher Arble ("You") and AIP Publishing ("AIP Publishing") consists of your license details and the terms and conditions provided by AIP Publishing and Copyright Clearance Center.

License Number	4376060910333
License date	Jun 25, 2018
Licensed Content Publisher	AIP Publishing
Licensed Content Publication	Review of Scientific Instruments
Licensed Content Title	A lab-based ambient pressure x-ray photoelectron spectrometer with exchangeable analysis chambers
Licensed Content Author	John T. Newberg, John Åhlund, Chris Arble, et al
Licensed Content Date	Aug 1, 2015
Licensed Content Volume	86
Licensed Content Issue	8
Type of Use	Thesis/Dissertation
Requestor type	Author (original article)
Format	Print and electronic
Portion	Figure/Table
Number of figures/tables	5
Title of your thesis / dissertation	HETEROGENEOUS SMALL MOLECULE INTERACTIONS ON SURFACES PROBED WITH AMBIENT PRESSURE X-RAY PHOTOELECTRON SPECTROSCOPY
Expected completion date	Jul 2018
Estimated size (number of pages)	200
Requestor Location	University Of Delaware 221 Academy Street NEWARK, DE 19711 United States Attn: Christopher Arble
Billing Type	Invoice
Billing Address	University Of Delaware 221 Academy Street NEWARK, DE 19711 United States Attn: Christopher Arble
Total	0.00 USD



RightsLink®

[Home](#)[Account Info](#)[Help](#)

Title: Lab-based ambient pressure X-ray photoelectron spectroscopy from past to present
Author: Chris Arble, Meng Jia, John T. Newberg
Publication: Surface Science Reports
Publisher: Elsevier
Date: May 2018
© 2018 Elsevier B.V. All rights reserved.

Logged in as:
Christopher Arble
University Of Delaware
Account #:
3001157697

[LOGOUT](#)

Please note that, as the author of this Elsevier article, you retain the right to include it in a thesis or dissertation, provided it is not published commercially. Permission is not required, but please ensure that you reference the journal as the original source. For more information on this and on your other retained rights, please visit: <https://www.elsevier.com/about/our-business/policies/copyright#Author-rights>

[BACK](#)[CLOSE WINDOW](#)

Copyright © 2018 [Copyright Clearance Center, Inc.](#) All Rights Reserved. [Privacy statement.](#) [Terms and Conditions.](#) Comments? We would like to hear from you. E-mail us at customercare@copyright.com



RightsLink®

[Home](#)[Account Info](#)[Help](#)

Title: Water dissociation on MnO(1 × 1)/Ag(100)
Author: Chris Arble, Xiao Tong, Livia Giordano, Anna Maria Ferrari, John T. Newberg
Publication: Physical Chemistry Chemical Physics
Publisher: Royal Society of Chemistry
Date: Aug 19, 2016
Copyright © 2016, Royal Society of Chemistry

Logged in as:
Christopher Arble
University Of Delaware
Account #:
3001157697

[LOGOUT](#)

This reuse request is free of charge. Please review guidelines related to author permissions here: <http://www.rsc.org/AboutUs/Copyright/Permissionrequests.asp>

[BACK](#)[CLOSE WINDOW](#)

Copyright © 2018 [Copyright Clearance Center, Inc.](#) All Rights Reserved. [Privacy statement.](#) [Terms and Conditions.](#) Comments? We would like to hear from you. E-mail us at customercare@copyright.com



Title: Terrace site hydroxylation upon water dimer formation on monolayer NiO/Ag(100)
Author: Chris Arble, Xiao Tong, Livia Giordano, John T. Newberg, Anna Maria Ferrari
Publication: Thin Solid Films
Publisher: Elsevier
Date: Available online 18 June 2018
© 2018 Published by Elsevier B.V.

Logged in as:
Christopher Arble
University Of Delaware
Account #:
3001157697

[LOGOUT](#)

Please note that, as the author of this Elsevier article, you retain the right to include it in a thesis or dissertation, provided it is not published commercially. Permission is not required, but please ensure that you reference the journal as the original source. For more information on this and on your other retained rights, please visit: <https://www.elsevier.com/about/our-business/policies/copyright#Author-rights>

[BACK](#)[CLOSE WINDOW](#)

Copyright © 2018 [Copyright Clearance Center, Inc.](#) All Rights Reserved. [Privacy statement](#). [Terms and Conditions](#).
Comments? We would like to hear from you. E-mail us at customercare@copyright.com